DESIGN, SYNTHESIS AND CHARACTERIZATION OF 2,1,3-BENZOTHIADIAZOLE COMPRISING POLYMERS: THE EFFECT OF BRIDGING UNITS ON THE OPTOELECTRONIC PROPERTIES AND OPV DEVICE CONSTRUCTION

A THESIS SUBMITTED TO
THE GRADUATE SCHOOL OF NATURAL AND APPLIED SCIENCES
OF
MIDDLE EAST TECHNICAL UNIVERSITY

BY

CANSU ZEYTUN KARAMAN

IN PARTIAL FULFILLMENT OF THE REQUIREMENTS
FOR
THE DEGREE OF MASTER OF SCIENCE
IN
CHEMISTRY

JANUARY 2021

Approval of the thesis:

DESIGN, SYNTHESIS AND CHARACTERIZATION OF 2,1,3-BENZOTHIADIAZOLE COMPRISING POLYMERS: THE EFFECT OF BRIDGING UNITS ON THE OPTOELECTRONIC PROPERTIES AND OPV DEVICE CONSTRUCTION

submitted by **CANSU ZEYTUN KARAMAN** in partial fulfillment of the requirements for the degree of **Master of Science in Chemistry Department, Middle East Technical University** by,

Prof. Dr. Halil Kalıpçılar _____
Dean, Graduate School of **Natural and Applied Sciences**

Prof. Dr. Cihangir Tanyeli _____
Head of Department, **Chemistry**

Prof. Dr. Levent Kamil Toppare _____
Supervisor, **Chemistry, METU**

Assoc. Prof. Dr. Salih Özçubukçu _____
Co-supervisor, **Chemistry, METU**

Examining Committee Members:

Prof. Dr. Ali Çırpan
Chemistry, METU _____

Prof. Dr. Levent Kamil Toppare
Chemistry, METU _____

Assoc. Prof. Dr. Salih Özçubukçu
Chemistry, METU _____

Prof. Dr. Yasemin Arslan Udum
Technical Sciences Vocational School, Gazi University _____

Assist. Prof. Dr. Erol Yıldırım
Chemistry, METU _____

Date: _____

I hereby declare that all information in this document has been obtained and presented in accordance with academic rules and ethical conduct. I also declare that, as required by these rules and conduct, I have fully cited and referenced all material and results that are not original to this work.

Name, Surname: Cansu Zeytun Karaman

Signature :

ABSTRACT

DESIGN, SYNTHESIS AND CHARACTERIZATION OF 2,1,3-BENZOTHIADIAZOLE COMPRISING POLYMERS: THE EFFECT OF BRIDGING UNITS ON THE OPTOELECTRONIC PROPERTIES AND OPV DEVICE CONSTRUCTION

Zeytun Karaman, Cansu
M.S., Department of Chemistry
Supervisor: Prof. Dr. Levent Kamil Toppare
Co-Supervisor: Assoc. Prof. Dr. Salih Özçubukçu

January 2021, 131 pages

Recently, conjugated polymers have obtained increasing popularity in a wide range of application areas such as electrochromic (EC) devices, biosensors, organic solar cells (OPVs) and organic light-emitting diodes (OLEDs). This popularity results from ease of processability, a good charge transporting capability, and broad optical absorption ability of the conjugated polymers. 2,1,3 benzothiadiazole has been commonly used in D-A type conjugated polymers since it is one of the strongest acceptor groups resulting in low band gap polymers. Fluorination of polymer backbone has appeared to be a promising approach for the development of semiconducting polymers for photovoltaic devices. Altering frontier molecular orbitals via fluorination could lead to better device performance. Alkoxy substitution is also performed to provide better solubility and high molecular weight for polymers. Besides, fluorene is used as a donor due to its high electron density and larger absorption wavelength. Lately, bridging groups are introduced into the polymer backbone to obtain higher intermolecular charge transport, higher absorption in the spectrum, and lower

band gap. In this thesis, 2,1,3-benzothiadiazole coupled with bridging groups: furan, thiophene, 3-hexylthiophene, selenophene, and thienothiophene via Stille reaction. These groups are used to investigate the changes in electronic, optic, intermolecular charge transport, and photovoltaic properties of the polymers. GPC analyses are done to determine molecular weights of polymers. Redox behaviors of the polymers are studied using cyclic voltammetry. After optimizing thickness and morphologies of polymer: PCBM, device construction, and current-voltage property measurements are conducted in a nitrogen-filled glovebox system. The analysis of the photovoltaic devices (ITO/PEDOT:PSS/Polymer:PC70BM/Metal) is performed by means of the energy conversion efficiency measured under standard AM 1.5G illumination.

Keywords: 2,1,3-Bezohiadiazole, Donor-Acceptor Approach, Conjugated Conducting Polymers, Organic Solar Cell

ÖZ

2,1,3-BENZOTİADİAZOL İÇEREN POLİMERLERİN TASARIMI, SENTEZİ VE KARAKTERİZASYONU: KÖPRÜLEME ÜNİTELERİNİN OPTOELEKTRONİK ÖZELLİKLER VE OPV CİHAZ YAPISINA ETKİSİ

Zeytun Karaman, Cansu
Yüksek Lisans, Kimya Bölümü
Tez Yöneticisi: Prof. Dr. Levent Kamil Toppare
Ortak Tez Yöneticisi: Doç. Dr. Salih Özçubukçu

Ocak 2021 , 131 sayfa

Son yıllarda, konjuge polimerler elektrokromik (EC) cihazlar, biyosensörler, organik solar hücreler (OPV'ler) ve organik ışık yayan diyotlar (OLED'ler) gibi geniş uygulama alanlarında artan popülerlik elde etmişlerdir. Bu popülerlik, işlenebilirlik, fazlaca yük taşıma kapasitesi ve konjuge polimerlerin geniş optik absorpsiyon kabiliyetinden kaynaklanır. D-A tipi konjuge polimerlerde yaygın olarak kullanılan 2,1,3-benzotiadiazol, düşük bant aralıklı polimerler ile sonuçlanan en güçlü elektron alıcı gruplardan biridir. Flor ünitesinin polimer ana zincirine eklenmesi, yarı iletken polimerlerin geliştirilmesi açısından önemli yaklaşımlardan biridir. Enerji seviyeleri değişimleri cihaz performansı açısından daha iyi sonuçlar sağlayabilir. Ayrıca, polimerlerin daha yüksek moleküler ağırlık ve daha iyi çözünürlüğe sahip olabilmesi için alkoksi gruplarının zincire eklenmesi gerçekleştirilmiştir. Bunun yanında, floren, yüksek elektron yoğunluğu ve yüksek absorpsiyon dalga boyu nedeniyle donör olarak kullanılmıştır. Son zamanlarda, daha yüksek moleküller arası yük aktarımı, spektrumda daha yüksek absorpsiyon ve daha düşük bant aralığı için köprüleme birimleri

polimer omurgasına eklenir. Bu çalışmada, 2,1,3-benzotiyadiazol, furan, tiyofen, 3-heksiltiyofen, selenofen ve tiyenotiyofen olmak üzere köprüleme birimleri ile Stille reaksiyonuyla birleştirilmiştir. Bu gruplar, polimerlerin elektronik, optik, moleküller arası yük taşınma ve fotovoltaik özelliklerindeki değişiklikleri incelemek için kullanılmıştır. Polimerlerin molekül ağırlığını belirlemek için GPC analizi yapılmıştır. Polimerlerin redoks davranışı dönüşümlü voltametri kullanılarak incelenmiştir. Polimer kalınlığını ve morfolojilerini optimize ettikten sonra: PCBM, cihaz yapımı ve akım-voltaj ölçümleri azot altında eldivenli kabin sistemi ile yapılmıştır. Fotovoltaik cihazların (ITO/PEDOT:PSS/Polimer:PC 70 BM/Metal) analizi, standart AM 1.5G aydınlatma altında ölçülen enerji dönüşüm verimliliği ile gerçekleştirilmiştir.

Anahtar Kelimeler: 2,1,3-Benzotiadiazol, Donör-Akseptör Yaklaşımı, Konjuge İletken Polimerler, Organik Güneş Hücresi

To my precious family...

ACKNOWLEDGMENTS

I would like to thank Prof. Dr. Levent Kamil Toppare for being my advisor during my master thesis. Thanks to his valuable advice and guidance, I improved myself on the road to being a researcher. I am so lucky to have the opportunity to work with him.

I would like to thank Assoc. Prof. Dr. Salih Özçubukçu for his support and remarkable suggestions for my thesis.

I would like to thank Prof. Dr. Ali Çırpan, for welcoming me to his lab. Thanks to his endless support, guidance, and encouragement, I felt confident about completing this thesis. I would like to thank Assist. Prof. Dr. Erol Yıldırım for theoretical studies.

I would like to thank Assoc. Prof. Dr. Şerife Özdemir Hacıoğlu not only for her patience and advice but also for showing me everything that I know in electrochemical studies.

I would like to thank Dr. Seza Göker for her help and support for the organic synthesis and design of my monomers.

I would like to thank Ümmügülsüm Şahin for the photovoltaic studies and Tuğba Hacıefendioğlu for the computational studies.

I would like to thank all Toppare research group members for their friendship and help.

I would like to thank Buse Dündar for all the fun coffee breaks and memories that we have together.

I would like to thank Dersu Duman for her endless support. She is more than a sister to me. I believe that she will be right by my side whenever I need her. Thanks to her encouragement, I found courage the handle difficulties.

I owe my special thanks to my precious family. I would not change their love and support for anything else in the world. Words are not enough to reflect my gratitude to them. I am the luckiest person in the world for having them in my life, and I know that I cannot be the one who I am now without them.

My most special thanks to my husband, Kaan Karaman, for his patience and understanding. I believe that I cannot achieve anything without his invaluable love. He makes life more meaningful with his true love, and I know that he will be right there when I need him.

I would like to thank TÜBİTAK for financial support (Project No: 115F604).

TABLE OF CONTENTS

LIST OF TABLES

TABLES

LIST OF FIGURES

FIGURES

LIST OF ABBREVIATIONS

2D	2 Dimensional
3D	3 Dimensional
ACN	Acetonitrile
Ag	Silver
AEA	Adiabatic Electron Affinity
AIP	Adiabatic Ionization Potential
CB	Conduction Band
CP	Conjugated Polymers
CV	Cyclic Voltammetry
D-A	Donor-Acceptor
DCM	Dichloromethane
E_g^{el}	Electronic band gap
E_g^{op}	Optical band gap
ECD	Electrochromic Device
ESP	Electrostatic Potential Surface
FTIR	Fourier-Transform Infrared
GPC	Gel Permeation Chromatography
HOMO	Highest Occupied Molecular Orbital
HRMS	High Resolution Mass Spectroscopy
ICT	Intramolecular Charge Transfer
ITO	Indium Tin Oxide
LUMO	Lowest Unoccupied Molecular Orbital
NIR	Near Infrared
NMR	Nuclear Magnetic Resonance Spectrometer

OLED	Organic Light Emitting Diode
OPV	Organic Photovoltaic
PA	Polyacetylene
P3HT	Poly(3-hexylthiophene)
PEDOT	Polyethylenedioxythiophene
PPP	Poly(paraphenylene)
PPV	Poly(paraphenylene vinylene)
PPy	Polypyrrole
Pt	Platinum
PT	Polythiophene
PTT	Poly(thieno[3,2-b]thiophene)
$TBABF_4$	Tetrabutylammonium hexafluorophosphate
$TBAPF_6$	Tetrabutylammonium tetrafluoroborate
THF	Tetrahydrofuran
TLC	Thin Layer Chromatography
VB	Valence Band
VEA	Vertical Electron Affinity
VIP	Vertical Ionization Potential

CHAPTER 1

INTRODUCTION

1.1 Conjugated Polymers

A couple of decades ago, polymers were known as good insulators. The first known conjugated polymer in the literature was polysulfur nitride. Polysulfur nitride, in short polythiazyl, was found as dark golden/yellow insoluble powder/crystal. During the mid-1970s, it took all the attention due to its both metallic character and superconducting features. It conducts in the range between 10 and 1700 S/cm at 2K[1]. However, the real story of the conjugated polymers started after discovering the conductivity of polyacetylene (PA). PA was exposed to the vapor of the halogens, such as chlorine, bromine, or iodine. With the uptake of halogen vapor, the doping process occurred, and the silvery/black film was obtained. This film has shown electrical conductivity over the order of seven compared to the magnitude of PA [2]. By this improvement, Alan MacDiarmid, Hideki Shirakawa, and Alan J. Heeger were the winner of the Nobel Prize in Chemistry, in 2000 [3]. After this breakthrough discovery, both academia and industry have shown tremendous interest in investigating new conjugated polymers. Polypyrrole, polythiophene, poly(3-hexylthiophene), poly(paraphenylene), poly(thieno[3,2-b]thiophene), and poly(paraphenylenevinylene) are the typical examples of CPs (Figure 1.1). Researchers also realized that these conductive polymers have many advantages over their inorganic counterparts, such as flexibility, low weight, low cost, solution processability, and tunability of the band gap [4]. Therefore, these future promising materials have various applications in solar cells (OPVs), organic field-effect transistors (OFETs), organic light-emitting diodes (OLEDs), electrochromic devices (ECDs), and biosensors.

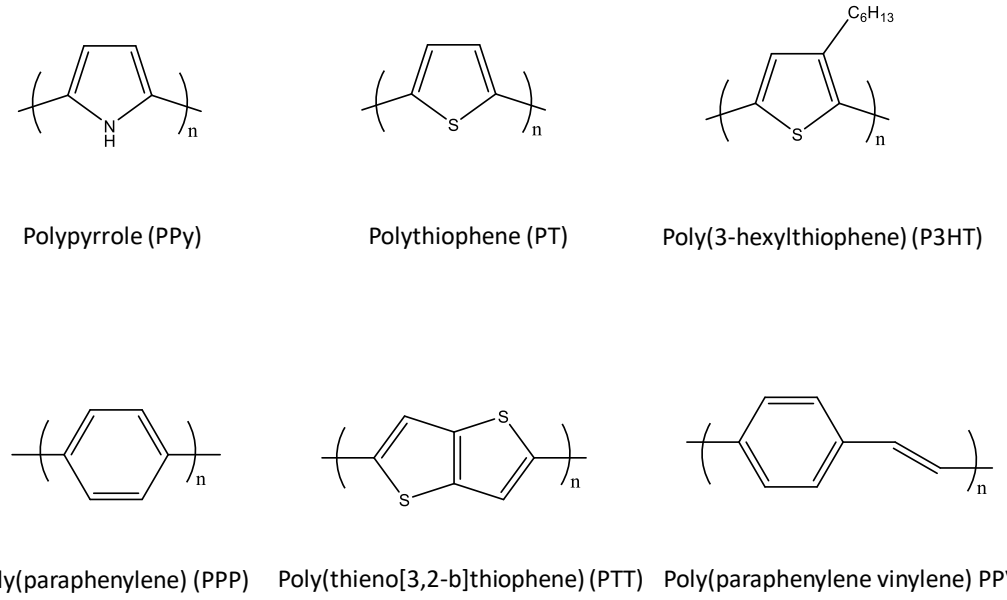

Figure 1.1: Popular conjugated polymer skeletons.

1.2 Conductivity in Conjugated Polymers

Materials can be divided into three main groups, namely metals, semiconductors, and insulators. This classification is made according to the electrical conductivity of the materials (Figure 1.2) [5]. Previously, polymers were considered as insulators until the discovery of the conductivity of polyacetylene (PA). PA has a linear chain with an alternation of localized single and double bonds, and in this form, it cannot conduct electricity. However, PA shows a significant rise in conductivity upon doping. It is doped under exposure to the halogen vapor, such as chlorine, bromine iodine vapor. Therefore, doped PA conducts electricity by the delocalization of electrons along with the skeleton [6].

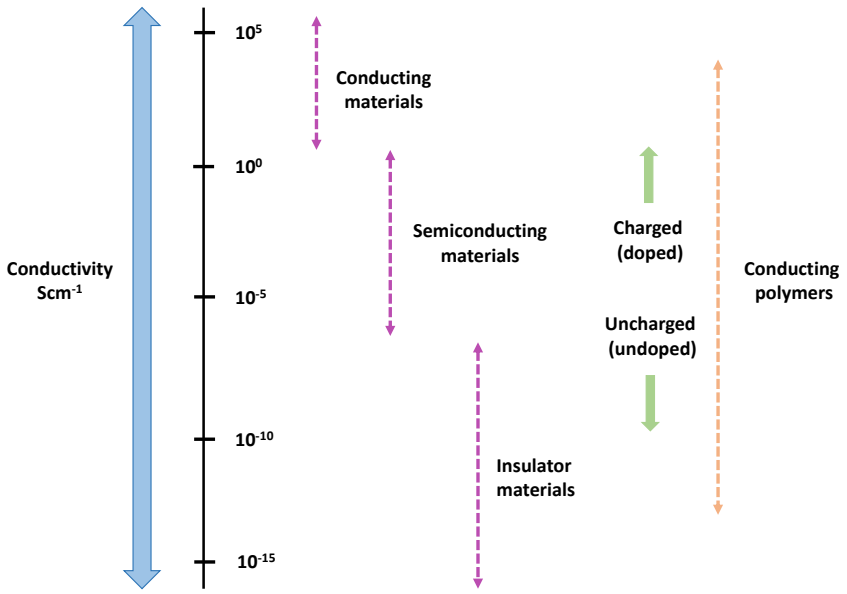

Figure 1.2: Conductivity scale of the conjugated polymers.

1.3 Band Theory

In the past, polymers were thought to be insulators because they are inadequate to use free electrons to conduct electricity. However, with the discovery of the conducting polymers, they are no longer considered as insulators. In order to understand the nature of the insulators, semiconductors, and conductors, the concept of the band gap is used. The band gap is an energy barrier between the highest-filled energy level called the highest occupied molecular orbital (HOMO), and the lowest unfilled level called the lowest unoccupied molecular orbital (LUMO). In other words, the band gap can be described as the energy gap between the valence band (VB) and the conduction band (CB). In this concept, it is stated that insulators contain a totally filled valence band and unfilled conduction band that is separated by a large energy barrier whereas, in metallic conductors, there is no energy barrier between these two levels. In semiconductors, this barrier is lower compared to that of insulators, the conduction band is partially filled with electrons, and the valence band is partially unfilled (Figure 1.3). Both conductors and semiconductors conduct electricity by electrons' movement from the valence band to the conduction band. However, in insulators, there is no movement of the electrons due to large energy barriers, so they do not

conduct electricity [7].

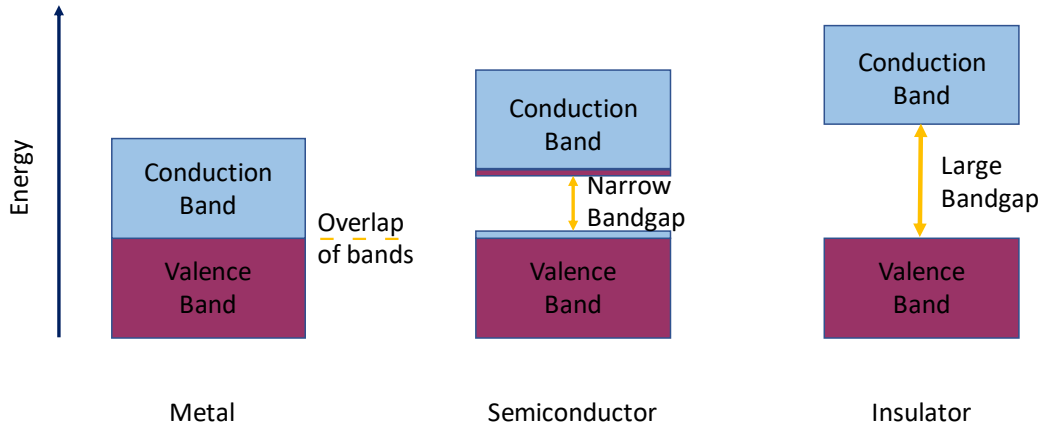

Figure 1.3: MO energy levels show distinctive band gaps for the metal, semiconductor, and insulator.

1.4 Modification of Band gap

Conjugated polymers are mostly considered as semiconductors. The conductivity of these semiconductors is related to their band gap. Their conductivity increases as the band gap decreases [8]. Scientists aim to harvest light as high as possible. Therefore, scientists determine some parameters to narrow the band gap. These parameters are bond length alternation, aromaticity, donor-acceptor approach, planarity, and substituent effect (Figure 1.4). In addition, the band gap is obtained by the contribution of these parameters.

$E_g = E_{Bla} + E_{Res} + E_\theta + E_{Sub} + E_{int}$

In which E_g resembles band gap, E_{Bla} resembles bond length alternation, E_{Res} resembles aromaticity, E_θ resembles planarity, E_{Sub} resembles substituent effect, and E_{int} resembles intermolecular interactions [**?**].

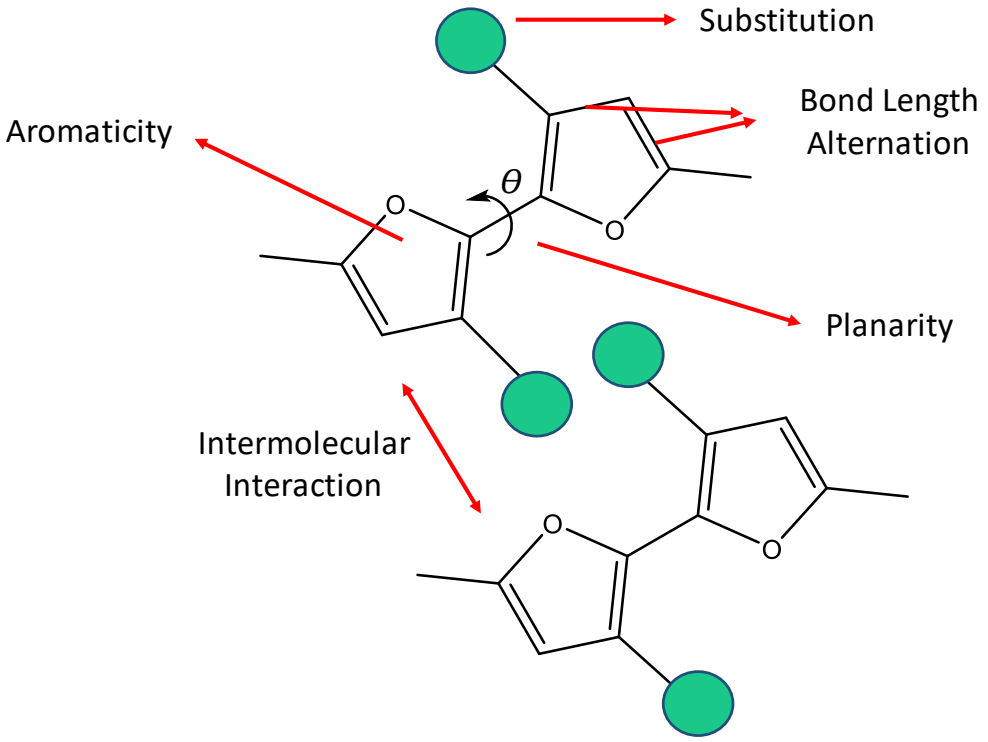

Figure 1.4: Parameters that alter band gap of the conjugated polymers.

1.4.1 Bond Length Alternation Effect

There are two forms of conjugated polymers, namely aromatic and quinoid forms. When the π-electrons delocalize, single bonds turn into double bonds, and double bonds turn into single bonds. In this way, the aromatic form turns into a quinoid form [9]. To illustrate, the aromatic and quinoid forms of polythiophene and polythiadiazole are represented (Figure 1.5). The aromatic form is a more stable and favorable form than the quinoid form. Therefore, bond length alternation energy (E_{Bla}) for an aromatic form is higher for the conversion into quinoid form. This effect directly changes the band gap energy (E_g). Conversion into quinoid form yields lower E_{Bla} and, therefore, lower E_g [10].

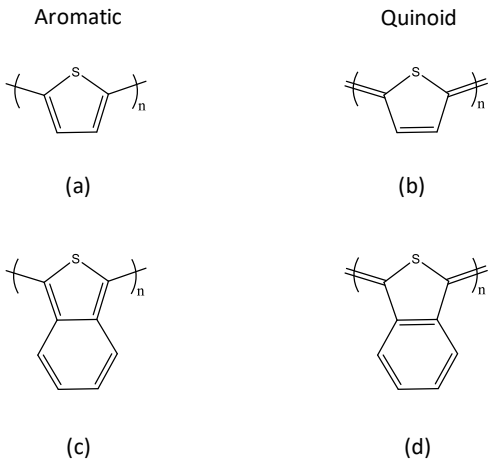

Figure 1.5: (a) and (c) illustrate an aromatic form, and (b) and (d) illustrate a quinoid form of the polythiophene and polybenzothiadiazole.

1.4.2 Aromaticity Effect

When the aromaticity of the monomer increases, the energy stabilization increases. Therefore, the delocalization of the π-electrons along the skeleton decreases, which results in a larger separation of HOMO and LUMO energy levels. In other words, higher E_g [11].

1.4.3 Planarity Effect

The fully planar conjugated polymers result in a low band gap thanks to electron delocalization along the backbone. If the conjugated polymers have a nonplanar structure, the ring plain's angular torsions can interrupt the conjugation. Aromatic heterocycles such as thiophene, furan, pyrrole, and selenophene are incorporated into conjugated polymers in order to enhance planarity [12].

1.4.4 Substituent Effect

One of the modification techniques to adjust the band gap of conjugated polymers is to incorporate the substituents. The substituents are either electron-donating groups (EDG) or electron-withdrawing groups (EWG). These substituents significantly impact the absorption, emission properties, and chemical reactivity of the conjugated molecules. In addition, they can change the HOMO and LUMO energy levels of the conjugated polymers [13]. Electron donating groups (EDG) donate π-electrons to the system and increase the reactivity, raising the HOMO level. On the other hand, electron-withdrawing groups (EWG) withdraws π-electrons from the system and decreases reactivity, which lowers the LUMO level [14].

1.4.5 Intermolecular Interaction Effect

Intermolecular interactions have a significant effect on band gap. While designing conjugated polymers, π-stacking units are preferred. These π-stacking units provide ordered structure, and higher delocalization of electrons results in a low band gap. However, conjugated polymers that have a more ordered structure can face solubility problems in common solvents [15].

1.5 Donor-Acceptor Concept

In 1993 a new strategy for tuning the band gap, the donor-acceptor concept, was introduced by Havinga and coworkers. They used squaric acid and croconic acid as acceptor units and heterocycle bearing nitrogen and sulfur atoms as the donor units. They achieved band gaps lower than 0.5 eV and intrinsic conductivities up to 10^{-5} S/cm [16]. In this concept, donor and acceptor groups are incorporated alternatively on the conjugated polymer skeleton leads to broad valence and conduction band and higher intrinsic conductivities. When the electronegativity difference increases between donor and acceptor groups, the band gap becomes narrower. In this concept,

the HOMO and LUMO energy level of the conjugated polymer is formed by the HOMO energy level of the donor and LUMO energy level of the acceptor unit [17].

1.6 Doping Process

Conjugated polymers are organic semiconductors with alternating single and double bonds in their skeleton. In their ground states, π-electrons are localized along with the skeleton, and they cannot conduct electricity. When the conjugated polymer is doped, free charge carriers are formed, which are called polaron and bipolaron (Figure 1.6). Thanks to the doping process, these π-electrons are delocalized and able to conduct electricity. The removal of an electron from the highest occupied molecular orbital is called p-type doping. The introduction of an electron to the lowest unoccupied molecular orbital is called n-type doping [18]. Conjugated polymers can be doped by two mechanisms, namely electrochemical and chemical mechanisms. Oxidation-reduction reactions are applied in both of these mechanisms. In the electrochemical mechanism, voltage is used in order to dope conjugated polymers. When a positive voltage is used, p-type doping is obtained. On the contrary, n-type doping is obtained when a negative voltage is used. In the chemical mechanism, conjugated polymers are p-doped when exposed to oxidants, which are generally halogens like iodine and bromine. However, they are n-doped when it is exposed to reductants which are generally alkali metals [19].

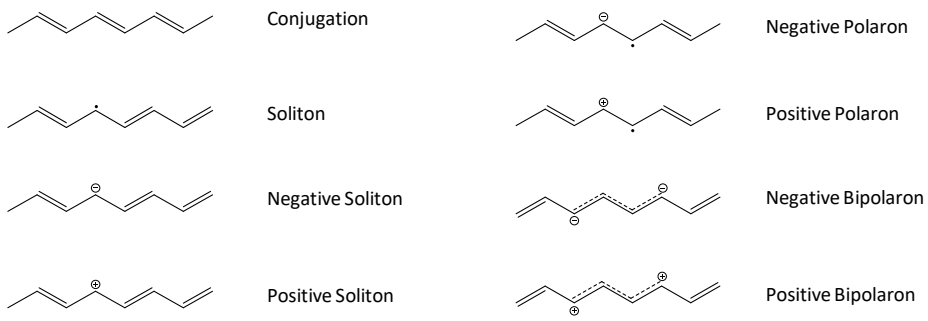

Figure 1.6: Free charge carriers.

1.7 Polymerization Methods

Electrochemical polymerization and chemical polymerization are two general methods for synthesizing conjugated polymers. There are some differences between these methods. Even tough electrochemical polymerization provides a rapid reaction and high purity, chemical polymerization is the most effective method to obtain a large scale of conjugated polymers [20]. The most widely used chemical polymerization methods are Oxidative polymerization, Suzuki-Miyaura cross coupling, Stille cross coupling, and Sonogashira cross coupling.

1.7.1 Electrochemical polymerization

There are two routes to synthesize the conjugated polymers in an electropolymerization: anodic and cathodic routes. Among these, the most used method is the anodic method. It has remarkable advantages over chemical polymerizations such as no need for a catalyst, easily tuning of the film thickness, mild reaction conditions, and no further purification. In this method, the monomer's oxidation by applying potential resulted in a chain growth deposited on the anode electrode surface. For the polymerization, monomer, supporting electrolyte (anionic salt), suitable solvent/ solvent couple are needed. Common solvents are acetonitrile, nitromethane, propylene carbonate and common salts are tetrabutylammonium hexafluorophosphate, sodium perchlorate and lithium perchlorate. These solvents and supporting electrolytes are determined according to the oxidation potentials of the monomer. The oxidation potentials of the solvents and supporting electrolytes should be higher than the monomer otherwise, they can be oxidized before the monomer. In addition, solvents should be ionically conductive and dissolve electrolytes completely and have high permittivity. Three electrochemical techniques are potentiostatic, potentiodynamic, and galvanostatic. In a potentiostatic technique, a constant potential is applied, whereas a constant current is applied in the galvanostatic technique. Unlike the others, in potentiodynamic technique, both current and voltage vary. Electrochemical polymerization is carried out with a three-electrode cell system. The electrodes are working electrode, counter electrode, and reference electrode [21]. The mechanism of the electrochem-

ical polymerization starts with the oxidation of the monomer that generates radical cation. It is followed by the coupling of two radicals to create a dication dimer. After removal of the two-hydrogen atom and rearrangement, the desired dimer product is obtained (Figure 1.7). When the potential application continues, the same mechanism is performed, and the chain grows to form the polymer [22].

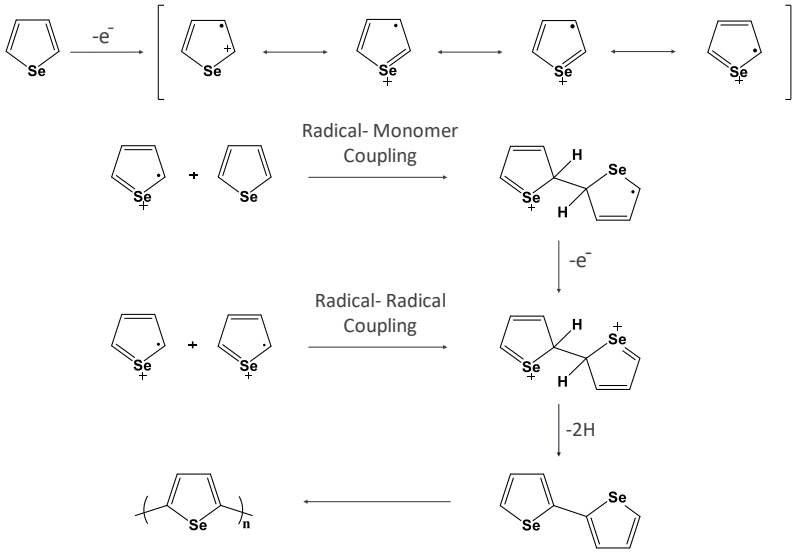

Figure 1.7: Mechanism for the electropolymerization of the selenophene.

1.7.2 Oxidative polymerization

Oxidative polymerization can be described as the removal of the two hydrogen atoms from monomer to yield polymer in the presence of Lewis acid catalysts such as $FeCl_3$, $AlCl_3$, and $Cu(ClO_4)$. Hence, it can be considered a polycondensation reaction. For this polymerization method, the most functional monomers are aromatic molecules such as phenols, aromatic hydrocarbon compounds, and heterocyclic aromatic compounds [23]. Oxidative polymerization provides a more atom-economical and cleaner way to obtain high molecular weight polymers by the formation of C–C bonds [24].

1.7.3 Stille Cross-Coupling

In 1977 John Kenneth Stille discovered one of the most famous palladium-catalyzed cross-coupling reactions; Stille Coupling. This versatile, highly specific, and selective carbon-carbon bond-forming reaction takes all the attention. Since it has mild reaction conditions compared to old Heck coupling and can tolerate different functional R-groups, it allows the formation of multi-functionalized chemical structures with high yields. Moreover, Stille coupling can be applied to form an intramolecular carbon-carbon bond. In this way, five, six-membered heterocyclic compounds can also be obtained. The main drawback of this reaction is the use of poisonous tin chemicals. In general, the Stille coupling takes place between stannyl and electron-deficient halide organic molecules in the presence of a palladium catalyst [25]. The commonly preferred catalysts are $Pd(PPh_3)_4$, $Pd(PPh_3)_2Cl_2$, and $Pd(dba)_2$, and solvents are dry toluene and THF [26].

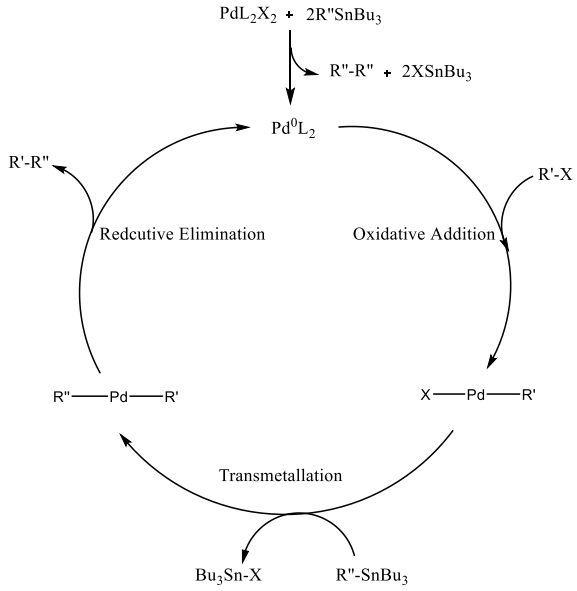

Figure 1.8: Reaction mechanism for the Stille cross-coupling.

The mechanism for Stille coupling was simplified in three main reactions, which are oxidative addition, transmetallation, and reductive elimination, respectively. In the first reaction, the oxidative addition of electron-deficient alkyl halide (R'-X) to Pd (0) is observed to produce Pd (II) complex. This complex undergoes transmetalla-

tion, and during the reaction, Sn-R" and X-Pd-R' form a four-membered ring and, the cleavage of Sn-R" and X-Pd bonds yields Sn-X and Pd-R" bond formation. Finally, the reductive elimination reaction produces R'-R" product and Pd (0) complex to complete the catalytic cycle (Figure 1.8) [27].

1.7.4 Suzuki-Miyaura Cross-Coupling

Suzuki Coupling is one of the carbon-carbon bond formation reactions which occurs between organoboron and halide compounds in the presence of base and palladium catalyst. The features like water stability, non-toxic reactants, stable organoboron compounds, the high selectivity of the reaction, and tolerance to different functional groups make the Suzuki coupling preferable [28].

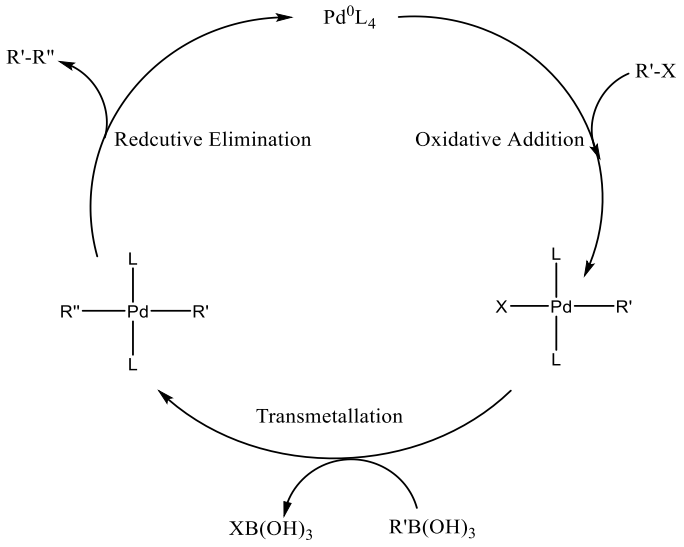

Figure 1.9: Reaction mechanism for the Suzuki-Miyaura cross-coupling.

The reaction mechanism for Suzuki coupling is composed of oxidative addition, transmetallation, and reductive elimination reactions. Unlike Stille coupling, the rate-determining step is oxidative addition. In this step, the oxidative addition of the halide compound to the palladium catalyst produces Pd (II) complex. In the presence of a base, the organoborane compound reacts with this complex, and the transmetalla-

tion reaction is completed. Finally, reductive elimination reaction generates of Pd (0) complex and Suzuki product (Figure 1.9) [29]. For Suzuki coupling, different types of bases are available, and one of them is K_2CO_3. The most commonly preferred catalysts are $Pd(PPh_3)_4$ and $Pd(PPh_3)_2Cl_2$ due to air stability, and readily reduction to Pd(0). For the halides, the reactivity of I is higher compared to Br and Cl [30].

1.7.5 Sonogashira Cross-Coupling

Sonogashira coupling is one of the most popular cross-coupling reactions to form a carbon-carbon bond between terminal alkynes and vinyl or aryl halides. The reaction runs in the basic medium, and triethylamine, pyrrolidine, K_2CO_3, and $NaHCO_3$ are mostly preferred bases. The suitable palladium catalysts are $PdCl_2$, PdI_2, and $Pd(OAc)_2$ [31]. The second catalyst is needed for this reaction, which is usually copper salts such as copper iodide. For the alkyl halides, generally, aryl or vinyl iodide is preferred since the reactivity of aryl or vinyl iodide is higher compared to bromide or chloride [32]. Therefore, the availability of chemicals and mild reaction conditions makes the Sonogashira coupling quite useful for the synthesis of many products such as pharmaceuticals, nanomaterials, and polymers.

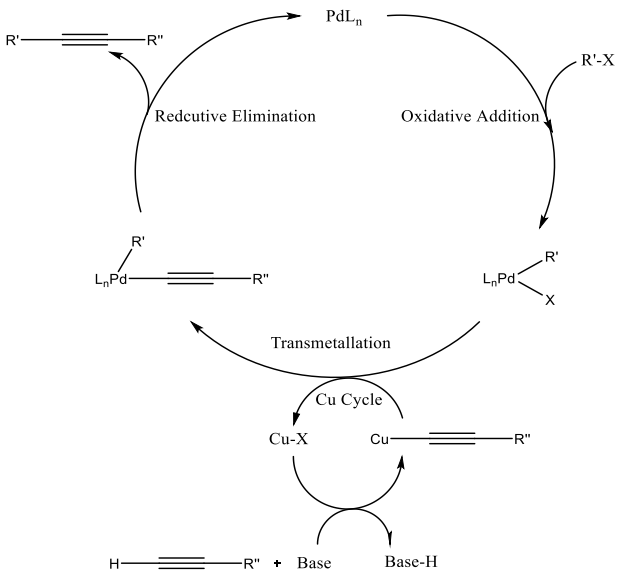

Figure 1.10: Reaction mechanism for the Sonogashira cross-coupling.

As with Suzuki and Stille couplings, the catalytic cycle includes oxidative addition, transmetallation, and reductive elimination. The first step is the activation of the palladium catalyst to produce of Pd (0) complex, which is then used in oxidative addition to aryl or vinyl halide. The produced Pd (II) complex reacts with copper Iodide generates another complex, and transmetallation completes. Finally, the desired product is obtained by reductive elimination (Figure 1.10) [33].

1.8 Organic Solar Cells

In recent years, the demand for energy resources has been increasing rapidly, and classical resources such as fossil fuels cause many environmental problems. Therefore, the interest in renewable energy sources rises. One of the most abundant renewable energy sources in our world is sunlight [34]. Converting sunlight into electrical energy by using photovoltaic cells is one of the most preferred technology. For this purpose, many organic and inorganic materials are prepared. In literature, inorganic material based solar cells shows higher efficiencies compared to their organic counterparts. However, organic materials are cheap, which makes them even more attractive for solar cell applications. Furthermore, they are flexible, lightweight, and they can absorb a large amount of light. Moreover, the band gap of the organic molecules can be tuned by molecular modifications [35].The disadvantage of these materials is that they show lower device performance and instability.

1.8.1 Working Principle of Organic Solar Cells

Solar cells use the sun's energy to produce electricity. This process can be described in 5 steps. When the sufficient energy of light is absorbed by the solar cell, electrons excite from the highest occupied molecular orbital to the lowest unoccupied molecular orbital to generate exciton. Exciton is a combination of electron and hole. Then, exciton diffuses through the donor-acceptor interface, and exciton dissociation occurs into free charges. This process takes a certain amount of time, which is called the exciton lifetime. Then, holes move through the donor layer, and electrons move through

the acceptor layer. Finally, holes are collected in the anode, electrons are collected in the cathode, and electricity is generated [36, 37].

- Absorption of photons
- Generation of exciton
- Exciton diffusion through interface between two semiconductors
- Exciton dissociation
- Charge transfer to corresponding electrodes (Figure 1.11)

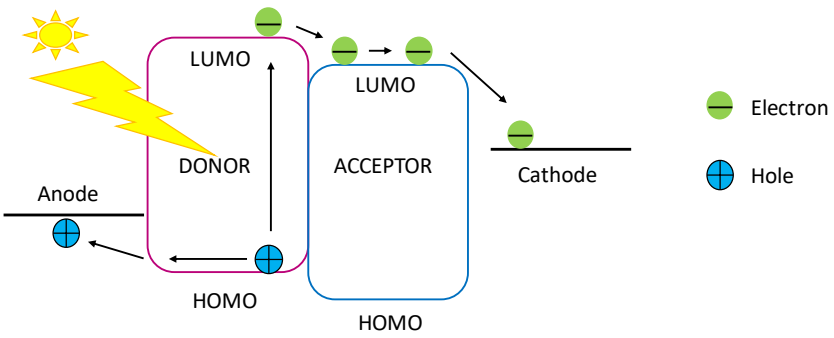

Figure 1.11: Working principle of organic solar cells.

1.8.2 Construction of Organic Solar Cell Devices

The advantages of organic solar cells have attracted considerable attention in both academia and industry. Different device architectures are constructed in order to increase power conversion efficiencies, such as a single layer, bilayer, bulk heterojunction, tandem, and inverted organic solar cells. The highest efficiencies are achieved by using tandem solar cells [38].

1.8.2.1 Single Layer Organic Solar Cells

In this solar cell type, the active material is sandwiched between anode and cathode electrodes, which have different work functions. The active material is generally polymers or small molecules (Figure 1.12). Their power conversion efficiencies are low compared to other device architectures. Due to the electric field between anode and cathode, these low efficiencies are sometimes insufficient to split excitons into holes and electrons. In addition, holes and electrons are recombined before reaching to electrodes [39].

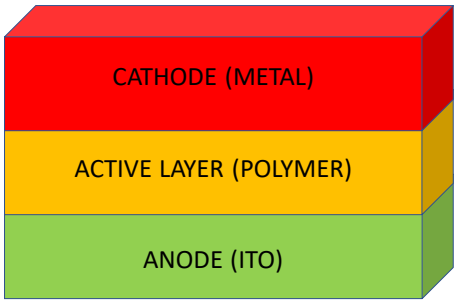

Figure 1.12: Construction of single layer solar cell device.

1.8.2.2 Bilayer Organic Solar Cells

In a bilayer architecture, two layers are composed of donor and acceptor materials positioning between the anode and cathode electrodes (Figure 1.13). The donor and acceptor layers have different electron affinities. Hence, electrostatic forces are produced at the interface between these layers. The power conversion efficiency is relatively low due to exciton dissociation occurring in the small heterojunction area. Furthermore, low mobility and unbalanced charge transport in the bilayer structure decreases efficiency [40].

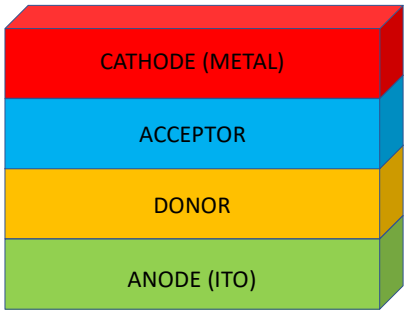

Figure 1.13: Construction of bilayer solar cell device.

1.8.2.3 Bulk-Heterojunction Organic Solar Cells

Bulk heterojunction solar cells are made up of many different layers. Light is absorbed by the active layer, which contains donor and acceptor materials. Conjugated polymers, pigments, and oligomers are used as donor materials, whereas fullerene derivatives are used as acceptor materials. The active layer is placed between the anode and cathode electrodes. Interfacial layers, which are the hole transport layer and electron transport layer, are placed between anode-active and cathode-active layers, respectively (Figure 1.14). With this architecture, it is aimed to create stable and high-performance devices. In this device, the donor generally absorbs photon and electron is excited from HOMO to LUMO. The difference between HOMO and LUMO energy levels must lie 0.1–1.4 eV range to form electron-hole pairs. These electron-hole pairs diffuse through the donor-acceptor interface in which they split into free charges. Then, electrons move through the cathode, and holes move through the anode [41].

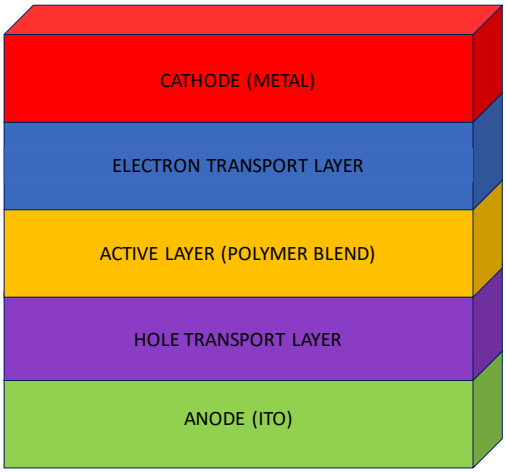

Figure 1.14: Construction of bulk-heterojunction solar cell device.

1.9 Characterization of Organic Solar Cell Devices

In order to characterize organic solar cells, the voltage-current (J-V) curve is applied. In addition, the performance of the organic solar cell is determined by some parameters. These parameters are power conversion efficiency (PCE), fill factor (FF), open-circuit voltage (V_{OC}), and short-circuit voltage (J_{SC}). Power conversion efficiency can be described as solar cell efficiency, which is the ratio of maximum power produced to the incident radiant energy [42]. Short-circuit current is known as the current generated by the organic solar cell when exposed to sunlight in the absence of external potential. It can also be defined as a maximum produced a photocurrent. Open circuit voltage is the measured potential under sunlight if no current flow occurs in the organic solar cell. Fill Factor is the ratio of maximum power produced by the organic solar cell to the product of open-circuit voltage (V_{OC}) and short-circuit current (J_{SC}) [43] (Figure 1.15).

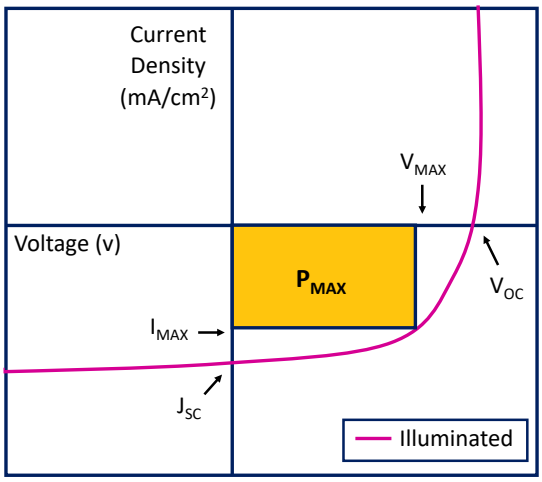

Figure 1.15: Current Density-voltage characteristic of organic solar cells under durak and illuminated.

1.10 Benzothiadiazole Moiety

Benzothiadiazole is one of the most used acceptor units, which has a planar heterocyclic structure. It contains an imine (-C=N-) bond, which stands out with good electron-withdrawing ability. To improve the performance of benzothiadiazole, different substituents can be added, such as fluorine atom. In literature, fluorine atom incorporated polymers shows higher short circuit current and power conversion efficiency. Furthermore, it has lower HOMO and LUMO levels that exhibit good thermal and oxidative stability compared to nonfluorinated ones. In addition, the fluorine atom has tremendous features like being the most electronegative element in the periodic table and the smallest electron-withdrawing group. Its small size reduces the steric hindrance of the structure. Moreover, the fluorine atom can form noncovalent interactions such as C-F···H and F···S. Therefore, all these features make the fluorinated benzothiadiazole moiety a strong candidate for the synthesis of conjugated polymers [44, 45].

1.11 Fluorene Moiety

Fluorene derivatives are one of the most preferred donor units for the design of organic electronics since the fluorene structure plays a significant role in modifying the band gap. It is composed of conjugated aromatic biphenyl rings that have electron-rich nature. This nature provides a larger absorption wavelength and lower oxidation potential [46]. Even though it has a rigid, planar structure when the fluorene is coupled with acceptor units, the quinoid structure is favored. Therefore, it provides a narrower band gap [47]. In addition, it shows properties like chemically and thermal stability, electron-donating ability. The active positions of the fluorene unit are 2,7 and 9 positions to give reactions. Generally, alkyl groups are substituted from position 9 and these alkyl groups make a significant contribution to the solubility and processibility [48].

1.12 Bridging Units

Research groups have carried out many studies in order to tune the new band gap of the conjugated polymers. However, the modifications made on donor and acceptor units became insufficient over time. Therefore, scientists introduced new methods such as incorporating π-bridges. These bridging units are generally aromatic heterocyclic compounds such as thiophene, selenophene, furan, thieno[3,2-b]thiophene. Incorporation of the π-bridges can affect the electronic structure and interaction between donor and acceptor units. Therefore, they can change electrochemical, optical, intermolecular charge transport, and photovoltaic properties conjugated polymers [49]. These bridges can provide low band gap conjugated polymers that can absorb both the spectrum's visible and Near-IR region. They can also make a contribution to increasing intermolecular charge transport, which provides higher molar absorptivity [50].

1.13 Aim of the Study

The control of the band gap in conjugated polymers made them more popular over the years. When the low band gap conjugated polymers were prepared, they can be used in many application areas like organic solar cell device construction. In order to achieve low band gap CP, the D-A strategy can be applied. For this reason, strong acceptor moiety, namely, benzothiadiazole comprising polymers, were prepared. To enhance its electron withdrawing ability, a fluorine atom was substituted. Furthermore, an oxygen atom with a branched alkyl unit was also substituted to increase both molecular weight and solubility of the polymer. As a result, novel 4,7-dibromo-5-fluoro-6-((2-octyldodecyl)oxy)benzo[c][1,2,5]thiadiazole acceptor moiety was prepared. This acceptor moiety was coupled with different donors like thiophene, thienothiophene, 3-hexylthiophene and furan, and resulted monomers were electropolymerized. Electrochemical and spectroelectrochemical properties of the homopolymers were revealed that they have narrow band gap and low-lying HOMO and LUMO energy levels. Besides, they exhibited multielectrochromic properties in their neutral and doped states.

As mentioned above, CP with a narrow band gap has potential applications like OSC device construction. Therefore, novel 4,7-dibromo-5-fluoro-6-((2-octyldodecyl)oxy) benzo[c][1,2,5]thiadiazole was coupled with a strong donor moiety fluorene, and as spacer thiophene, thienothiophene, 3-hexylthiophene and selenophene were used. They showed broad absorption in the spectrum with a narrow band gap. Therefore, they were strong candidates for the OSC application. Besides, they exhibited multielectrochromic properties in their neutral, oxidized, and reduced states, which means they are also promising for electrochromic device construction.

CHAPTER 2

EXPERIMENTAL

2.1 Chemicals and Equipments

For the synthesis, all the chemicals were purchased from Sigma-Aldrich except for 4,5-difluoro-2-nitroaniline was purchased from Tokyo Chemical Industry (TCI). Dry solvents were dispensed from an MB-SPS-800 solvent drying system. Column chromatography runs by using Merck Silica Gel 60 with the pore size 0.040-0.063 mm. Homopolymerization of the monomers was performed by electropolymerization in a three-electrode cell system. These electrodes were platinum wire used as the counter electrode, the silver wire used as the reference electrode, and Indium Tin Oxide (ITO) coated glass used as the working electrode. All electrochemistry studies were run by using GAMRY Reference 600 potentiostat. Electropolymerization medium consisted of tetrabutylammonium tetrafluoroborate salt in an acetonitrile/ dichloromethane solution. Cyclic voltammetry was used to determine oxidation and reduction potentials. Perkin Elmer Lambda 25 UV/Vis Spectrometer was utilized to determine spectroelectrochemical features. The ^{1}H and ^{13}C spectra of the synthesized chemicals were assigned by Bruker Spectrospin Avance DPX-400 Spectrometer. HRMS measurements were performed by Waters Synapt G1 High Definition Mass Spectrometer.

2.2 Computational methods

Theoretical calculations were carried out for tetramers of PTBTT, PHTBTHT, PFBTF and PTTBTTT in the form of DADADADA (D: donor, A: acceptor) by using

B3LYP hybrid functional and 6-311G(d) basis set with tight SCF convergence criteria in the Gaussian09 (Revision A.02) software package [51, 52, 53]. Adequate agreement was achieved with experimental results previously at this level of calculations for donor-acceptor copolymer studies [54, 55, 56]. Alkyl side chains on the polymers were replaced with ethyl groups to increase computational efficiency. Geometry optimizations were started from different initial conformations by controlling the torsional angle between connected donor and acceptor units to determine lowest energy geometry. Electrostatic potential surface (ESP), highest occupied molecular orbitals (HOMO), and lowest unoccupied molecular orbitals (LUMO) were calculated for the optimized geometries of tetramers. Band gap was calculated by using two different methods that are direct difference between the HOMO energy and LUMO energy for the optimized ground state and the calculation vertical excitation energy of the lowest singlet excited state ($S_0 \rightarrow S_1$). The singlet excited states of the oligomers were calculated by using time-dependent density-functional theory (TDDFT) at the same level of calculation quality. Vertical ionization potential (VIP) and adiabatic ionization potential (AIP) were calculated by the energy difference between the neutral tetramer and cation state of the optimized ground state geometry, followed by optimized cation geometry, respectively. Hole reorganisation energies (λreorg) were determined based on the formulation by Bredas et al [57]. Atomic charges were calculated based on the ESP fitting scheme of Merz-Singh-Kollman (MK) [58].

2.3 General Synthetic Pathway for Monomers

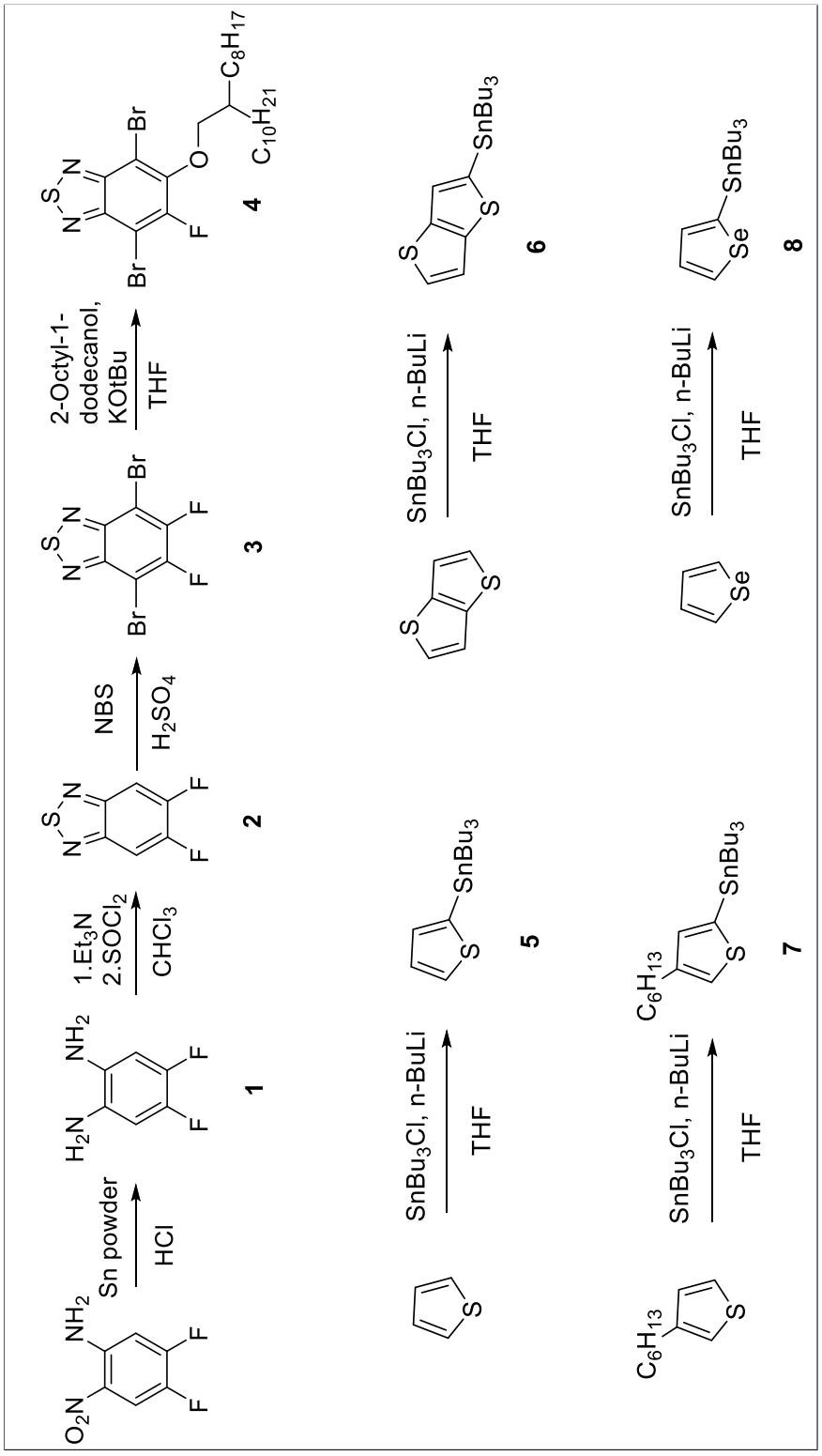

Figure 2.1: Synthetic pathway for monomers part I.

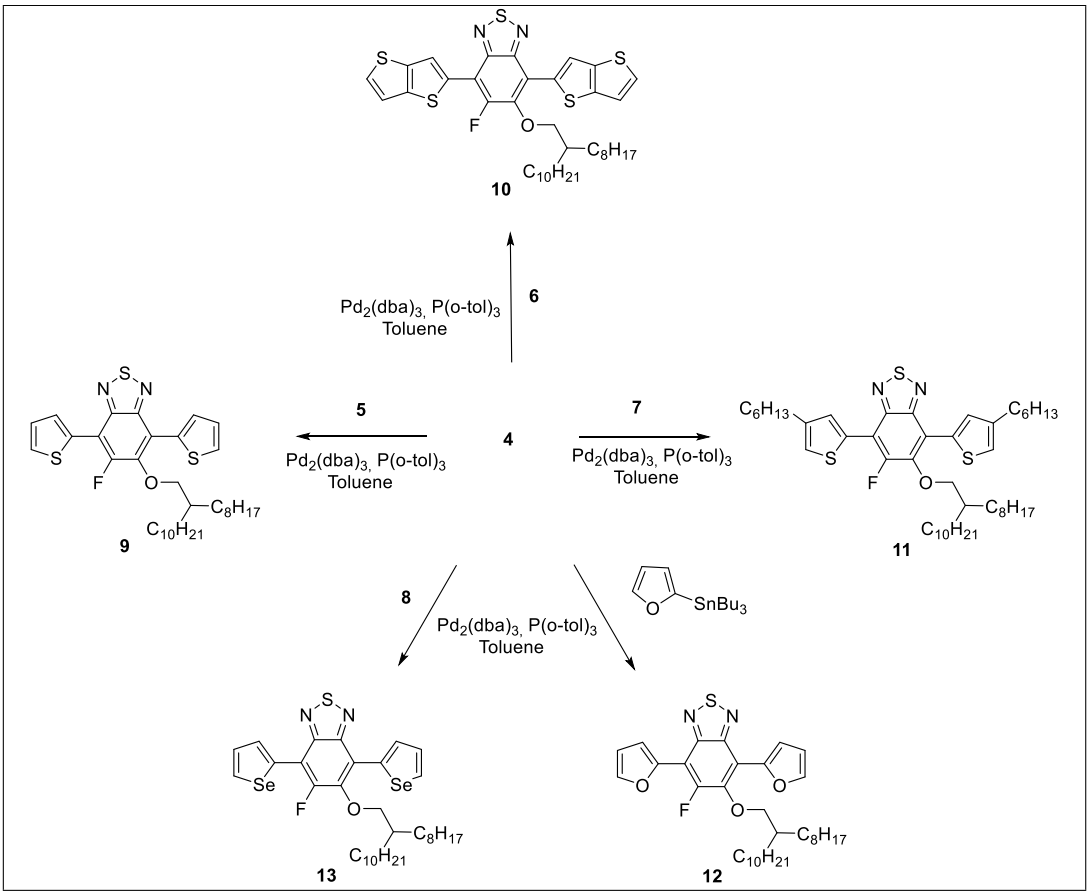

Figure 2.2: Synthetic pathway for monomers part II.

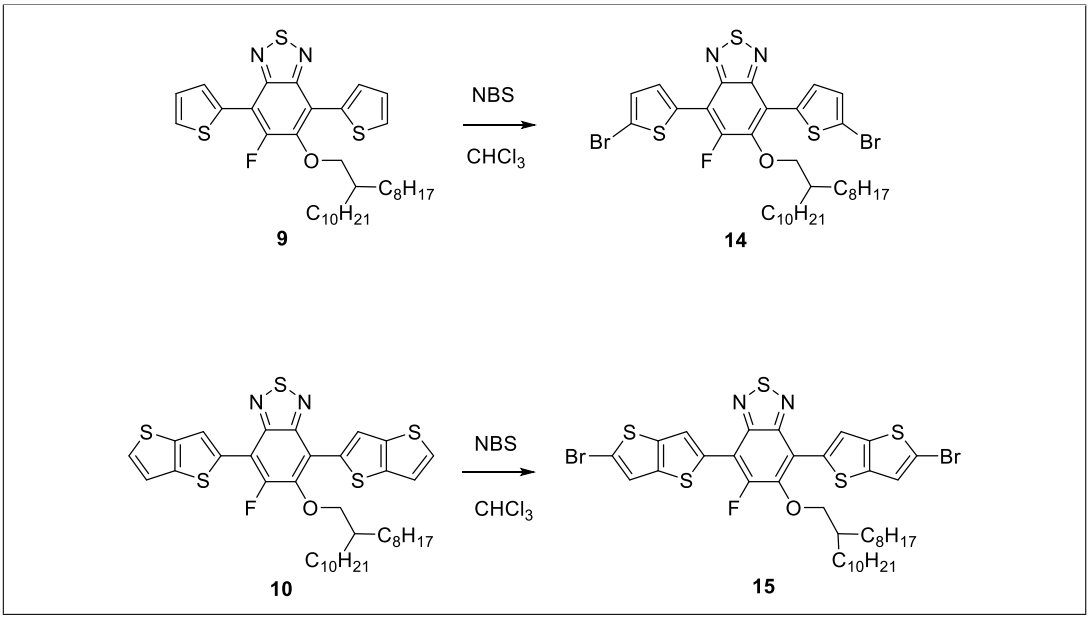

Figure 2.3: Synthetic pathway for monomers part III.

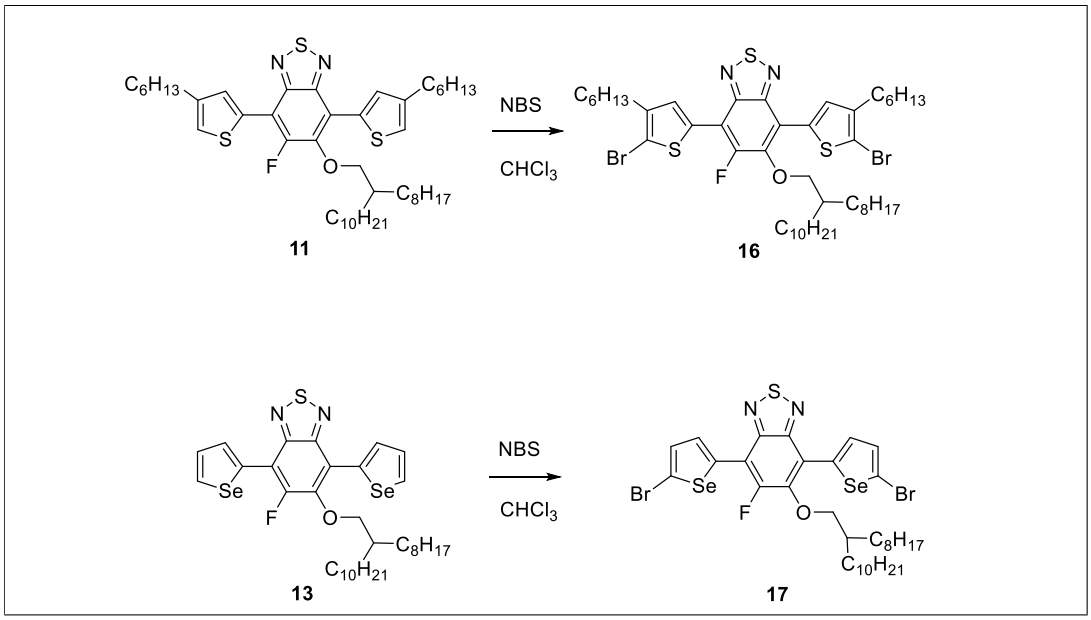

Figure 2.4: Synthetic pathway for monomers part IV.

2.4 Synthesis of Monomers

2.4.1 Synthesis of 4,5-difluorobenzene-1,2-diamine (1)

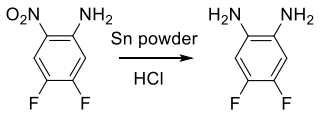

Figure 2.5: Synthetic pathway for 4,5-difluorobenzene-1,2-diamine.

4,5-Difluoro-2-nitroaniline (1.25 g, 7.18 mmol) and 12 M HCl (30 mL) were mixed under nitrogen atmosphere. The reaction medium was cooled to 0 °C, and the tin powder (4.13 g, 34.7 mmol) was added in three portions. After the depletion of tin powder at room temperature, the reaction mixture was poured into 100 mL of pure water. Then, NaOH was added until adjusting pH to 10. The phase was extracted with ethyl acetate and washed with brine and pure water. The organic layers were combined and dried over anhydrous $MgSO_4$. The white cotton solid was obtained after the removal of the solvent by rotary evaporation. The yield was 78%. ^{1}H NMR (400 MHz, $CDCl_3$) δ 6.51 (t, J = 9.5 Hz, 2H), 3.28 (s, 4H). ^{13}C NMR (100 MHz,

$CDCl_3$) δ 145.2, 145.0, 142.8, 142.6, 130.6, 130.5, 105.4, 105.3, 105.3, 105.2.

2.4.2 Synthesis of 5,6-difluorobenzo[c][1,2,5]thiadiazole (2)

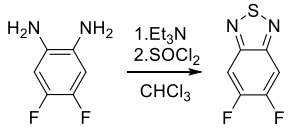

Figure 2.6: Synthetic pathway for 5,6-difluorobenzo[c][1,2,5]thiadiazole.

4,5-Difluorobenzene-1,2-diamine (1.70 g, 11.8 mmol) and triethylamine (6.58 mL, 47.1 mmol) were dissolved in 60 mL of $CDCl_3$ in a two-necked flask under an inert atmosphere. When the reaction mixture's temperature was cooled to 0 °C, $SOCl_2$ (1.72 mL, 23.5 mmol) was added drop wise. The temperature was then gradually elevated to 70 °C, and the mixture was stirred for 5 h. The organic part was washed with pure water and dried over $MgSO_4$. After removal of the $CDCl_3$ under reduced pressure, the brown solid was obtained. The yield was 63%. ^{1}H NMR (400 MHz, $CDCl_3$) δ 7.75 (t, J = 8.7 Hz, 2H). ^{13}C NMR (100 MHz, $CDCl_3$) δ 155.0 (d, J = 19.9 Hz), 152.4 (d, J = 20.0 Hz), 150.8 (t, J = 5.5 Hz), 106.1 (dd, J_1 14.8, J_2= 6.8 Hz).

2.4.3 Synthesis of 4,7-dibromo-5,6-difluorobenzo[c][1,2,5]thiadiazole (3)

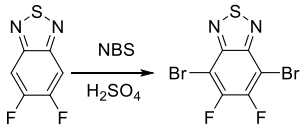

Figure 2.7: Synthetic pathway for 4,7-dibromo-5,6-difluorobenzo[c][1,2,5] thiadiazole.

5,6-Difluorobenzo[c][1,2,5]thiadiazole (3.88 g, 22.5 mmol) was dissolved in 100 mL concentrated H_2SO_4 in a two-necked flask. Then, N-bromosuccinimide (16.0 g, 90.1

mmol) was added in three portions. The reaction mixture was stirred and heated to 70°C for 8 h under cover from light. Then the reaction medium was spilled into an ice-pure water mixture to afford white precipitate. The filtered white product was washed with pure water and allowed to dry. With the evaporation of pure water, solid was recrystallized in methanol, and the white wool like product was obtained. The yield was 41%. ^{13}C NMR (100 MHz, $CDCl_3$) δ 153.0, 152.8, 150.4, 150.2, 148.7, 148.7, 99.3, 99.2, 99.2, 99.1.

2.4.4 Synthesis of 4,7-dibromo-5-fluoro-6-((2-octyldodecyl)oxy) benzo[c][1,2,5]thiadiazole (4)

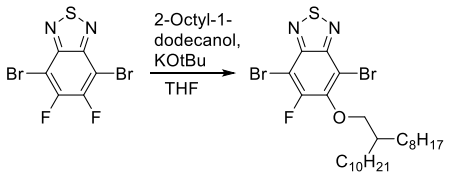

Figure 2.8: Synthetic pathway for 4,7-dibromo-5-fluoro-6-((2-octyldodecyl)oxy) benzo[c][1,2,5]thiadiazole.

4,7-Dibromo-5,6-difluorobenzo[c][1,2,5]thiadiazole (0.70 g, 2.12 mmol), 2-octyl-1-dodecanol (3.78 mL, 10.6 mmol) and KOBu^t (0.21 g, 1.91 mmol) were dissolved in 40 mL dry THF under argon atmosphere. The reaction temperature was raised to 66 °C and stirred overnight. Through evaporation of the THF under reduced pressure, the crude was washed with pure water and extracted dichloromethane. Organic phases were collected and dried with $MgSO_4$. After removing the solvent, the liquid product was purified by column chromatography on silica gel using 1.5:1 dichloromethane: hexane. The yield was 87%. ^{1}H NMR (400 MHz, $CDCl_3$) δ 4.12 (d, J = 5.1 Hz, 2H), 1.90 – 1.68 (m, 1H), 1.59 (m, 2H), 1.28 (m, 30H), 0.87 (m, J = 2.1 Hz, 6H). ^{13}C NMR (100 MHz, $CDCl_3$) δ 157.9, 155.3, 150.0, 149.6, 149.4, 149.0, 149.0, 105.9, 105.8, 98.6, 98.4, 78.1, 78.0, 39.1, 31.9, 31.9, 31.0, 29.9, 29.6, 29.6, 29.6, 29.3, 29.3, 26.8, 22.6.

2.4.5 Synthesis of tributyl(thiophen-2-yl)stannane (5)

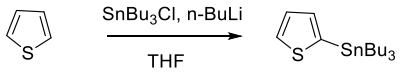

Figure 2.9: Synthetic pathway for tributyl(thiophen-2-yl)stannane.

Thiophene (2.00 g, 23.7 mmol) was dissolved in freshly distilled THF under argon atmosphere. The reaction medium was cooled to -78 °C, and n-butyl lithium (10.4 mL, 2.5 M in hexane, 26.1 mmol) was added drop wise. This solution was stirred for 2 h under an inert atmosphere at the same temperature. Then tributyltin chloride (7.09 mL, 26.1 mmol) was added drop wise. The reaction mixture was gradually reached room temperature and stirred overnight. After removing the solvent under reduced pressure, the organic layer was extracted with dichloromethane and washed with brine and pure water three times. Organic phases were combined and dried over $MgSO_4$. The product was concentrated on a rotary evaporator, and the light-yellow liquid was obtained. The yield was 85%. ^{1}H NMR (400 MHz, $CDCl_3$) δ 7.57 (d, J = 4.7 Hz, 1H), 7.20 – 7.17 (t, 1H), 7.12 (d, J = 3.2 Hz, 1H), 1.49 (m, 6H), 1.27 (t, J = 14.7, 6H), 1.11 – 0.97 (m, 6H), 0.82 (t, J = 7.3 Hz, 9H). ^{13}C NMR (100 MHz, $CDCl_3$) δ 136.1, 135.1, 130.5, 127.8, 28.9, 28.8, 27.5, 27.2, 13.6.

2.4.6 Synthesis of tributyl(thieno[3,2-b]thiophen-2-yl)stannane (6)

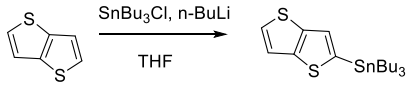

Figure 2.10: Synthetic pathway for tributyl(thieno[3,2-b]thiophen-2-yl)stannane.

Thieno[3,2-b]thiophene (0.70 g, 4.99 mmol) was dissolved in freshly distilled THF under an inert atmosphere. The reaction medium was cooled to -78 °C, and n-butyl lithium (2.20 mL, 2.5 M in hexane, 5.49 mmol) was added drop wise. This solution

was stirred for 2 h under an inert atmosphere at the same temperature. Then tributyltin chloride (1.49 mL, 5.49 mmol) was added drop wise. The reaction mixture was gradually reached room temperature and stirred overnight. After removing the solvent under reduced pressure, the organic layer was extracted with dichloromethane and washed with brine and pure water three times. Organic parts were combined and dried over $MgSO_4$. The product was concentrated on a rotary evaporator, and the light-yellow liquid was obtained as the product. The yield was 50%. ^{1}H NMR (400 MHz, $CDCl_3$) δ 7.38 (d, J = 5.0 Hz, 1H), 7.33 (s, J = 5.1 Hz, 1H), 7.23 (d, J = 5.2 Hz, 1H), 1.65 – 1.52 (m, 12H), 1.35 (m, 6H), 1.19 – 1.08 (m, 6H), 0.90 (t, J = 7.3 Hz, 9H). ^{13}C NMR (100 MHz, $CDCl_3$) δ 136.0, 135.0, 130.4, 127.7, 28.8, 27.1, 13.5, 10.7.

2.4.7 Synthesis of tributyl(4-hexylthiophen-2-yl)stannane (7)

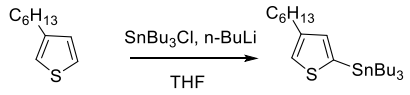

Figure 2.11: Synthetic pathway for tributyl(4-hexylthiophen-2-yl)stannane.

3-Hexylthiophene (2.50 g, 14.8 mmol) was dissolved in freshly distilled THF under an inert atmosphere. The reaction medium was cooled to -78 °C, and n-butyl lithium (6.54 mL, 2.5 M in hexane, 16.3 mmol) was added drop wise. This solution was stirred for 2 h under an inert atmosphere at the same temperature. Then tributyltin chloride (4.43 mL, 16.3 mmol) was added drop wise. The reaction mixture was gradually reached room temperature and stirred overnight. After removing the solvent under reduced pressure, the organic layer was extracted with dichloromethane and washed with brine and pure water three times. Organic parts were combined and dried over $MgSO_4$. The product was concentrated on a rotary evaporator, and the light-yellow liquid was obtained as the product as the product. The yield was 83%. ^{1}H NMR (400 MHz, $CDCl_3$) δ 7.20 (s, 1H), 6.98 (s, 1H), 2.70 – 2.62 (t, 2H), 1.69 – 1.61 (m, 8H), 1.60 – 1.53 (m, 10H), 1.37 – 1.31 (m, 8H), 1.13 – 1.06 (m, 9H), 0.91 (t, J = 7.3 Hz, 3H). ^{13}C NMR (100 MHz, $CDCl_3$) δ 144.4, 136.8, 136.2, 125.4, 31.7,

30.6, 29.9, 29.1, 28.9, 27.2, 22.6, 14.0, 13.6, 10.7.

2.4.8 Synthesis of tributyl(selenophen-2-yl)stannane (8)

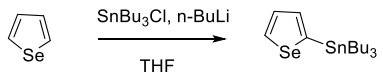

Figure 2.12: Synthetic pathway for tributyl(selenophen-2-yl)stannane.

Selenophene (2.10g g, 16.0 mmol) was dissolved in freshly distilled THF under an inert atmosphere. The reaction medium was cooled to -78 °C, and n-butyl lithium (7.05 mL, 2.5 M in hexane, 17.6 mmol) was added drop wise. This solution was stirred for 2 h under an inert atmosphere at the same temperature. Then tributyltin chloride (4.78 mL, 17.6 mmol) was added drop wise. The reaction mixture was gradually reached room temperature and stirred overnight. After removing the solvent under reduced pressure, the organic layer was extracted with dichloromethane and washed with brine and pure water three times. Organic parts were combined and dried over $MgSO_4$. The solution was concentrated on a rotary evaporator, and the light-yellow liquid was obtained as the product. The yield was 95%. ^{1}H NMR (400 MHz, $CDCl_3$) δ 8.36 (d, J = 4.3 Hz, 1H), 7.51 (d, J = 3.8 Hz, 1H), 7.49 (d, J = 3.5 Hz, 1H), 1.77 – 1.46 (m, 8H), 1.35 (t, J_1 = 14.7, 8H), 1.19 – 1.02 (m, 8H), 0.91 (q, J = 7.0 Hz, 12H). ^{13}C NMR (100 MHz, $CDCl_3$) δ 143.6, 137.9, 135.2, 130.5, 28.9, 27.8, 27.2, 13.6, 11.1.

2.4.9 Synthesis of 5-fluoro-6-((2-octyldodecyl)oxy)-4,7-di(thiophen-2-yl)benzo[c][1,2,5]thiadiazole (9)

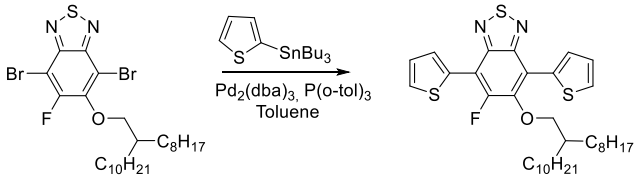

Figure 2.13: Synthetic pathway for 5-fluoro-6-((2-octyldodecyl)oxy)-4,7-di(thiophen-2-yl)benzo[c][1,2,5]thiadiazole.

4,7-Dibromo-5-fluoro-6-((2-octyldodecyl)oxy)benzo[c][1,2,5]thiadiazole (0.6 g, 0.97 mmol) and 2-(tributylstannyl) thiophene (0.81 g, 2.17 mmol) were dissolved in 40 mL dry toluene and stirred under argon atmosphere for 1 h. Then, bis(dibenzylideneacetone) palladium (0) (44.0 mg, 48.0 µmol) and tri(o-tolyl)phosphine (60.0 mg, 0.19 mmol) were added and the mixture was heated to 110 °C for 2 days under inert atmosphere. Through evaporation of the toluene under reduced pressure, the crude product was purified by column chromatography on silica gel using eluent 1:5 dichloromethane: hexane .The yield was 33%. ^{1}H NMR (400 MHz, $CDCl_3$) δ 8.41 (d, J = 3.8 Hz, 1H), 8.27 (d, J = 3.7 Hz, 1H), 7.58 (d, J = 5.2 Hz, 1H), 7.53 (d, J = 5.2 Hz, 1H), 7.24 (m, 2H), 4.00 (d, J = 5.9 Hz, 2H), 1.99 – 1.93 (m, 1H), 1.57 – 1.47 (m, 4H), 1.27 (s, 28H), 0.88 (s, 6H). ^{13}C NMR (100 MHz, $CDCl_3$) δ 156.2, 153.6, 150.3, 149.5, 149.4, 147.1, 146.9, 133.3, 133.3, 132.2, 132.1, 130.8, 130.4, 130.3, 128.1, 128.0, 127.8, 127.1, 126.8, 117.3, 111.6, 111.4, 77.8, 39.0, 31.9, 31.0, 30.0, 29.7, 29.4, 26.7, 22.7, 14.1. HRMS (ESI, m/z), $[M+H]^+$: for $C_{34}H_{48}N_2OFS_3$, calculated 615.2913 found 615.2914.

2.4.10 Synthesis of 5-fluoro-6-((2-octyldodecyl)oxy)-4,7-bis(thieno[3,2-b] thiophen-2-yl)benzo[c][1,2,5]thiadiazole (10)

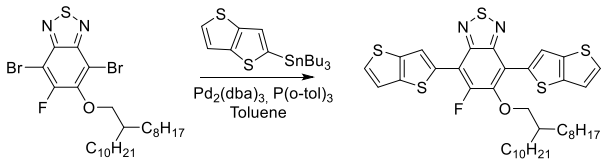

Figure 2.14: Synthetic pathway for 5-fluoro-6-((2-octyldodecyl)oxy)-4,7-bis(thieno[3,2-b]thiophen-2-yl)benzo[c][1,2,5]thiadiazole.

4,7-Dibromo-5-fluoro-6-((2-octyldodecyl)oxy)benzo[c][1,2,5]thiadiazole (0.50 g, 0.82 mmol) and tributyl(thieno[3,2-b]thiophen-2-yl)stannane (0.85 g, 2.05 mmol) were dissolved in 40 mL dry toluene and stirred under argon atmosphere for 1 h. Then, bis(dibenzylideneacetone) palladium (0) (37.5 mg, 0.81 mmol) and tri(o-tolyl)phosphine (50.0 mg, 0.41 mmol) were added and the mixture was heated to 110 °C for 2 days under inert atmosphere. The solution was concentrated on rotary evaporator and the solid product was purified by column chromatography on silica gel using eluent 1:4 dichloromethane: hexane. The yield was 50%. ^{1}H NMR (400 MHz, $CDCl_3$) δ 8.73 (s, 1H), 8.55 (s, 1H), 7.51 – 7.46 (m, 2H), 7.35 – 7.31 (m, 2H), 4.06 (d, J = 5.9 Hz, 2H), 2.05 – 1.99 (t, 1H), 1.56 (s, 4H), 1.27 (s, 28H), 0.89 (s, 6H). ^{13}C NMR (100 MHz, $CDCl_3$) δ 155.2, 152.6, 149.1, 148.3, 148.2, 146.0, 145.9, 140.7, 140.6, 138.5, 138.2, 134.4, 133.0, 127.8, 127.6, 122.2, 121.7, 121.6, 118.3, 116.6, 111.0, 110.8, 77.2, 38.0, 30.9, 29.9, 29.0, 28.7, 28.3, 25.7, 21.6, 13.1. HRMS (ESI, m/z), $[M+H]^+$: for $C_{38}H_{48}N_2OFS_5$, calculated 727.2354 found 727.2352.

2.4.11 Synthesis of 5-fluoro-4,7-bis(4-hexylthiophen-2-yl)-6-((2-octyldodecyl)oxy)benzo[c][1,2,5]thiadiazole (11)

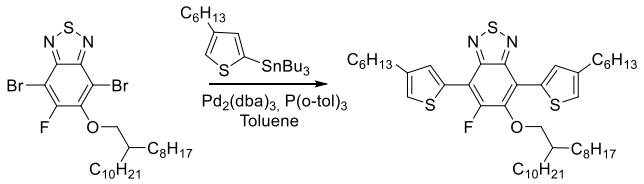

Figure 2.15: Synthetic pathway for 5-fluoro-4,7-bis(4-hexylthiophen-2-yl)-6-((2-octyldodecyl)oxy)benzo[c][1,2,5]thiadiazole.

4,7-Dibromo-5-fluoro-6-((2-octyldodecyl)oxy)benzo[c][1,2,5]thiadiazole (0.60 g, 0.97 mmol) and tributyl(4-hexylthiophen-2-yl)stannane (1.13 g, 2.47 mmol) were dissolved in 25 mL dry toluene and stirred under argon atmosphere for 1 h. Then, bis(diben- zylideneacetone)palladium (0) (44.4 mg, 0.48 µmol) and tri(o-tolyl)phosphine (60.0 mg, 0.19 mmol) were added and the mixture was heated to 110 °C for 2 days under inert atmosphere. Through evaporation of the toluene under reduced pressure, the crude product was purified by column chromatography on silica gel using eluent 1:4 dichloromethane: hexane. The yield was 41%. ^{1}H NMR (400 MHz, $CDCl_3$) δ 8.25 (s, 1H), 8.10 (s, 1H), 7.17 (s, 1H), 7.12 (s, 1H), 3.99 (d, J = 6.0 Hz, 2H), 2.80 – 2.57 (m, 4H), 1.97 (m, 2H), 1.70 (m, 6H), 1.44 – 1.35 (m, 8H), 1.27 (s, 32H), 0.97 – 0.85 (m, 6H), 0.87 (m, 6H). ^{13}C NMR (100 MHz, $CDCl_3$) δ 156.2, 153.6, 150.3, 149.5, 149.4, 147.0, 146.9, 143.3, 142.9, 133.1, 133.0, 132.2, 131.9, 131.8, 131.8, 131.7, 123.1, 123.0, 122.8, 117.3, 117.2, 111.5, 111.4, 77.8, 77.7, 39.1, 32.0, 31.8, 31.7, 31.0, 30.6, 30.5, 30.1, 29.8, 29.7, 29.7, 29.4, 29.2, 29.1, 26.8, 22.7, 22.7, 22.7, 14.1. HRMS (ESI, m/z), $[M+H]^+$: for $C_{46}H_{72}N_2OFS_3$, calculated 783.4791 found 783.4821.

2.4.12 Synthesis of 5-fluoro-6-((2-octyldodecyl)oxy)-4,7-di(selenophen-2-yl)benzo[c][1,2,5]thiadiazole (12)

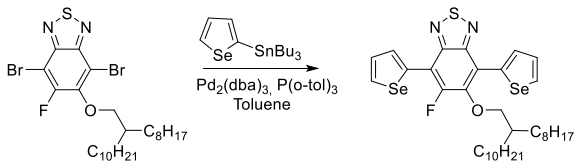

Figure 2.16: Synthetic pathway for 5-fluoro-6-((2-octyldodecyl)oxy)-4,7-di(selenophen-2-yl)benzo[c][1,2,5]thiadiazole.

4,7-Dibromo-5-fluoro-6-((2-octyldodecyl)oxy)benzo[c][1,2,5]thiadiazole (0.57 g, 0.94 mmol) and tributyl(selenophen-2-yl)stannane (0.96 g, 2.34 mmol) were dissolved in 25 mL dry toluene and stirred under argon atmosphere for 1 h. Then, bis(dibenzylideneacetone)palladium (0) (44.4 mg, 47.0 µmol) and tri(o-tolyl)phosphine (57.0 mg, 0.19 mmol) were added and the mixture was heated to 110 °C for 2 days under inert atmosphere. Through evaporation of the toluene under reduced pressure, the crude product was purified by column chromatography on silica gel using eluent 1:7 dichloromethane: hexane. The yield was 39%. ^{1}H NMR (400 MHz, $CDCl_3$) δ 8.80 (d, J = 3.4 Hz, 1H), 8.49 (d, J = 3.9 Hz, 1H), 8.30 (d, J = 5.7 Hz, 1H), 8.25 (d, J = 5.7 Hz, 1H), 7.48 (dd, J_1 = 5.7, J_2 = 4.1 Hz, 2H), 4.04 (d, J = 6.2 Hz, 2H), 2.10 – 1.99 (m, 1H), 1.65 – 1.50 (m, 4H), 1.29 (s, 28H), 0.90 (s, 6H). ^{13}C NMR (101 MHz,$CDCl_3$) δ 154.8, 154.8, 152.2, 148.6, 148.6, 148.3, 148.3, 148.2, 148.2, 145.5, 145.3, 136.4, 135.4, 135.4, 133.3, 133.2, 132.7, 132.0, 131.3, 131.2, 128.7, 128.5, 117.7, 117.7, 112.0, 111.9, 76.8, 38.0, 30.9, 29.8, 29.0, 28.6, 28.6, 28.6, 28.3, 25.6, 21.6, 13.1. HRMS (ESI, m/z), $[M+H]^+$: for $C_{34}H_{48}N_2OFSSe_2$ calculated 709.1831 found 709.1848.

2.4.13 Synthesis of 5-fluoro-6-((2-octyldodecyl)oxy)-4,7-di (furan-2-yl)benzo[c][1,2,5]thiadiazole (FBTF) (13)

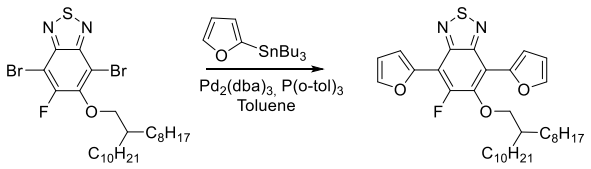

Figure 2.17: Synthetic pathway for -fluoro-6-((2-octyldodecyl)oxy)-4,7-di (furan-2-yl)benzo[c][1,2,5]thiadiazole.

4,7-Dibromo-5-fluoro-6-((2-octyldodecyl)oxy)benzo[c][1,2,5]thiadiazole (0.49 g, 0.81 mmol) and tributyl(furan-2-yl)stannane (0.64 mL, 2.01 mmol) were dissolved in 30 mL dry toluene and stirred under argon atmosphere for 2 h. Then, bis(dibenzylidene-acetone)palladium (0) (40.0 mg, 40.0 µmol) and tri(o-tolyl)phosphine (0.05 g, 0.16 mmol) were added and the mixture was heated to 110 °C for 2 days under inert atmosphere. Through evaporation of the toluene under reduced pressure, the crude product was purified by column chromatography on silica gel using eluent 1:6 dichloromethane:hexane. The yield 70%. ^{1}H NMR (400 MHz, $CDCl_3$) δ 7.74 (d, J = 0.8 Hz, 1H), 7.69 (d, J = 0.8 Hz, 1H), 7.52 (d, J = 3.3 Hz, 1H), 7.42 (d, J = 3.3 Hz, 1H), 6.66 (m, 2H), 4.02 (d, J = 5.6 Hz, 2H), 1.92 – 1.81 (m, 2H), 1.26 (s, 70 H), 0.88 (s, 6H). ^{13}C NMR (100 MHz, $CDCl_3$) δ 155.6, 153.0, 149.4, 148.1, 148.0, 147.4, 147.2, 146.9, 146.9, 145.8, 145.8, 143.5, 143.4, 143.0, 114.4, 114.3, 114.2, 113.7, 113.7, 111.7, 111.5, 108.2, 108.1, 78.0, 39.1, 31.7, 30.9, 29.9, 29.5, 29.5, 29.4, 29.2, 28.1, 27.7, 26.7, 26.6, 22.5, 17.3, 17.1, 13.9, 13.4. HRMS (ESI, m/z), $[M+H]^+$: for $C_{34}H_{48}N_2O_3FS$, calculated 583.3370 found 583.3370.

2.4.14 Synthesis of 4,7-bis(5-bromothiophen-2-yl)-5-fluoro-6-((2-octyldodecyl) oxy)benzo[c][1,2,5]thiadiazole (14)

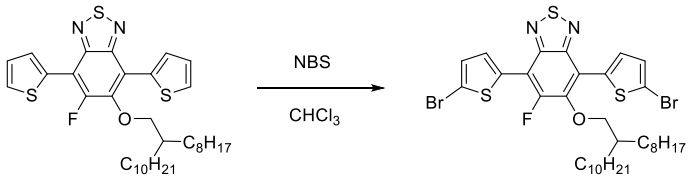

Figure 2.18: Synthetic pathway for 4,7-bis(5-bromothiophen-2-yl)-5-fluoro-6-((2-octyldodecyl)oxy)benzo[c][1,2,5]thiadiazole.

5-Fluoro-6-((2-octyldodecyl)oxy)-4,7-di(thiophen-2-yl)benzo[c][1,2,5]thiadiazole (0.11 g, 0.40 mmol) was dissolved in 25 mL chloroform, and N-bromosuccinimide (63.6 mg, 0.36 mmol) was added in one portion under dark atmosphere. After stirring at room temperature for 4 h, the chloroform was removed. The residue was extracted with dichloromethane. The combined organic parts were washed with pure water and dried over $MgSO_4$. After evaporation of the chloroform under reduced pressure, the crude product was purified by column chromatography on silica gel using eluent 1:3 dichloromethane: hexane. The yield was 90%. ^{1}H NMR (400 MHz, $CDCl_3$) δ 8.25 (d, J = 4.0 Hz, 1H), 7.96 (d, J = 3.8 Hz, 1H), 7.13 (dd, J_1=6.8, J_2 =3.8 Hz, 2H), 3.98 (d, J = 5.9 Hz, 2H), 2.10 – 1.90 (m, 1H), 1.54 (m, 4H), 1.29 (s, 28H), 0.89 (d, J = 4.6 Hz, 6H). ^{13}C NMR (100 MHz, $CDCl_3$) δ 155.7, 153.2, 149.3, 148.7, 148.6, 146.5, 146.3, 134.8, 133.6, 133.6, 131.1, 130.5, 130.4, 129.9, 129.5, 116.3, 116.2, 116.0, 110.6, 110.5, 77.9, 38.9, 31.8, 30.8, 29.9, 29.6, 29.6, 29.2, 26.6, 22.6, 14.0. HRMS (ESI, m/z), $[M+H]^+$: for $C_{34}H_{46}N_2OFS_3Br_2$ calculated 773.1103 found 773.1119.

2.4.15 Synthesis of 4,7-bis(5-bromothieno[3,2-b]thiophen-2-yl)-5-fluoro-6-((2-octyldodecyl)oxy)benzo[c][1,2,5]thiadiazole (15)

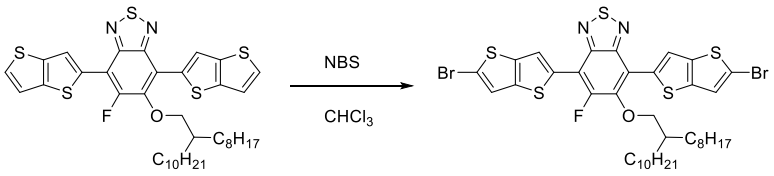

Figure 2.19: Synthetic pathway for 4,7-bis(5-bromothieno[3,2-b]thiophen-2-yl)-5-fluoro-6-((2-octyldodecyl)oxy)benzo[c][1,2,5]thiadiazole.

5-Fluoro-6-((2-octyldodecyl)oxy)-4,7-bis(thieno[3,2-b]thiophen-2-yl)benzo[c][1,2,5] thiadiazole (0.30 g, 0.41 mmol) was dissolved in 25 mL chloroform, and N-bromo-succinimide (0.15 g, 0.83 mmol) was added in one portion under dark atmosphere. After stirring at room temperature for 4 h, the chloroform was removed. The residue was extracted with dichloromethane. The combined organic parts were washed with pure water and dried over $MgSO_4$. After evaporation of the chloroform under reduced pressure, the crude solid was recrystallized in methanol, and the desired product is obtained. The yield was 88%. ^{1}H NMR (400 MHz, $CDCl_3$) δ 8.62 (s, 1H), 8.40 (s, 1H), 7.28 (s, 1H), 7.27 (s, 1H), 4.01 (d, J = 6.1 Hz, 2H), 2.06 – 1.99 (m, 1H), 1.61 – 1.48 (m, 4H), 1.28 (s, 28H), 0.89 (d, J = 5.2 Hz, 6H). ^{13}c NMR (101 MHz, $CDCl_3$) δ 155.9, 153.3, 149.6, 148.9, 148.7, 146.7, 146.5, 140.4, 140.3, 139.5, 139.3, 134.6, 134.6, 133.3, 133.3, 122.4, 121.9, 121.8, 117.0, 115.3, 115.0, 111.4, 111.3, 78.0, 38.9, 31.8, 30.8, 30.0, 29.6, 29.6, 29.6, 29.5, 29.3, 29.2, 26.6, 22.6, 14.0. HRMS (ESI, m/z), $[M+H]^+$: for $C_{38}H_{45}N_2OFS_5Br_2$ calculated 884.0466 found 884.0522.

2.4.16 Synthesis of 4,7-bis(5-bromo-4-hexylthiophen-2-yl)-5-fluoro-6-((2-octyldodecyl) oxy)benzo[c][1,2,5]thiadiazole (16)

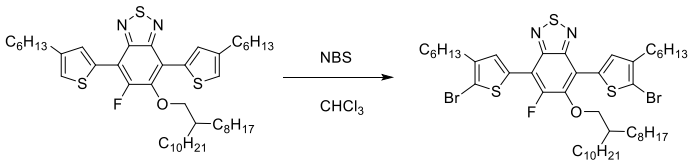

Figure 2.20: Synthetic pathway for 4,7-bis(5-bromo-4-hexylthiophen-2-yl)-5-fluoro-6-((2-octyldodecyl)oxy)benzo[c][1,2,5]thiadiazole.

5-Fluoro-6-((2-octyldodecyl)oxy)-4,7-bis(4-hexylthiophen-2-yl) benzo[c][1,2,5] thiadiazole (0.19 g, 0.24 mmol) was dissolved in 25 mL chloroform, and N-bromo-succinimide (87.3 mg, 0.49 mmol) was added in one portion under dark atmosphere. After stirring at room temperature for 4 h, the chloroform was removed. The residue was extracted with dichloromethane. The combined organic parts were washed with pure water and dried over $MgSO_4$. After evaporation of the chloroform under reduced pressure, the crude product was purified by column chromatography on silica gel using eluent 1:6 dichloromethane: hexane. The yield was 94%. ^{1}H NMR (400 MHz, $CDCl_3$) δ 8.23 (s, 1H), 7.92 (s, 1H), 4.00 (d, J = 5.9 Hz, 2H), 2.64 (t, J = 7.7 Hz, 4H), 2.00 (dd, J_1= 11.6, J_2= 5.7 Hz, 1H), 1.69 – 1.63 (m, 4H), 1.37 – 1.25 (m, 44H), 0.89 (m, 12H). ^{13}C NMR (100 MHz, $CDCl_3$) δ 155.8, 153.3, 149.5, 148.9, 148.8, 146.5, 146.4, 142.1, 141.7, 132.9, 131.7, 131.1, 131.0, 116.3, 113.3, 113.2, 113.1, 110.7, 110.5, 77.9, 38.9, 31.8, 31.5, 31.5, 30.8, 29.9, 29.7, 29.6, 29.5, 29.5, 29.4, 29.2, 28.9, 28.8, 26.6, 22.6, 14.0. HRMS (ESI, m/z), $[M+H]^+$: for $C_{46}H_{70}N_2OFS_3Br_2$ calculated 941.2981 found 941.2979.

2.4.17 Synthesis of 4,7-bis(5-bromoselenophen-2-yl)-5-fluoro-6-((2-octyldodecyl) oxy)benzo[c][1,2,5]thiadiazole (17)

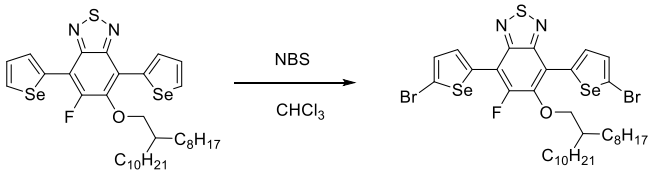

Figure 2.21: Synthetic pathway for 4,7-bis(5-bromoselenophen-2-yl)-5-fluoro-6-((2-octyldodecyl)oxy)benzo[c][1,2,5]thiadiazole.

5-Fluoro-6-((2-octyldodecyl)oxy)-4,7-di(selenophen-2-yl)benzo[c][1,2,5]thiadiazole (0.30 g, 0.42 mmol) was dissolved in 25 mL chloroform, and N-bromosuccinimide (0.15 g, 0.85 mmol) was added in one portion under dark atmosphere. After stirring at room temperature for 4 h, the chloroform was removed. The residue was extracted with dichloromethane. The combined organic parts were washed with pure water and dried over $MgSO_4$. After evaporation of the chloroform under reduced pressure, the crude product was purified by column chromatography on silica gel using eluent 1:4 dichloromethane: hexane. The yield was 95%. ^{1}H NMR (400 MHz, $CDCl_3$) δ 8.55 (d, J = 4.4 Hz, 1H), 8.06 (d, J = 4.4 Hz, 1H), 7.36 (t, J = 4.3 Hz, 2H), 4.02 (d, J = 6.3 Hz, 2H), 2.12 – 2.01 (m, 1H), 1.64 – 1.41 (m, 4H), 1.28 (d, J = 3.1 Hz, 28H), 0.89 (d, J = 4.6 Hz, 6H). ^{13}C NMR (100 MHz, $CDCl_3$) δ 155.6, 153.0, 149.0, 148.8, 146.3, 146.1, 139.1, 139.1, 138.4, 138.3, 133.2, 132.9, 132.9, 132.2, 132.0, 121.4, 121.3, 120.7, 118.0, 112.5, 112.4, 78.2, 78.2, 39.0, 31.8, 30.7, 29.9, 29.6, 29.5, 29.5, 29.2, 26.5, 22.5, 14.0, 0.9. HRMS (ESI, m/z), $[M+H]^+$: for $C_{34}H_{45}N_2OFSSe_2Br_2$ calculated 865.9934 found 866.0013.

2.4.18 Synthesis of P1

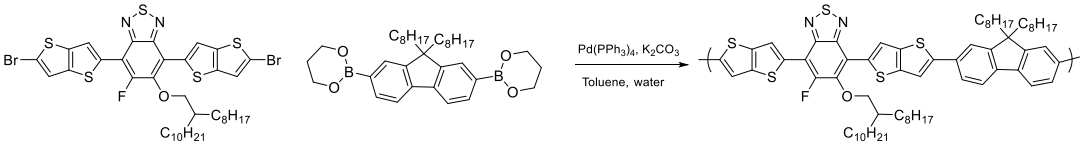

Figure 2.22: Synthetic pathway for P1.

4,7-Bis(5-bromothieno[3,2-b]thiophen-2-yl)-5-fluoro-6-((2-octyldodecyl)oxy)benzo[c][1,2,5] thiadiazole (0.10 g, 0.11 mmol), 9,9-Dioctylfluorene-2,7-diboronic acid bis(1,3-propanediol) ester (63.1 mg, 0.11 mmol), 0.14 mL 2 M K_2CO_3, 1–2 drops Aliquat 336, and $Pd(PPh_3)_4$ (5 mol%) were poured in a 50 mL schlenk tube, and stirred under argon atmosphere for 2 h. Then, 15 mL dry toluene was added and heated to reflux for 72 h. After removal of the toluene, the crude was extracted with chloroform and washed with pure water. The combined organic parts were dried over $MgSO_4$, and the solvent was evaporated under reduced pressure. Then, cold methanol and sodium diethyldithiocarbamate (Pd scavenger) were added to the crude and stirred for 1.5 h. The polymer was then filtered through a soxhlet extractor and washed with methanol, acetone,and to eliminate the low molecular weight oligomers. Chloroform was used to gather polymer as a dark purple colored solid. The yield was 47%. Mw: 79 900 Da, Mn: 55 552 Da, PDI: 1.43

2.4.19 Synthesis of P2

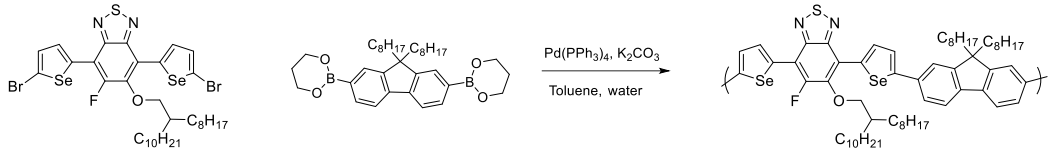

Figure 2.23: Synthetic pathway for P2.

4,7-Bis(5-bromoselenophen-2-yl)-5-fluoro-6-((2-octyldodecyl)oxy)benzo[c][1,2,5] thiadiazole (0.10 g, 0.12 mmol), 9,9-Dioctylfluorene-2,7-diboronic acid bis(1,3-propa-

nediol) ester (64.4 mg, 0.12 mmol), 0.13 mL 2 M K_2CO_3, 1–2 drops Aliquat 336, and $Pd(PPh_3)_4$ (5 mol%) were poured in a 50 mL schlenk tube, and stirred under argon atmosphere for 2 h. Then, 15 mL dry toluene was added and heated to reflux for 72 h. After removal of the toluene, the crude was extracted with chloroform and washed with pure water. The combined organic parts were dried over $MgSO_4$, and the solvent was evaporated under reduced pressure. Then, cold methanol and sodium diethyldithiocarbamate (Pd scavenger) were added to the crude and stirred for 1.5 h. The polymer was then filtered through a soxhlet extractor and washed with methanol, acetone to eliminate the low molecular weight oligomers. Hexane was used to gather polymer as a dark orange colored solid. The yield was 54%. Mw: 27 455 Da, Mn: 16 515 Da, PDI: 1.66

2.4.20 Synthesis of P3

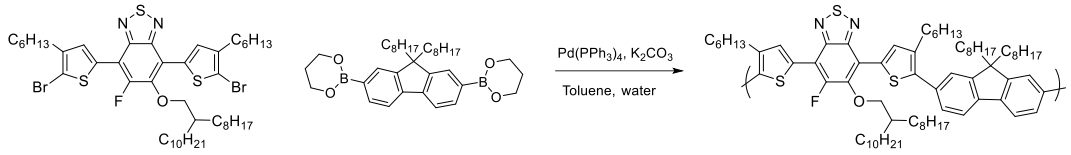

Figure 2.24: Synthetic pathway for P3.

4,7-Bis(5-bromo-4-hexylthiophen-2-yl)-5-fluoro-6-((2-octyldodecyl)oxy)benzo[c][1,2,5]thiadiazole (0.10 g, 0.11 mmol), 9,9-Dioctylfluorene-2,7-diboronic acid bis(1,3-propanediol) ester (59.3 mg, 0.11 mmol), 0.13 mL 2 M K_2CO_3, 1–2 drops Aliquat 336, and $Pd(PPh_3)_4$ (5 mol%) were poured in a 50 mL schlenk tube, and stirred under argon atmosphere for 2 h. Then, 15 mL dry toluene was added and heated to reflux for 72 h. After removal of the toluene, the crude was extracted with chloroform and washed with pure water. The combined organic parts were dried over $MgSO_4$, and the solvent was evaporated under reduced pressure. Then, cold methanol and sodium diethyldithiocarbamate (Pd scavenger) were added to the medium and stirred for 1.5 h. The polymer was then filtered through a soxhlet extractor and washed with methanol, acetone to eliminate the low molecular weight parts. Hexane was used to gather polymer as a dark orange colored solid. The yield was 16%. Mw: 4 821 Da, Mn: 3 369 Da, PDI: 1.43

2.4.21 Synthesis of P4

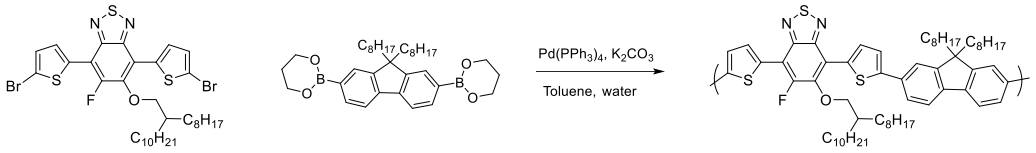

Figure 2.25: Synthetic pathway for P4.

4,7-Bis(5-bromothiophen-2-yl)-5-fluoro-6-((2-octyldodecyl)oxy)benzo[c][1,2,5] thiadiazole (0.10 g, 0.13 mmol), 9,9-Dioctylfluorene-2,7-diboronic acid bis(1,3-propanediol) ester (71.5 mg, 0.13 mmol), 0.19 mL 2 M K_2CO_3, 1–2 drops Aliquat 336, and $Pd(PPh_3)_4$ (5 mol%) were poured in a 50 mL schlenk tube, and stirred under argon atmosphere for 2 h. Then, 15 mL dry toluene was added and heated to reflux for 72 h. After removal of the toluene, the crude was extracted with chloroform and washed with pure water. The combined organic parts were dried over $MgSO_4$, and the solvent was evaporated under reduced pressure. Then, cold methanol and sodium diethyldithiocarbamate (Pd scavenger) were added to the crude and stirred for 1.5 h. The polymer was then filtered through a soxhlet extractor and washed with methanol, acetone to eliminate the low molecular weight oligomers. Hexane was used to gather polymer as a dark purple colored solid. The yield was 57%. Mw: 13 333 Da, Mn: 7 598 Da, PDI: 1.75

CHAPTER 3

RESULTS AND DISCUSSION

3.1 Electropolymerization and Electrochemical Characterizations of Homo-polymers

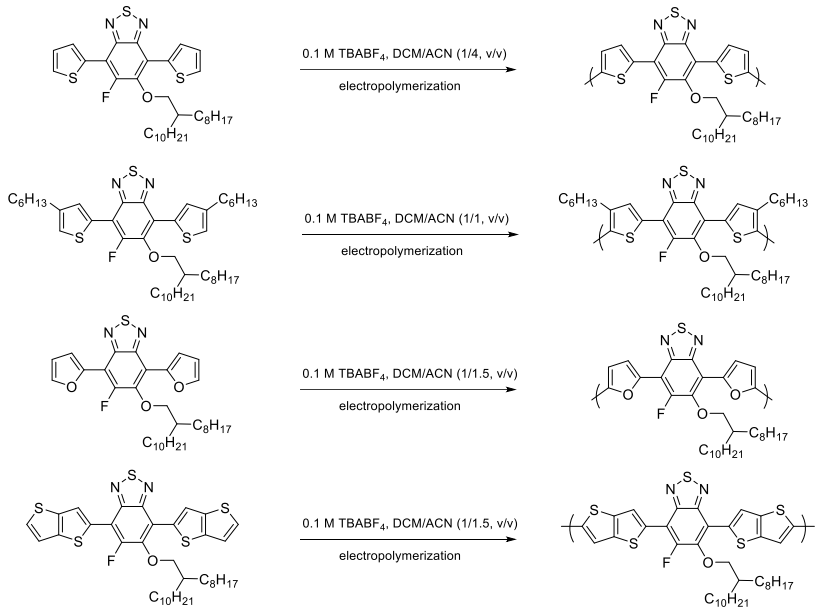

Figure 3.1: Electrochemical polymerization of (a) PTBTT (b) PHTBTHT (c) PFBTF and (d) PTTBTTT.

Certain simplicity, easy use and multifunctionality of cyclic voltammetry (CV) make it a versatile and widely preferred technique for both electropolymerization and electrochemical characterization of the compounds. Due to above-mentioned advantages all electrochemical polymerizations were performed with CV between 0.0 V and 1.4 in 0.1 M acetonitrile (ACN)/ dichloromethane (DCM) (4/1, v/v) for PTBTT (1/1, v/v) for PHTBTHT and (1.5/1, v/v) for PFBTF and PTTBTTT solution containing tetra-

butylammonium tetrafluoroborate ($TBABF_4$) as the supporting electrolyte. During electropolymerization, different solvent mixtures were used in order to improve the solubility and obtain good polymer film formation on ITO electrodes (Figure 3.1). The CVs for electropolymerizations were depicted below (Figure 3.2).

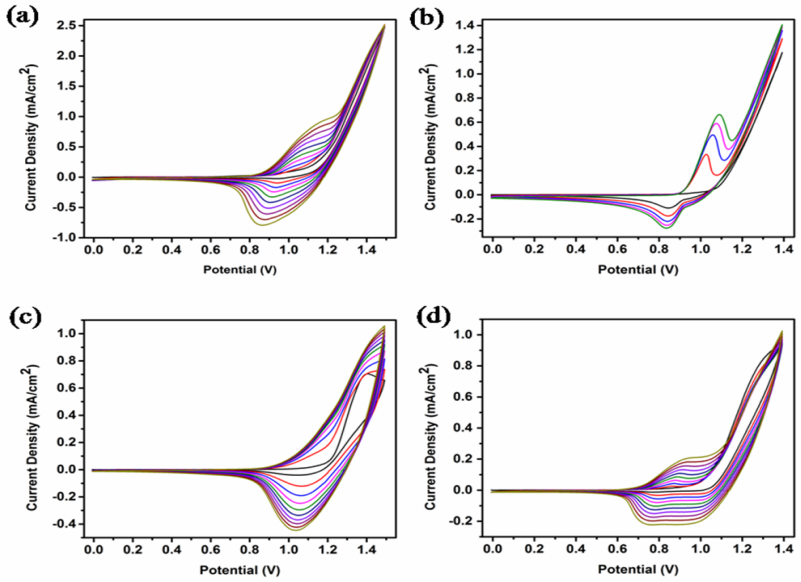

Figure 3.2: Electrochemical deposition of (a) PTBTT (b) PHTBTHT (c) PFBTF and (d) PTTBTTT on ITO coated glass slides in 0.1 M $TBABF_4$/DCM/ACN solution at a scan rate of 100 mV $\cdot$ s^{-1}.

After electrochemical synthesis, the redox behaviors of PTBTT, PHTBTHT, PFBTF and PTTBTTT were also investigated via CV in a conventional three electrode system (Ag wire as the reference electrode (RE), a Pt wire as the counter electrode (CE), and indium tin oxide (ITO)-coated glass slide as the working electrode (WE)) immersed in 0.1 M tetrabutylammonium hexafluorophosphate ($TBAPF_6$)/acetonitrile (ACN) electrolyte/solvent couple at a scan rate of 100 mV $\cdot$ s^{-1}. In addition, some crucial parameters such as oxidation/reduction potentials, HOMO/LUMO energy levels and electronic band gap (E_g^{el}) which are vital for several of applications could be calculated from CV.

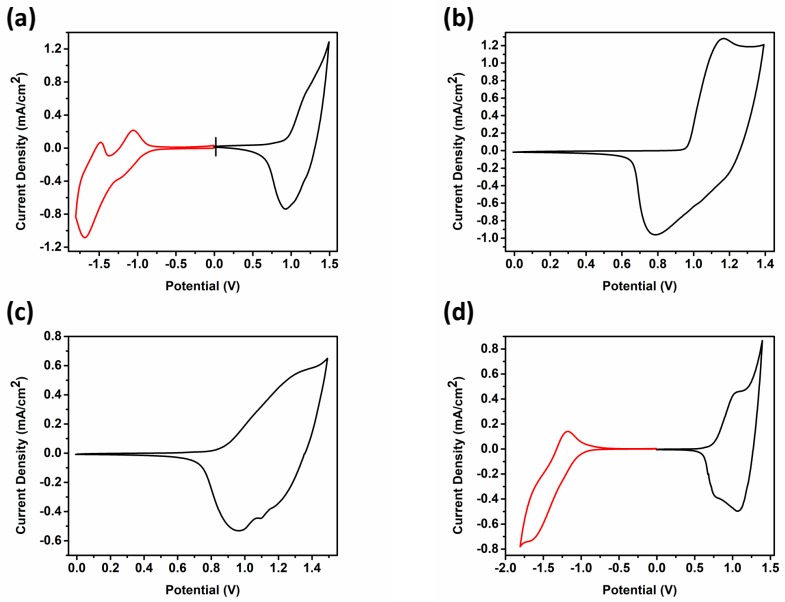

Figure 3.3: Single scan cyclic voltammograms of (a) PTBTT (b) PHTBTHT (c) PFBTF and (d) PTTBTTT in a monomer free 0.1 M $TBAPF_6$ /ACN solution.

The single scan cyclic voltammograms (CVs) were obtained for polymers PTBTT, PHTBTHT, PFBTF and PTTBTTT (Figure 3.3). As seen from the CVs, thiophene and thienothiophene comprising polymers PTBTT and PTTBTTT exhibited ambipolar character (p-type and n-type doping behavior) with 1.17 V/ -1.68 V and 1.03 V/ -1.65 V oxidation and reduction potentials. However, 3-hexylthiophene and furan bearing polymers PHTBTHT and PFBTF showed only p-type doping behavior with 1.16 V and 1.33 V oxidation potentials.

When PTBTT, PHTBTHT, PFBTF and PTTBTTT were compared in terms of their electrochemical behaviors (Table 3.1), tthienothiophene comprising derivative PTTBTTT exhibited the lowest oxidation potential as 1.03 V which can be dedicated to the different electron densities of four donor groups (thiophene, 3-hexylthiophene, furan and thienothiophene), in other words, PTTBTTT has higher electron density with extended conjugation which results lower oxidation potential [59]. PTBTT and PHTBTHT show oxidation potentials as 1.17 V and 1.16 V, respectively. This small difference could arise from the alkyl chain of the hexylthiophene. Since alkyl chain inductively donates electron to the ring and increase the electron density resulting in lower oxidation potential.

HOMO/LUMO energy levels are also crucial parameters for polymers especially to determine their application fields and can be calculated from CVs. Herein, HOMO/ LUMO energy levels of all polymers (PTBTT, PHTBTHT, PFBTF and PTTBTTT) were calculated from the onsets of the corresponding oxidation potentials and reported as -5.68 eV/ -3.91 eV for PTBTT, -5.71eV / -3.72 eV for PHTBTHT, -5.61 eV/ -4.04 eV for PFBTF and -5.51 eV / -3.71 eV for PTTBTTT.

Table 3.1: Electrochemical and Spectroelectrochemical properties of polymers.

	PTBTT	PHTBTHT	PFBTF	PTTBTTT
$E^{ox}{}_{mon}$	1.40	-	1.40	1.30
$E_{p\text{-doping}}$	1.17	1.16	1.33	1.03
$E_{p\text{-dedoping}}$	0.93	0.78	0.96	0.76
$E_{n\text{-doping}}$	-1.20 /-1.68	-	-	-1.65
$E_{n\text{-dedoping}}$	-1.05 /-1.47	-	-	-1.18
HOMO (eV)	-5.68	-5.71	-5.61	-5.51
LUMO (eV)	-3.91	-3.72	-4.04	-3.51
Λ_{max} (nm)	549	511	592 / 652	536
$E_g{}^{op}$	1.65	1.99	1.54	1.64
Polaron (nm)	805	840	875	770

The scan rate dependencies of the polymers (PTBTT, PFBTF and PTTBTTT) were studied by recording the single scan CVs at four different scan rates (50 mV $\cdot$ s^{-1}, 100 mV $\cdot$ s^{-1}, 150 mV $\cdot$ s^{-1}) in a monomer free 0.1 M $TBAPF_6$ /ACN electrolyte solution. Current density - applied potential (Figure 3.4) and current density - scan rate graphs (Figure 3.5) were reported. As seen, a linear relationship between the current density and scan rate demonstrates the non-diffusion controlled mass transfer during doping–dedoping processes and formation of well adhered polymer films.

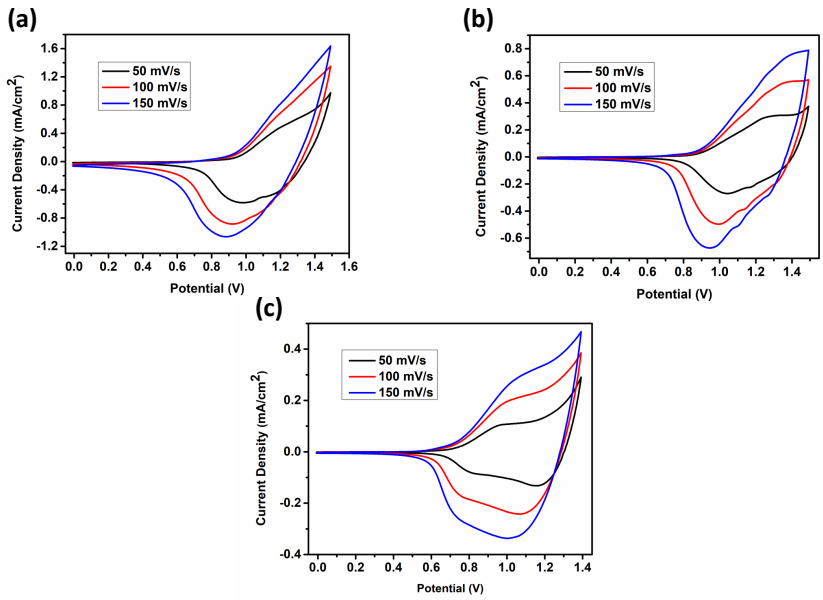

Figure 3.4: Scan rate dependence of (a) PTBTT (b) PFBTF and (c) PTTBTTT in 0.1 M $TBAPF_6$ /ACN solution.

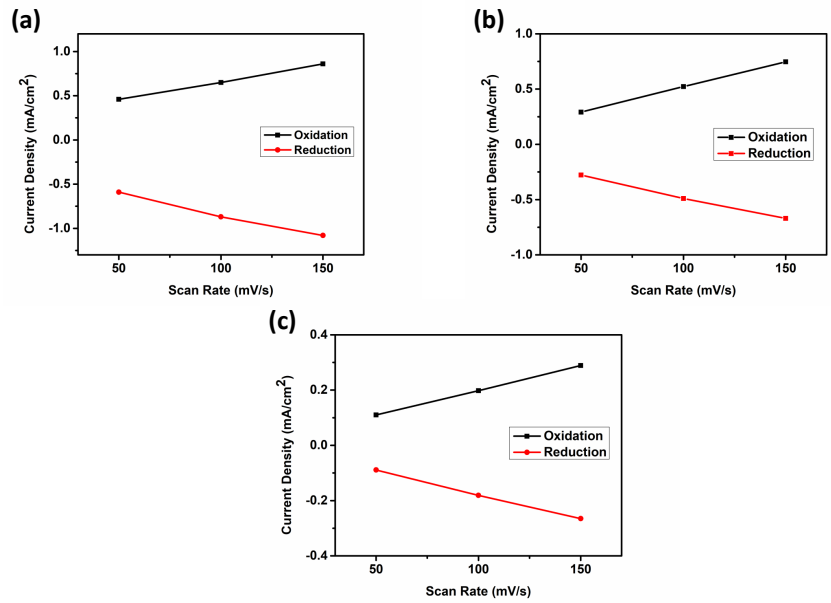

Figure 3.5: Current density - scan rate graphs of (a) PTBTT (b) PFBTF and (c) PTTBTTT in 0.1 M $TBAPF_6$ /ACN solution.

3.1.1 Spectroelectrochemical Studies

After electrochemical characterizations, the UV-Vis-NIR absorption spectra of the polymers were recorded in order to investigate the optical and electronic changes upon stepwise oxidation. Some crucial parameters like neutral state absorption maxima (λ_{max}), optical band gap (E_g^{op}) and polaronic region were calculated from UV-Vis-NIR absorption spectra. Polymers were obtained electrochemically on ITO working electrode surface via CV as described before and spectroelectrochemical studies were performed in 0.1 M $TBAPF_6$/ACN solution using UV-Vis-NIR spectrophotometer integrated with potentiostat. Initially, –0.5 V constant potential was applied in order to record the true neutral film absorptions and then potential was sweeped between 0.0 V and 1.5 V for PTBTT, 0.0 V and 1.4 V for PHTBTHT, 0.0 V and 1.3 V for PFBTF and 0.0 and 1.4 V for PTTBTTT.

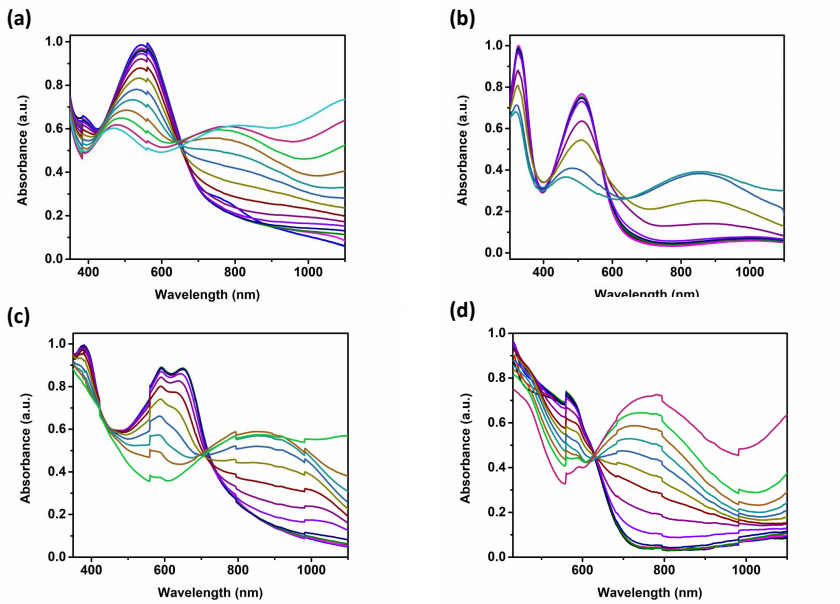

Figure 3.6: Electronic absorption spectra of all polymers in 0.1 M $TBAPF_6$/ACN solution between 0.0 V and 1.5 V for PTBTT, 0.0 V and 1.4 V for PHTBTHT, 0.0 V and 1.3 V for PFBTF and 0.0 and 1.4 V for PTTBTTT.

As seen above (Figure 3.6), the neutral state absorption maxima revealed at 549 nm for PTBTT, 511 nm for PHTBTHT, 592 nm for PFBTF and 536 nm for PTTBTTT which can be assigned to π- π* transitions. Upon stepwise oxidation while the neutral

state absorptions depleted, new absorption bands which correspond to the formation of radical cations (polaron bands) appeared at 805 nm for PTBTT, 840 nm for PHTBTHT, 875 nm for PFBTF and 770 nm for PTTBTTT, respectively. Another crucial parameter for conducting polymers which affect their applicability in different fields like electrochromic devices, solar cells is the band gap which can be calculated from the onset of the π- π* transition of the neutral polymers films according to the equation $E_g^{op} = 1241/\lambda$, were calculated as 1.65 eV (PTBTT), 1.99 eV (PHTBTHT), 1.57 eV (PFBTF) and 1.64 eV (PTTBTTT).All electrochemical and spectroelectrochemical analyses for all polymers (PTBTT, PHTBTHT, PFBTF and PTTBTTT) were summarized in (Table 3.1).

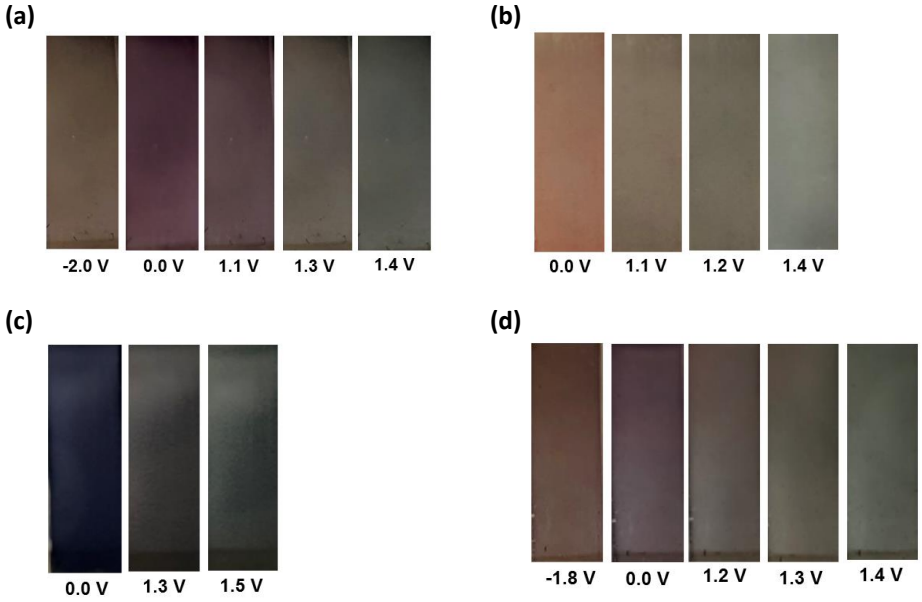

Figure 3.7: Colors of (a) PTBTT (b) PHTBTHT (c) PFBTF and (d) PTTBTTT at neutral and oxidized/reduced states with different intermediate colors.

When spectroelectrochemical results were compared for all polymers (PTBTT, PHTBTHT, PFBTF and PTTBTTT) to get deep insight on the electron donor ability of thiopehene, 3-hexylthiophene, furan and thienothiophene. As seen in Table 1 furan comprising PFBTF exhibited most red shifted neutral state absorption centered at 592/652 nm with lowest optical band gap calculated as 1.57 eV which can be dedicated to the better electron donor ability of furan unit as a π-bridge [60]. Even though PFBTF has the lowest E_g^{op}, a similar trend is not observed in E_g^{el}. This difference

can be emerged from the formation of the charge on polymer film during the cyclic voltammetry run. Therefore, high E_g^{el} is resulted [61].PTBTT and PTTBTTT have similar E_g^{op} values as 1.65 eV and 1.64 eV, respectively. Even though thiophene and thienothiophene have high electron densities and strong donating abilities, furan is more electronegative than its sulfur counterpart, so furan based polymers could reveal better properties. The highest E_g^{op} value belongs to PHTBTHT due to the bulky alkyl chain of the 3-hexylthiophene, which causes steric hindrance and interrupts coplanarity between aromatic rings on the polymer backbone. Therefore, distortion of the planarity results in higher E_g^{op} [62].

As a further characterization, electrochromic properties of the resulting polymers were also investigated and all polymers exhibited a multichromic behavior which is important for variety of applications such as electrochromic devices, displays, mirrors, windows and sun-glasses. Colors of all polymer films were recorded at different applied potentials and depicted (Figure 3.7). As seen, the electrochromic properties and colors of the polymers in the neutral state are consistent with the neutral state absorption values. While the furan comprising polymer PFBTF with red shifted absorption (592 / 652 nm) exhibited bright blue color in the neutral state, the bluest shifted (511 nm) polymer PHTBTHT exhibited orange color in the neutral state. In addition, PTBTT and PTTBTTT showed the different tones of red-purple in the neutral state with 549 nm and 536 nm absorption maxima. Furthermore, all polymers exhibited multi-electrochromic character and showed different tones of grayish green color in the oxidized states.

3.1.2 Kinetic Studies

Kinetic studies were performed in order to explore and calculate the optical contrast (the changes in percent transmittance) and switching time (the time required for coloring/bleaching process between two extreme states) values while continuous stepping the potential between two extreme states (neutral and oxidized states) within 5 s time interval. The wavelengths used for the electrochromic switching studies were determined from the spectroelectrochemical studies as the maximum absorption wavelengths and reported (Table 3.2). The percent transmittance-time graphs

were displayed for PTBTT, PHTBTHT (Figure 3.8), PFBTF and PTTBTTT (Figure 3.9) and corresponding electrochromic switching properties were summarized (Table 3.2).

Table 3.2: Kinetic properties of the polymers.

	Λ_{max} (nm)	Optical Contrast (%)	Switching Time (s)
PTBTT	563	24	2.8
	805	24	2.1
PHTBTHT	512	37	2.1
	840	28	2.1
PFBTF	590	23	1.9
	915	11	1.8
PTTBTTT	570	26	2.3
	770	40	3.0

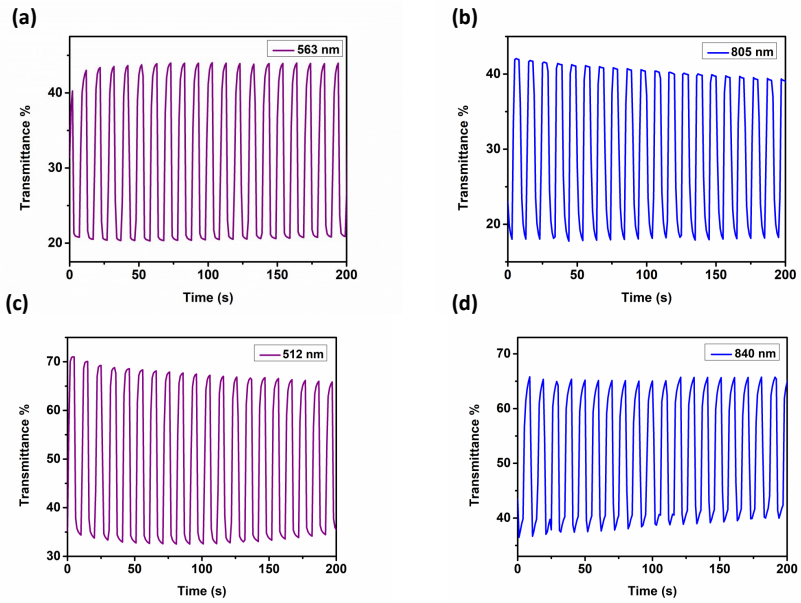

Figure 3.8: Electrochromic percent transmittance changes observed at the absorption maxima of (a,b) PTBTT and (c,d) PHTBTHT in 0.1 M $TBAPF_6$/ACN solution.

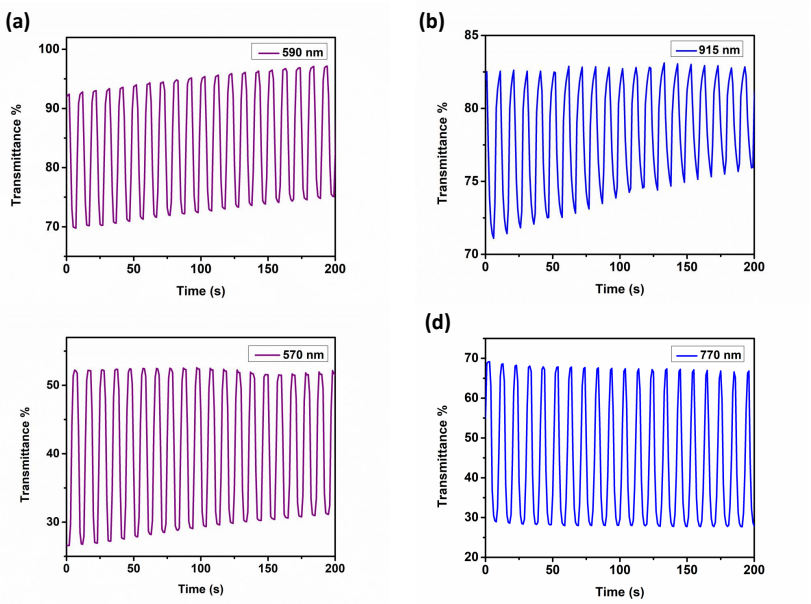

Figure 3.9: Electrochromic percent transmittance changes observed at the absorption maxima of (a,b) PFBTF and (c,d) PTTBTTT in 0.1 M $TBAPF_6$/ACN solution.

As seen, the optical contrast values were measured as 24% (at 563nm) and 24% (at 805 nm) for PTBTT and 37% (at 512 nm) and 28% (at 840 nm) for PHTBTHT (Figure 3.8). Then, the optical contrast values were measured as 23% (at 590 nm) and 11% (at 915 nm) for PFBTF and 26% (at 570 nm) and 40% (at 770 nm) for PTTBTTT (Figure 3.9). As illustrated (Table 3.2), 3-Hexylthiophene comprising polymer PHTBTHT exhibited the highest optical contrast as 37% in the visible region (at 512 nm). Finally, another important parameter namely switching time was calculated from kinetic studies as 2.8 s and 2.1 s for PTBTT, 2.1 s and 2.1 s for PHTBTHT, 1.9 s and 1.8 s for PFBTF, 2.3 s and 3.0 s for PTTBTTT at the corresponding wavelengths.

3.1.3 Computational Studies

HOMO, LUMO and ESP surfaces for the optimized geometries of tetramers of PTBTT, PHTBTHT, PFBTF and PTTBTTT are reported (Figure 3.10). HOMO orbitals were delocalized along the chain for tetramers instead for localizing on the donor acceptor. LUMO orbitals were also delocalized however less than HOMO, where they are mostly placed on the acceptor units as expected, especially on the central benzoth-

iadiazole units. Relatively more disordered distribution of frontier orbitals was observed for PHTBTHT due to the higher nonplanarity compared to other copolymers. ESP surface shows well-ordered and sequential distribution of electron rich (red) donor and electron deficient (blue) acceptor sites. Significant effect of alkoxy and -F substitutions were observed on the electrostatic potential distribution of 5-fluoro-6-((2-octyldodecyl)oxy)benzo[c][1,2,5]thiadiazole acceptor unit where benzothiadiazole unit became more electron deficient, leading to the better acceptor properties due to these substitutions. Reduced regularity and reduced repeating patterns were observed for ESP of PHTBTHT due to its decreased planarity and electron conjugation. Torsional angles between donor and acceptor units are given in (Table 3.3). There are two types of angles due to the different substitutions on two carbon atoms at the two sides of benzothiadiazole unit. -F substitution did not disturb planarity and all the angles are below 1°.

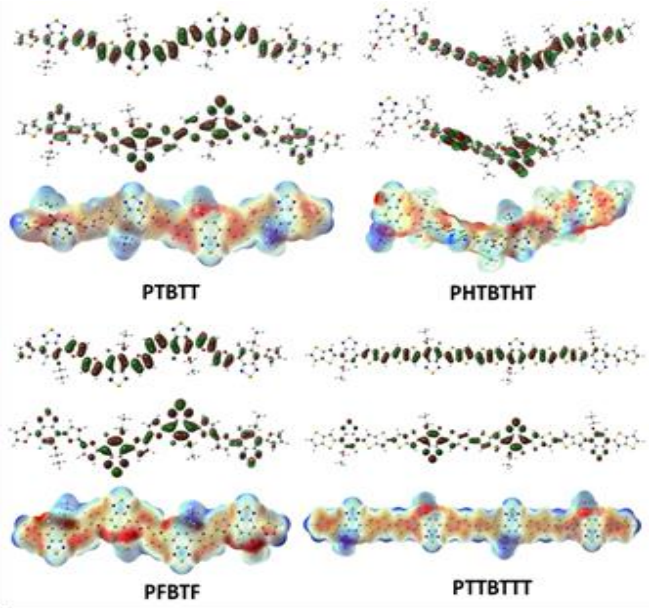

Figure 3.10: Molecular orbital surfaces of HOMO (top), LUMO (middle) and ESP mapping (bottom) for PTBTT, PHTBTHT, PFBTF and PTTBTTT.

However, alkoxy substitution significantly change planarity and torsional angles are between 9-15°. Still the main reason for the difference in the planarity of the chains is the torsional angle between two connected donor units. The torsional angles between two donors of PHTBTHT is 68.3° which significantly reduce electronic and optical

properties. The highest planarity was observed for PFBTF. Close values were determined three copolymers other than PHTBTHT, for the VIP, AIP and λreorg value which is directly related with the charge mobility. Similarly, PTBTT, PFBTF and PTTBTTT show close optical and direct band gap values, with the exception of non-planar PHTBTHT. The difference observed for experimental and computational band gap values are due to the interchain interactions that are not included in the theoretical calculations. Higher planarity of the PFBTF chains that leads to the better interchain packing resulted in the lower band compared to the single chain calculations and the most red-shifted neutral state absorption in the experiments. Finally, atomic charges by ESP fitting on the two donor and two acceptors in the middle of tetramers were calculated by neglecting end group donor-acceptor units to avoid end group effect. Although all copolymers have electron transfer from donor to acceptor according to these atomic charges, charge difference formed between donor and acceptor units are significantly higher in PFBTF which leads to the enhanced donor-acceptor capacity.

Table 3.3: Electronic and structural properties of PTBTT, PHTBTHT, PFBTF and PTTBTTT by DFT method.

	PTBTT	PHTBTHT	PFBTF	PTTBTTT
θ D-A	10.7 / 0.2	11.9 / 0.7	14.8 / 0.9	9.6 / 0.5
θ D-D	17.2	68.3	0.2	19.3
VIP	5.73	6.04	5.64	5.60
AIP	5.62	5.82	5.56	5.52
Λ_{reorg}	0.11	0.21	0.08	0.08
HOMO	-5.07	-5.37	-4.94	-5.05
LUMO	-3.06	-2.85	-2.99	-3.13
E_g^{el}	2.00	2.52	1.96	1.92
E_g^{op}	1.68	2.13	1.63	1.61
Charge Acceptor	-0.39	-0.36	-0.97	-0.14
Charge Donor	0.21	0.16	0.49	0.07

3.2 Electrochemical Characterizations of P1, P2, P3, and P4

Cyclic Voltammetry is a crucial tool for exploring oxidation-reduction behavior and HOMO/LUMO energy levels of the conjugated copolymers. These electrochemical behaviors are determined using a three-electrode cell system, and the electrodes are namely platinum wire as a counter, silver wire as a reference, and ITO coated glass slide as a working electrode.

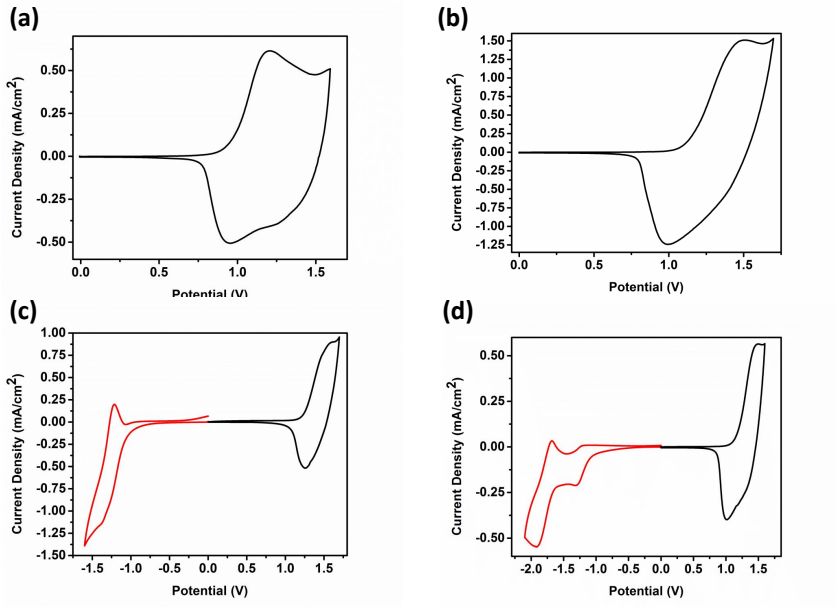

Figure 3.11: Single scan cyclic voltammetry of the polymers (a) P1, (b) P2, (c) P3, and (d) P4 in a 0.1 $TBAPF_6$ /ACN electrolyte solution.

In order to carry out cyclic voltammetry studies, polymers P1, P2, P3, and P4 were dissolved in chloroform to adjust a concentration of 5 mg/mL, and then spray coated onto the working electrode surface via a spray gun. Electrochemical studies were performed in a 0.1 M $TBAPF_6$/ACN supporting electrolyte/solvent combination at a 100 $mV \cdot s^{-1}$ scan rate. The single scan cyclic voltammetry of the polymers were run in the potential range between 0.00 V/ 1.60 V for P1, 0.00 V/ 1.65 V for P2, -1.60 V/ 1.70 V for P3, and -2.10 V/1.60 V for P4, respectively (Figure 3.11). The polymers' redox potentials at doping /doped state were determined as 1.20 V/ 0.95 V for P1, and 1.50 V/ 1.12 V for P2, 1.60 V/ 1.25 V for P3, and 1.45 V/ 1.00 V for P4 (Table 3.4). The polymers P3 and P4 showed ambipolar character (both p-type and n-

dope behavior). Even P4 shows reversible two n-doped states. N-doping/n-dedoping potentials were -1.36 V/ -1.21 V for P3, and -1.29V/ -1.21 V, and -1.91 V/ -1.68 V for P4, respectively.

In this work, different bridging units thieno[3,2-b]thiophene, selenophene, 3-hexylthiophene, and thiophene) were incorporated into the polymer backbone in order to compare the electrochemical behavior of the polymers. The different oxidation potentials of the polymers can be explained by electronic nature and different electron densities of the bridging units. The thieno[3,2-b]thiophene comprising polymer (P1) exhibited the lowest oxidation potential as 1.20 V among the other polymers. This is because of thieno[3,2-b]thiophene's high electron density nature and high electron-donating ability compared to other bridging units. The highest oxidation potential belongs to P3 as 1.60 V. In literature, it is stated that the 3-hexylthiophene comprising polymers exhibit higher oxidation potential values compared to others [63]. Besides, the bulky alkyl chain of 3-hexylthiophene sterically hinders the coplanarity between adjacent rings resulting in high oxidation potential. HOMO/LUMO energy levels characterization plays a crucial role in investigating the conjugated polymers' application fields. HOMO energy levels of the polymers, P1, P2, P3, and P4, were calculated from the onset of oxidation potentials using equation HOMO= -(4.75 + E_{ox}^{onset}) and recorded as -5.70 eV, -5.87 eV, -5.90 eV, and -5.89 eV, respectively. LUMO energy levels of the polymers were calculated from the onset of reduction potentials using equation LUMO= -(4.75 +E_{red}^{onset}) and recorded as -3.80 eV, -4.00 eV, -3.80 eV, and -3.71 eV, respectively. Electronic band gap (E_g^{el}) was calculated applying equation E_g^{el} = HOMO-LUMO and the lowest HOMO energy level belongs to the P1 among the other polymers. Since thieno[3,2-b]thiophene has higher electron density with an extended conjugation and higher electron-donating ability compared to selenophene, thiophene, and 3-hexylthiophene. P2, which comprising the selenophene unit, has the second-lowest HOMO energy level. It can be explained by selenium's high polarizability compared to its sulfur counterpart, which favors quinoid structure more and lowers HOMO energy level. Therefore, selenophene comprising polymer, namely P2, has a lower HOMO energy level than thiophene comprising polymer, namely P4. 3-hexylthiophene comprising polymer, namely P3, has the highest HOMO energy level due to above-mentioned reason.

Table 3.4: Electrochemical and Spectroelectrochemical properties of polymers.

	P1	P2	P3	P4
$E_{p\text{-doping}}$	1.20	1.50	1.60	1.45
$E_{p\text{-dedoping}}$	0.95	1.12	1.25	1.00
$E_{n\text{-doping}}$	- /-	-	-1.36	-1.29 / -1.91
$E_{n\text{-dedoping}}$	- /-	-	-1.21	-1.22 / -1.68
HOMO (eV)	-5.70	-5.87	-5.90	-5.89
LUMO (eV)	-3.80	-4.00	-3.80	-3.71
E_g^{op}	1.85	1.81	1.95	1.73
Λ_{max} (nm)	545	543	500	555
Polaron (nm)	770	845	740	785
Bipolaron (nm)	1530	1635	1570	1630

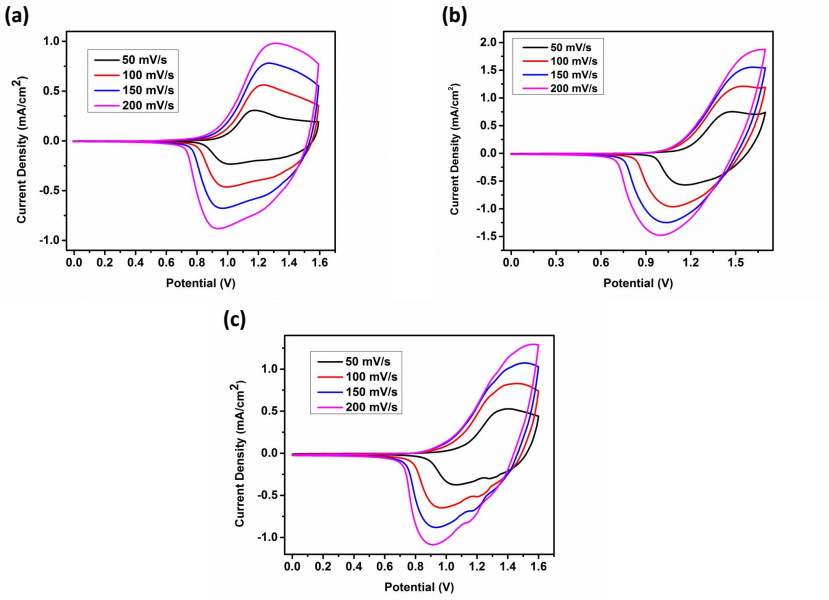

Figure 3.12: Scan rate dependences of the polymers (a) P1, (b) P2, and (c) P4 in a 0.1 M $TBAPF_6$ /ACN electrolyte solution.

The scan rate dependences of the polymers were investigated at a single scan cyclic voltammogram were reported at four scan rates (50 $mV \cdot s^{-1}$, 100 $mV \cdot s^{-1}$, 150 $mV \cdot s^{-1}$, 200 $mV \cdot s^{-1}$) in 0.1 M $TBAPF_6$ /ACN electrolyte solvent couple (Figure

3.12). The linear relationship of current density to the scan rate was investigated for P1, P2, and P4 (Figure 3.13). The linear plot proves the and non-diffusion-controlled mass transfer while doping-dedoping process and well-coated polymer film.

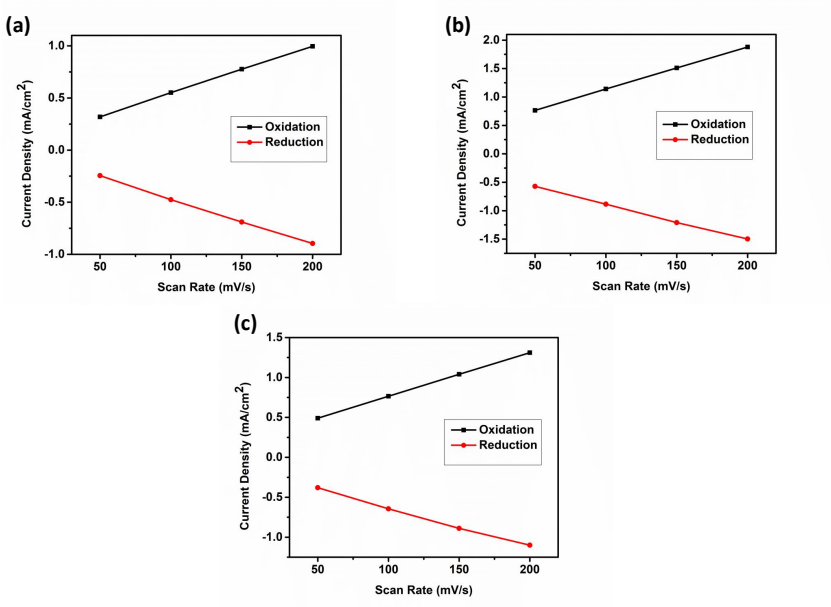

Figure 3.13: Current density – scan rate relationship of the polymers (a) P1, (b) P2, (c) P3, and (d) P4 in a 0.1 $TBAPF_6$ /ACN electrolyte solution.

3.2.1 Spectroelectrochemical Studies

Spectroelectrochemical works were conducted in order to discover optical properties and electronic changes in the application of stepwise oxidation. The characteristic parameters such as λ_{max}, optical band gap (E_g^{op}), polaron and bipolaron regions were determined from UV-Vis-NIR absorption spectra of the polymers. Absorption spectra of the spray-coated polymers onto ITO slides were carried out in a monomer free, 0.1 M $TBAPF_6$/ACN electrolyte solution using UV-Vis-NIR spectrophotometer coupled with a potentiostat. Spectroelectrochemical characterizations were started by applying -0.5 V constant potential to obtain neutral polymer film, then stepwise oxidation performed between 0.00 V and 1.40 V for P1, 0.00 V and 1.50 V for P2, 0.00 V and 1.60 V for P3, 0.00 V and 1.45 V for P4 (Figure 3.14). The maximum neutral state absorption of the polymers in the visible region of the spectrum were determined at 545 nm for P1, 543 nm for P2, 500 nm for P3, 555 nm for P4. These λ_{max} values

were attributed to π- π* transitions. The continuous stepwise oxidation leads to new absorptions which belongs to polaron (radical cation) and bipolaron (dication) formation in the NIR region. These new absorptions bands determined at 770 nm, 1530 nm for P1, 845 nm, 1635 nm for P2, 740 nm, 1570 nm for P3, 785 nm, 1630 nm for P4, respectively.

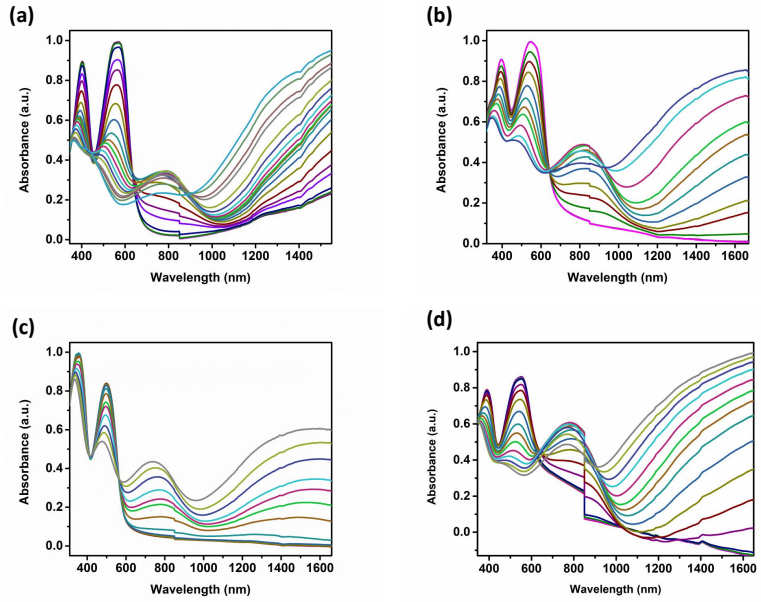

Figure 3.14: Electronic absorption spectra of the polymers (a) P1, (b) P2, (c) P3, and (d) P4 in a 0.1 M $TBAPF_6$ /ACN electrolyte solution.

Apart from the λ_{max}, polaron, and bipolaron characteristics, E_g^{op} is another important characteristic parameter to determine the application area of the conjugated polymers. The optical band gap is calculated from the onset of π- π* transitions of the polymer film's neutral state using the equation $E_g^{op} = 1241/\lambda$. The calculated E_g^{op} values are 1.85 eV for P1, 1.81 eV for P2, 1.95 eV for P3, and 1.73 eV for P4 respectively (Table 1). When the polymers' optical and electronic band gap were compared, E_g^{op} values were lower than E_g^{el} values. This difference can emerge from the charge on the polymer film during the run of cyclic voltammetry. Among four polymers, thiophene comprising polymer showed the red-shifted state absorption at 555 nm with the lowest E_g^{op} value as 1.73 eV. This result can be devoted to thiophenes' low-lying HOMO energy level compared to its selenium counterpart. Selenophene and thieno[3,2-b]thiophene comprising polymers showed similar E_g^{op} values as 1.81 eV

and 1.85 eV at similar neutral absorption states as 543 nm and 545 nm. These similar results can be dedicated to the high electron-donating ability of both selenophene and thieno[3,2-b]thiophene. 3-hexylthiophene comprising polymer has the highest E_g^{op} value as 1.95 eV, which can be devoted to the polymer's low molecular weight. This is probably due to containing sterically bulky alkyl chain in 3-hexylthiophene which interrupts polymerization resulting polymer with low chain length. As the number of repeating units decreases, conjugation length decreases, and hence a higher band gap of the P3 is resulted. As the number of repeating units decreases, conjugation length decreases, and a higher band gap of the P3 was calculated.

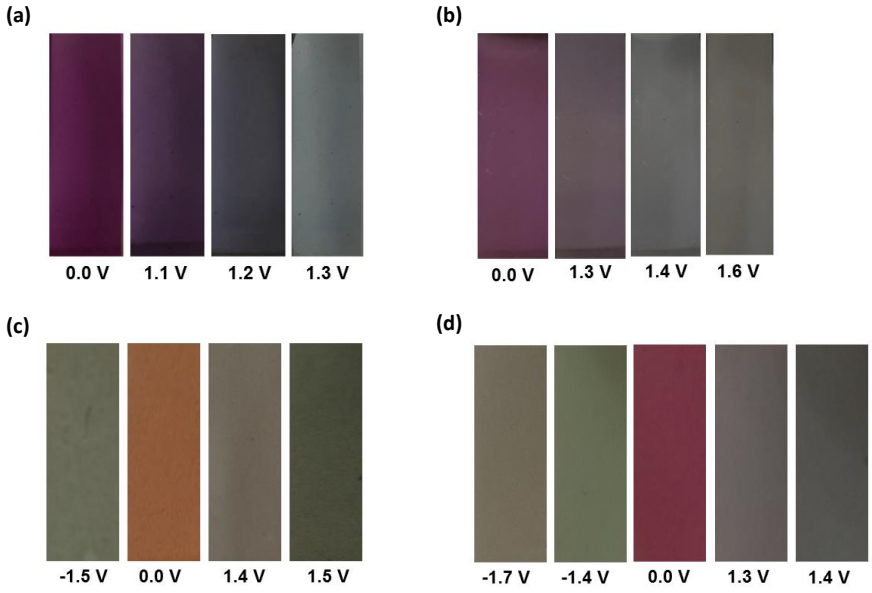

Figure 3.15: Different colors of the polymers (a) P1, (b) P2, (c) P3, and (d) P4 at neutral, oxidized, and reduced states.

All the polymers exhibited electrochromic character since they have different colors at both neutral and doped states. The electrochromic character is an important feature for conjugated polymers due to large application areas such as displays, smart windows, and glasses. The colors at neutral and doped states were reported in the application of a different constant potential (Figure 3.15). The color of the polymers at neutral states were in coherence with the color of neutral state absorptions. The thiophene comprising polymer showed the most red-shifted absorption (555 nm) with a purple color in the neutral state. The 3-hexylthiophene comprising polymer showed

most blue-shifted absorption (500 nm) with orange color in the neutral state. Moreover, P1 and P2 exhibited different purple color shades in their neutral states at 545 nm and 543 nm, respectively. All polymers showed different grey color shades in their oxidized states, whereas P3 and P4 showed different green color shades in their reduced states.

3.2.2 Kinetic Studies

In order to calculate the switching time and optical contrast of the polymers, kinetic works were conducted. Optical contrast can be defined as the change in the percent transmittance at a certain wavelength, and switching time is time needed to change color between neutral and oxidized states. Kinetic works were carried out at absorption maxima values determined in spectroelectrochemical works in the application of potential within 5s intervals. For all polymers optical contrast and switching times were reported at maximum absorption state of neutral, polaron and bipolaron regions (Figure 3.16) .

Table 3.5: Kinetic properties of the polymers.

	Λ_{max} (nm)	Optical Contrast (%)	Switching Time (s)
P1	545	50	3.4
	770	45	1.7
	1530	71	1.7
P2	543	39	3.1
	845	54	2.7
	1635	65	2.4
P3	500	19	1.5
	740	45	3.8
	1570	63	1.8
P4	555	34	2.8
	785	39	3.4
	1630	61	3.8

The reported values are 34% (at 403 nm) with 1.8 s, 50% (at 545 nm) with 3.4 s, 45% (at 770 nm) with 1.7 s, and 71% (at 1530 nm) with 1.7 s for P1, 29% (at 395 nm) with 2.9 s, 39% (at 543 nm) with 3.1 s, 54% (at 845 nm) with 2.7 s, and 65% (at 1635 nm) with 2.4 s for P2, 19% (at 360 nm) with 1.6 s, 19% (at 500 nm) with 1.5 s, 45% (at 740 nm) with 3.8 s, and 63% (at 1570 nm) with 1.8 s for P3, 20% (at 403 nm) with 3.0 s, 34% (at 545 nm) with 2.8 s, 39% (at 770 nm) with 3.4 s, and 61% (at 1530 nm) with 3.8 s for P4 (Table 3.5). Among these four polymers, P1 obtained relatively better optical contrast and switching time values compared to other polymers. As is mentioned above, these results can be dedicated to electron-rich nature and better electron-donating ability of thieno[3,2-b]thiophene.

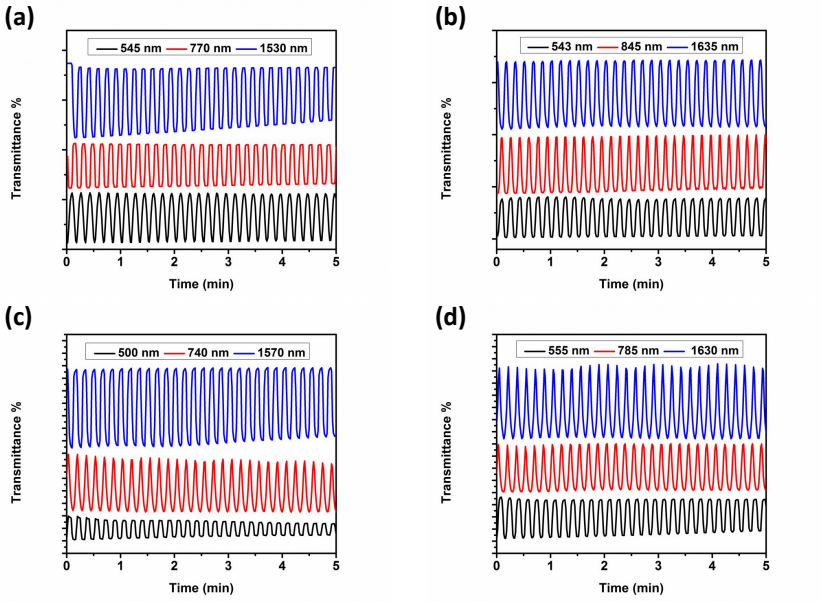

Figure 3.16: Change in the percent transmittance observed at the absorption maxima of the polymers (a) P1, (b) P2, (c) P3, and (d) P4 in a 0.1 M $TBAPF_6$ /ACN electrolyte solution.

The absorption spectrum of the polymer solution in chloroform and polymer thin film was obtained using a UV-Vis spectrophotometer (Figure 3.17). All polymers exhibited red-shift absorption in thin-film polymer compared to the polymer solution. This red-shift could be explained by reducing conformation change freely, high π-electron delocalization on a planar solid state, or the polymer and solvent interaction. (Table 3.6)

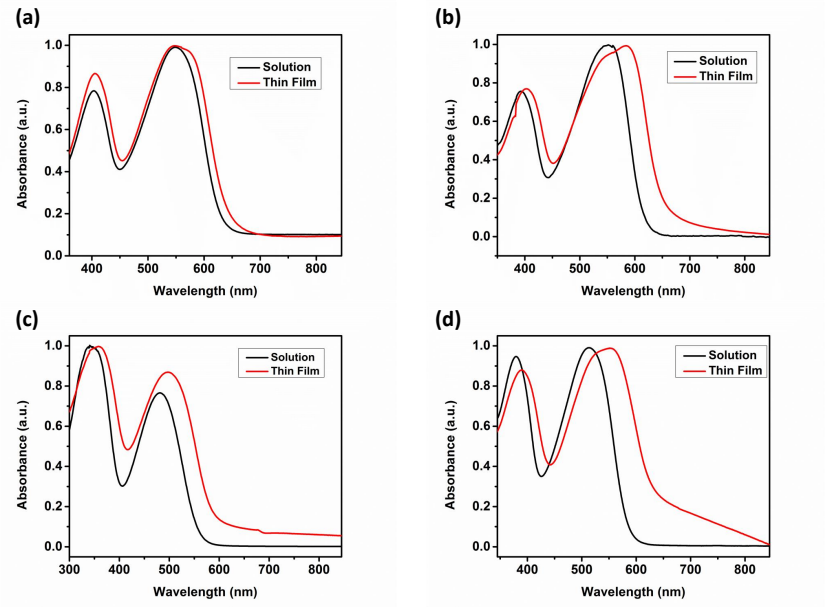

Figure 3.17: Absorption spectra of the polymers (a) P1, (b) P2, (c) P3, and (d) P4 solutions in chloroform and polymer thin film.

Table 3.6: Optical properties of P1, P2, P3, and P4 in chloroform solution and thin film form.

	Solution Λ (nm)	Thin Film Λ (nm)
P1	403	405
	547	549
P2	393	402
	551	583
P3	340	358
	481	497
P4	379	389
	512	552

3.2.3 Photovoltaic Studies

Electrochemical works showed that all polymers have suitable band gaps and HOMO-LUMO energy levels to construct organic bulk- heterojunction solar cells. ITO/PE-

DOT:PSS/Polymer: $PC_{71}BM$/ LiF/Al based device architecture was fabricated for all polymers apart from P3. Because of the low yield of the polymerization reaction, the amount of P3 was not enough for device fabrication. Current density-voltage (J-V) properties of the BHJ devices were determined under light illumination (AM 1.5 G with 100 mW/cm^2). In order to determine the most effective devices, wide variety of optimizations were conducted such as polymer and $PC_{71}BM$ blend ratio (w:w), blend concentration, and thickness optimizations. The thickness optimizations were recorded by changing the rate of spin coating. . In order to enhance the device performance, the solvent additive is used, and only P1 showed better performance in the addition of DPE as a solvent additive (4.25%). For P2, 2% CN and 3% DPE, and for P4, 2% DIO and 3% DPE additive treatments were performed. However, PCEs were below 0.2%. The dissociation of exciton and transport of charge carriers directly related to donor and acceptor arrangements on the morphology. Therefore, the decrease in the PCEs of P2 and P3 could be probably deterioration of the morphology in the presence of additives, whereas the improvement of PCE of P1 could be probably the additive treatment which enhancing morphology. All photovoltaic works of the novel three polymers are reported below.

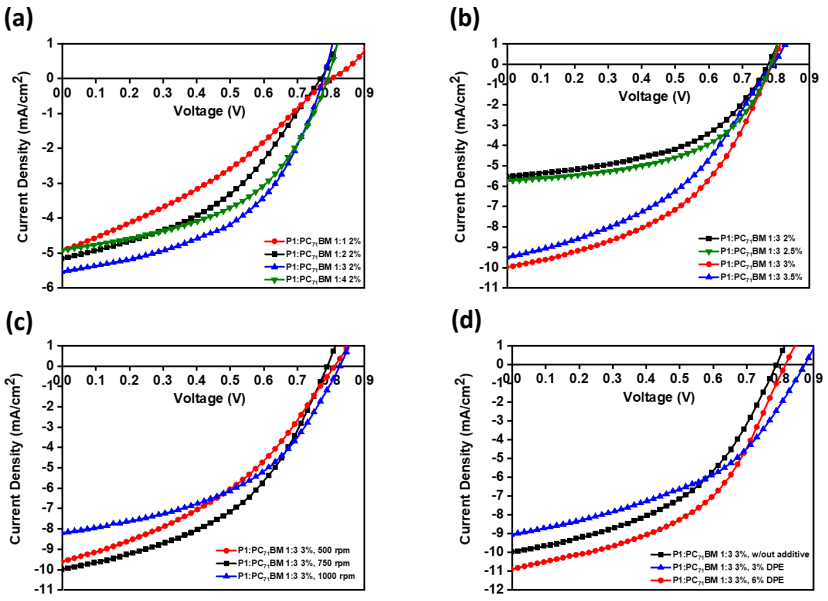

Figure 3.18: Current density-voltage curves of P1 for study of a) blend ratio b) concentration c) thickness d) additive.

According to photovoltaic results, the highest performance belongs to thienothiophene containing P1 with 1:3 (w:w) P1:$PC_{71}BM$ blend ratio with 3% concentration in the addition of 6% DPE at 750 rpm (Figure 3.18). This device exhibited the highest PCE as 4.25%, J_{SC} as 10.89 mA/cm2, V_{OC} as 0.82 V and FF as 47.74%. For selenophene containing P2, the highest PCE as 2.26%, J_{SC} as 8.31 mA/cm^2, V_{OC} as 0.74 V and FF as 36.94%. For thiophene containing P4, the highest PCE as 0.84%, J_{SC} as 3.82 mA/cm^2, V_{OC} as 0.69 V and FF as 31.86%. The increasing PCE from P4, P2, and P1 as 0.82%, 2.26%, and 4.25%, respectively, is expected. Since the molecular weight of the polymers also exhibited a similar trend. When the chain length of the polymer raises, the intermolecular charge hopping raises, and therefore PCE enhances [64].

Table 3.7: Photovoltaic parameters of P1 based BHJ solar cell.

Polymer(P1):$PC_{71}BM$	J_{SC}	V_{OC}	FF%	PCE%	RPM	Treatment
1:1 (2%)	4.92	0.81	32.78	1.30	750	-
1:2 (2%)	5.14	0.77	41.64	1.66	750	-
1:3 (2%)	5.52	0.78	49.13	2.11	750	-
1:4 (2%)	4.92	0.79	48.37	1.86	750	-
1:3 (2.5%)	5.74	0.79	52.47	2.38	750	-
1:3 (3%)	9.96	0.79	45.61	3.60	750	-
1:3 (3.5%)	9.46	0.80	41.40	3.12	750	-
1:3 (3%)	9.59	0.81	38.81	3.02	500	-
1:3 (3%)	8.19	0.83	46.09	3.14	1000	-
1:3 (3%)	9.03	0.87	44.67	3.53	750	DPE (3%)
1:3 (3%)	10.89	0.82	47.74	4.25	750	DPE (6%)

The current density- voltage (J-V) curves of the P1 based BHJ devices were reported for blend ratios, concentrations, thickness at different spin coating rates, and additive percent's (Figure 3.18). The PCE of P1 is enhanced from 2.11% to 3.60% when the concentration is increased from 2% to 3% at 1:3 blend ratio in the o-DCB solvent at 750 rpm. As the polymer:PCBM concentration in the active layer raises, light absorption raises, and which leads to better solar performances. The best device with the highest PCE is gained when the additive, namely diphenyl ether (DPE), is added.

Since the additive treatment makes enhancement on exciton dissociation and charge transport; therefore, photovoltaic efficiency increases [65]. When the additive percent raised from 3% to 6%, the PCE raised to 4.24%. This can be attributed to further improvement of the morphology when 6% additive is used compared to 3% additive.

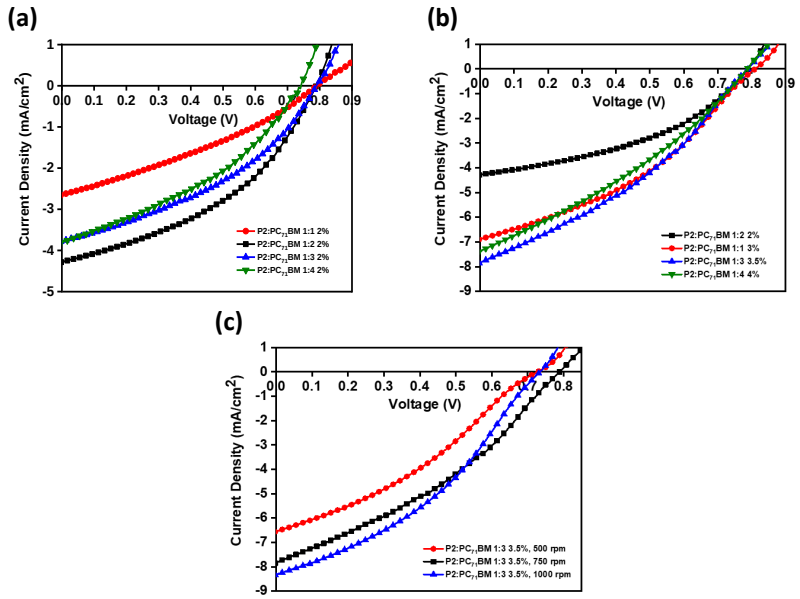

Figure 3.19: Current density-voltage curves of P2 for study of a) blend ratio b) concentration c) thickness.

Table 3.8: Photovoltaic parameters of P2 based BHJ solar cell.

Polymer(P2):$PC_{71}BM$	J_{SC}	V_{OC}	FF%	PCE%	RPM
1:1 (2%)	2.65	0.80	32.01	0.67	750
1:2 (2%)	4.28	0.79	41.28	1.40	750
1:3 (2%)	3.78	0.79	38.85	1.16	750
1:4 (2%)	3.80	0.74	36.95	1.04	750
1:2 (3%)	6.88	0.81	36.98	2.07	750
1:2 (3.5%)	7.82	0.79	34.25	2.13	750
1:2 (4%)	7.37	0.79	32.00	1.86	750
1:2 (3.5%)	6.54	0.73	33.14	1.58	500
1:2 (3.5%)	8.31	0.74	36.94	2.26	1000

For P2 based devices, J-V curves were drawn for blend ratio, concentration, and thickness works (Figure 3.19). According to photovoltaic data, the J_{SC} , FF and PCE values reduces as the blend ratio alters from 1:2 to 1:4 (Table 3.8). This is because of decreasing polymer amount and increasing PCBM amount in the blend ratio result in decreasing J_{SC} value. The device efficiency is improved when concentration is 3.5% in the o-DCB solvent. Compared to 500 and 750 rpm, the best device is obtained at 1000 rpm. When the coating rate increases, the J_{SC} value also increases because the mobility of the charge carriers increases when the thickness of the active layer decreases [66]. Finally, the J-V graphs were drawn for P4 based polymer for the study of blend ratio, concentration, and thickness (Figure 3.20). The highest PCE value is gained as 0.84% when blend ratio is 1:3 with 2% concentration in o-DCB solvent at 750 rpm (Table 3.9). When concentration raised from 2% to 3%, PCE reduced from 0.84% to 0.36%. This result can be devoted to reduction of J_{SC} value from 3.82 to 2.09 since ability of light absorption is directly related with J_{SC} value. As J_{SC} value increases, light absorption of the device, therefore; PCE increases.

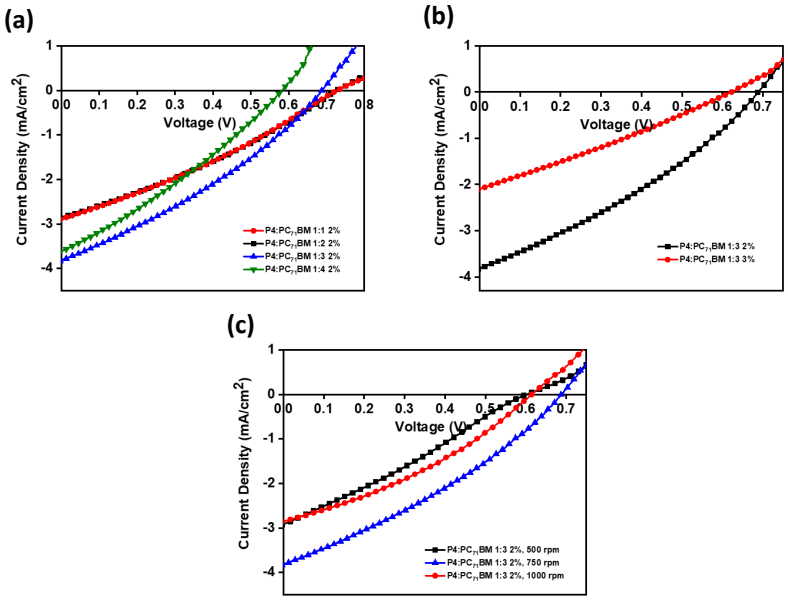

Figure 3.20: Current density-voltage curves of P2 for study of a) blend ratio b) concentration c) thickness.

Table 3.9: Photovoltaic parameters of P4 based BHJ solar cell.

Polymer(P4):$PC_{71}BM$	J_{SC}	V_{OC}	FF%	PCE%	RPM
1:1 (2%)	2.85	0.73	30.74	0.64	750
1:2 (2%)	3.26	0.72	30.45	0.72	750
1:3 (2%)	3.82	0.69	31.86	0.84	750
1:4 (2%)	3.61	0.58	29.92	0.63	750
1:3 (3%)	2.09	0.62	27.77	0.36	750
1:3 (2%)	2.90	0.60	27.90	0.49	500
1:3 (2%)	2.85	0.62	33.52	0.59	1000

3.2.4 Morphological Works

For solar cell devices, the structure of bi-continuous network is needed in order to obtain higher device performances. The suitable domain size is required in order to electron-hole couples to reach the interface between donor and acceptor layers at which charge generation occurs [67]. Therefore, TEM images of the best device performance polymer films were taken to gain insight into the morphology of the P1, P2, and P4. In TEM images, the darker places represent the places where PCBM is rich, and the lighter places represent the places where the polymer is rich (Figure 3.21). As it is seen from the TEM images, P1: $PC_{71}BM$ blend has the most homogenous morphology, whereas there are some defects on P2: $PC_{71}BM$ and P4: $PC_{71}BM$ blends, which correspond to aggregation of $PC_{71}BM$. In literature, it is stated that the defects on the morphology can lead to lower FF and J_{SC} values [68].

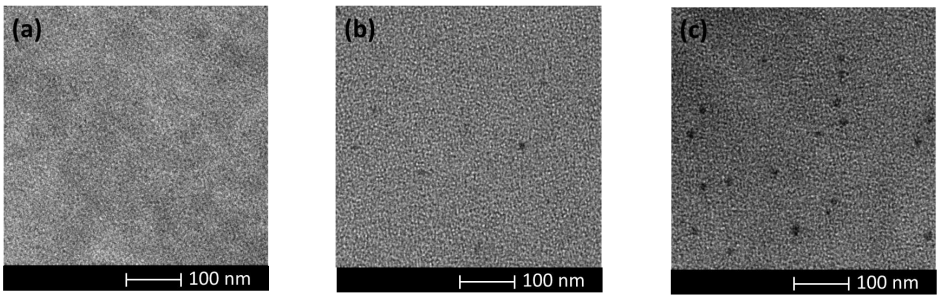

Figure 3.21: TEM images of a) P1:$PC_{71}BM$ (1:3 / w:w) blend with 6% DPE at 750 rpm, b) P2:$PC_{71}BM$ (1:2 / w:w) blend, c) P4 :$PC_{71}BM$ (1:3 / w:w) blend.

3.2.5 Computational Studies

Although all the single chains were predicted to have helical structures in the long range, the diameter of these helices are larger and chains are relatively more linear for P1 and P2. ESP surfaces mapped on the tetramers showed that electron rich part represented by red color are concentrated not only on the fluorene donor and bridging units but also on the alkoxy oxygen and fluorine atoms on the acceptor. Electron deficient parts are distributed on the benzothiadiazole acceptor backbone, alkyl side chain of the alkoxy group in acceptor and hydrogen atoms on the donor and bridging unit. The backbones of the chains have a relatively good donor-acceptor distribution along the chain. While P1 shows highest level of repeating ESP donor-acceptor pattern, P3 that has lowest planarity, also have the lower repeating pattern for ESP. HOMO and HOMO-1 orbital surfaces are highly delocalized both on the donors and acceptors. HOMO and HOMO-1 are complementary where HOMO surfaces are mostly on the middle and HOMO-1 surfaces are on the end groups of the tetramer chain. Contrary, LUMO and LUMO+1 are highly localized on the acceptor and neighboring bridging units.

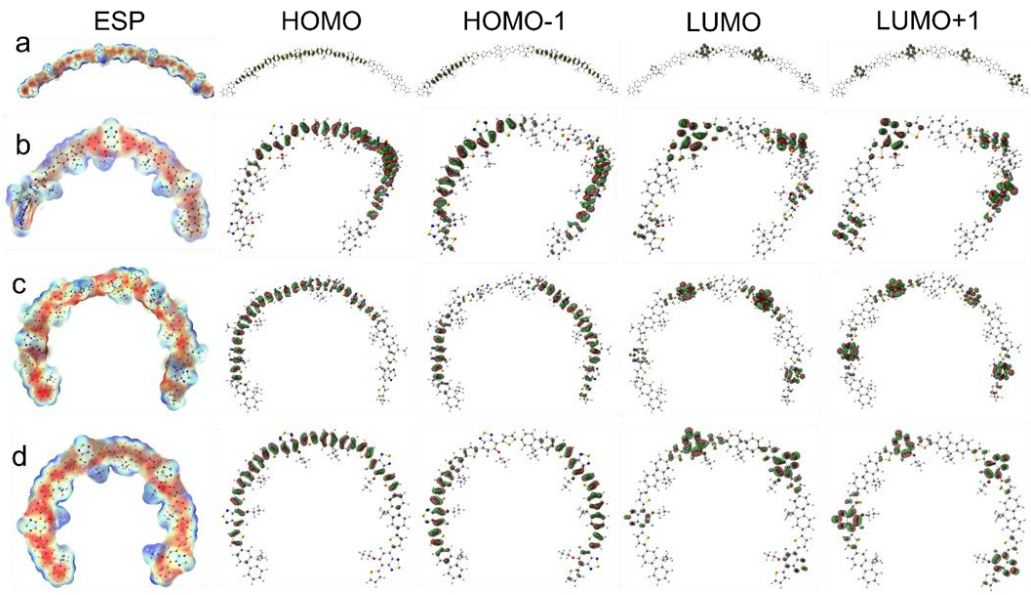

Figure 3.22: Electrostatic potential surface (ESP) and frontier orbital surfaces (HOMO, HOMO-1, LUMO, LUMO+1) for the a) P1, b) P2, c) P3, d) P4 copolymers.

Dihedral angles (θ) between donor, acceptor and bridging units are given in (Table 3.10). Two different types of angles were present between acceptors and bridging units due to the -F and alkoxy substitutions at the two sides of benzothiadiazole acceptor unit. -F substitution did not affect on planarity and the angles were below 1° for P1, P2 and P4, which is slightly larger for P3. However, alkoxy substitution change planarity significantly where dihedral angles are between 10-12° for all bridging units. The most important difference in the planarity of the chains is due the dihedral angle between fluorene donor and bridging units. The torsional angles between donor and bridging unit of P3 is 47.30° due to the repulsions between alkyl side chains which significantly reduce physical and electronic properties. P1, P2 and P4 have 28-30° angle between donor and acceptor units. The planarity of P1, P2 and P4 have close values where all of them presented a helical structures in the long range, with higher helical diameter and increased linearity for P1. Close values were determined three copolymers other than P3, for the VIP, AIP, VEA and AEA values. P1 and P2 have relatively lower positive ionization potential and more negative electron affinity, that are preferred electronic properties for a successful donor-acceptor chain.

Band gaps also have close values for P1, P2 and P4, with the exception of nonplanar P3, where the calculated values are in good agreement with experimental values with their optical band gaps values below 2 eV. The difference in the experimental and computational values may due to the limited chain length in calculations as well as interchain interactions that are not covered in the theoretical calculations. Higher planarity of the chains that leads to the better interchain packing resulted in the lower band compared to the single chain calculations and the most red-shifted neutral state absorption in the experiments. λreorg values which is inversely proportional with the mobility is slightly lower for P1 leading to the higher hole mobility. Dipole moment (μ), polarizability (α) and hyperpolarizability (β) values are also given in (Table 3.10). Significantly higher values of α and β were determined for P1 compared to other copolymers. There is a relation between molecular hyperpolarizability, β, and the bond-length alternation in conjugated chains where β increases with increasing electron delocalization and decreasing bond length alternation [69]. β values have the order of P1>P2>P4>P3 that agrees well with the experimental results. Higher polarizability and hyperpolarizability values for P1 also indicated the stronger dispersion and dipole-dipole intermolecular interactions with other species such as $PC_{71}BM$. Finally, atomic charges by ESP fitting on the donor, acceptor and bridging unit for the two repeating unit in the middle of tetramers were calculated by neglecting end groups to avoid end group effect. All copolymers have electron transfer from donor to acceptor according to these atomic charges. There are significant positive charges formed on the fluorene donor that demonstrate its efficiency as a donor unit. Bridging units have negative charges that agrees with the LUMO levels which observed to be extended from acceptor to the bridges.

Table 3.10: Results of the DFT calculations for the electronic and structural properties of P1-P4 in eV.

	PTBTT	PHTBTHT	PFBTF	PTTBTTT
θ A-B	0.16 / 10.83	0.37 / 11.24	3.55 / 10.25	0.35 / 11.60
θ D-B	29.88	29.69	47.30	28.47
HOMO	-5.10	-5.12	-5.18	-5.12
LUMO	-2.95	-2.90	-2.76	-2.88
E_g^{el}	2.15	2.21	2.42	2.24
E_g^{op}	1.84	1.88	2.11	1.90
VIP	5.52	5.60	5.66	5.63
AIP	5.48	5.40	5.61	5.57
VEA	-2.51	-2.41	-2.25	-3.37
AEA	-2.54	-2.60	-2.29	-2.41
Λ_{reorg}	0.08	0.11	0.10	0.11
μ	1.84	1.41	1.89	1.38
α	889.83	677.02	687.79	640.79
β	29617.20	19878.72	9565.84	17309.49
Charge Acceptor	-0.14	-0.22	-0.46	-0.48
Charge Donor	0.67	0.54	0.65	0.54
Charge Bridge	-0.26	-0.18	-0.11	-0.03

CHAPTER 4

CONCLUSION

Novel 2,1,3-benzothiadiazole comprising monomers were successfully synthesized and characterized by HRMS and NMR spectroscopy. They were coupled with furan, thiophene, 3-hexylthiophene, selenophene, and thienothiophene to explore the effect of these bridging units on the optoelectronic properties and OPV device construction. Electrochemical, spectroelectrochemical, optical and computational characterizations of the polymers were conducted successfully. PTBTT, PFBTF, PTHTBTHT, and PTTBTTT are synthesized by electrochemical polymerization by using cyclic voltammetry. Among these homopolymers thiophene, and thienothiophene containing polymers exhibited ambipolar character. Besides, the lowest oxidation potential belongs to PTTBTTT as 1.3 V. According to spectroelectrochemical studies, the most red-shifted polymer is PFBTF, with the lowest optical bandgap as 1.57 eV. In addition, all polymers show multi-electrochromic behavior, and colorimetric analysis was carried out at neutral, oxidized, and reduced states of the polymers. The neutral state colors of all polymers are consistent with UV-Vis- NIR absorption spectra of the polymers. Kinetic studies revealed that the highest optical contrast at the highest neutral state absorption wavelength belongs to PHTBTHT with 37%. The novel alternating conjugated polymers, namely P1, P2, P3, and P4, were synthesized by coupling the monomers with the fluorene donor unit via Suzuki polycondensation reaction. The molecular weight of the polymers was acquired by gel permeation chromatography. According to electrochemical studies, P3 and P4 are both p- dopable and n-dopable. Spectroelectrochemical studies showed that the lowest optical bandgap belongs to P4 as 1.73 eV. All polymers showed multi-electrochromic behavior at neutral, oxidized, and reduced states. The colors of the polymers are consistent with the neutral state absorption spectra. Besides, they exhibited the tones of grey color in their oxidized

states. Optical studies revealed that at highest neutral state absorption wavelength belongs to P1 with 50% percent transmittance. According to UV- Vis spectra, all polymers exhibited red-shift absorption in polymer thin film compared to polymer solution in chloroform. BHJ solar cell device architectures were constructed for P1, P2, and P4. The power conversion efficiencies were reported as 4.25%, 2.26%, and 0.84% respectively under illumination (AM 1.5 G, 100 mW cm^2). Results were discussed by comparing with the theoretical calculations.

REFERENCES

[1] A. J. Banister and I. B. Gorrell, "Poly (sulfur nitride): The first polymeric metal," *Advanced Materials*, vol. 10, no. 17, pp. 1415–1429, 1998.

[2] H. Shirakawa, E. J. Louis, A. G. MacDiarmid, C. K. Chiang, and A. J. Heeger, "Synthesis of electrically conducting organic polymers: halogen derivatives of polyacetylene,(ch) x," *Journal of the Chemical Society, Chemical Communications*, no. 16, pp. 578–580, 1977.

[3] A. J. Heeger, "Nobel lecture: Semiconducting and metallic polymers: The fourth generation of polymeric materials," *Reviews of Modern Physics*, vol. 73, no. 3, p. 681, 2001.

[4] L. Dou, Y. Liu, Z. Hong, G. Li, and Y. Yang, "Low-bandgap near-ir conjugated polymers/molecules for organic electronics," *Chemical reviews*, vol. 115, no. 23, pp. 12633–12665, 2015.

[5] M. H. Harun, E. Saion, A. Kassim, N. Yahya, and E. Mahmud, "Conjugated conducting polymers: A brief overview," *UCSI Academic Journal: Journal for the Advancement of Science & Arts*, vol. 2, pp. 63–68, 2007.

[6] C. K. Chiang, C. Fincher Jr, Y. W. Park, A. J. Heeger, H. Shirakawa, E. J. Louis, S. C. Gau, and A. G. MacDiarmid, "Electrical conductivity in doped polyacetylene," *Physical review letters*, vol. 39, no. 17, p. 1098, 1977.

[7] K. M. Molapo, P. M. Ndangili, R. F. Ajayi, G. Mbambisa, S. M. Mailu, N. Njomo, M. Masikini, P. Baker, and E. I. Iwuoha, "Electronics of conjugated polymers (i): polyaniline," 2012.

[8] J. C. Costa, R. J. Taveira, C. F. Lima, A. Mendes, and L. M. Santos, "Optical band gaps of organic semiconductor materials," *Optical Materials*, vol. 58, pp. 51–60, 2016.

[9] H. Van Mullekom, J. Vekemans, E. Havinga, and E. Meijer, "Developments in the chemistry and band gap engineering of donor–acceptor substituted conjugated polymers," *Materials Science and Engineering: R: Reports*, vol. 32, no. 1, pp. 1–40, 2001.

[10] J.-L. Bredas, "Relationship between band gap and bond length alternation in organic conjugated polymers," *The Journal of chemical physics*, vol. 82, no. 8, pp. 3808–3811, 1985.

[11] M. Kertesz, C. H. Choi, and S. Yang, "Conjugated polymers and aromaticity," *Chemical reviews*, vol. 105, no. 10, pp. 3448–3481, 2005.

[12] J. Roncali, "Molecular engineering of the band gap of π-conjugated systems: Facing technological applications," *Macromolecular Rapid Communications*, vol. 28, no. 17, pp. 1761–1775, 2007.

[13] Y. Mao, M. Head-Gordon, and Y. Shao, "Unraveling substituent effects on frontier orbitals of conjugated molecules using an absolutely localized molecular orbital based analysis," *Chemical science*, vol. 9, no. 45, pp. 8598–8607, 2018.

[14] B. Pal, W.-C. Yen, J.-S. Yang, C.-Y. Chao, Y.-C. Hung, S.-T. Lin, C.-H. Chuang, C.-W. Chen, and W.-F. Su, "Substituent effect on the optoelectronic properties of alternating fluorene- cyclopentadithiophene copolymers," *Macromolecules*, vol. 41, no. 18, pp. 6664–6671, 2008.

[15] K.-H. Kim, H. Yu, H. Kang, D. J. Kang, C.-H. Cho, H.-H. Cho, J. H. Oh, and B. J. Kim, "Influence of intermolecular interactions of electron donating small molecules on their molecular packing and performance in organic electronic devices," *Journal of Materials Chemistry A*, vol. 1, no. 46, pp. 14538–14547, 2013.

[16] U. Salzner, "Does the donor- acceptor concept work for designing synthetic metals? 1. theoretical investigation of poly (3-cyano-3 '-hydroxybithiophene)," *The Journal of Physical Chemistry B*, vol. 106, no. 36, pp. 9214–9220, 2002.

[17] X. Wan, C. Li, M. Zhang, and Y. Chen, "Acceptor–donor–acceptor type molecules for high performance organic photovoltaics–chemistry and mechanism," *Chemical Society Reviews*, vol. 49, no. 9, pp. 2828–2842, 2020.

[18] B. Lüssem, M. Riede, and K. Leo, "Doping of organic semiconductors," *physica status solidi (a)*, vol. 210, no. 1, pp. 9–43, 2013.

[19] R. Fujimoto, Y. Yamashita, S. Kumagai, J. Tsurumi, A. Hinderhofer, K. Broch, F. Schreiber, S. Watanabe, and J. Takeya, "Molecular doping in organic semiconductors: fully solution-processed, vacuum-free doping with metal–organic complexes in an orthogonal solvent," *Journal of Materials Chemistry C*, vol. 5, no. 46, pp. 12023–12030, 2017.

[20] M. Rahaman, A. Aldalbahi, M. Almoiqli, and S. Alzahly, "Chemical and electrochemical synthesis of polypyrrole using carrageenan as a dopant: Polypyrrole/multi-walled carbon nanotube nanocomposites," *Polymers*, vol. 10, no. 6, p. 632, 2018.

[21] S. Sadki, P. Schottland, N. Brodie, and G. Sabouraud, "The mechanisms of pyrrole electropolymerization," *Chemical Society Reviews*, vol. 29, no. 5, pp. 283–293, 2000.

[22] J. Roncali, "Conjugated poly (thiophenes): synthesis, functionalization, and applications," *Chemical Reviews*, vol. 92, no. 4, pp. 711–738, 1992.

[23] H. Higashimura and S. Kobayashi, "Oxidative polymerization," *Encyclopedia of polymer science and technology*, pp. 1–37, 2002.

[24] K. Tsuchiya and K. Ogino, "Catalytic oxidative polymerization of thiophene derivatives," *Polymer journal*, vol. 45, no. 3, pp. 281–286, 2013.

[25] A. F. Littke and G. C. Fu, "The first general method for stille cross-couplings of aryl chlorides," *Angewandte Chemie International Edition*, vol. 38, no. 16, pp. 2411–2413, 1999.

[26] M. M. Heravi, E. Hashemi, and F. Azimian, "Recent developments of the stille reaction as a revolutionized method in total synthesis," *Tetrahedron*, vol. 70, no. 1, pp. 7–21, 2014.

[27] P. Espinet and A. M. Echavarren, "The mechanisms of the stille reaction," *Angewandte Chemie International Edition*, vol. 43, no. 36, pp. 4704–4734, 2004.

[28] A. Suzuki, "Organoborane coupling reactions (suzuki coupling)," *Proceedings of the Japan Academy, Series B*, vol. 80, no. 8, pp. 359–371, 2004.

[29] A. Suzuki, "Recent advances in the cross-coupling reactions of organoboron derivatives with organic electrophiles, 1995–1998," *Journal of Organometallic Chemistry*, vol. 576, no. 1-2, pp. 147–168, 1999.

[30] N. Miyaura and A. Suzuki, "Palladium-catalyzed cross-coupling reactions of organoboron compounds," *Chemical reviews*, vol. 95, no. 7, pp. 2457–2483, 1995.

[31] B. Liang, M. Dai, J. Chen, and Z. Yang, "Copper-free sonogashira coupling reaction with pdcl2 in water under aerobic conditions," *The Journal of organic chemistry*, vol. 70, no. 1, pp. 391–393, 2005.

[32] S. Thorand and N. Krause, "Improved procedures for the palladium-catalyzed coupling of terminal alkynes with aryl bromides (sonogashira coupling)," *The Journal of Organic Chemistry*, vol. 63, no. 23, pp. 8551–8553, 1998.

[33] R. Chinchilla and C. Nájera, "Recent advances in sonogashira reactions," *Chemical Society Reviews*, vol. 40, no. 10, pp. 5084–5121, 2011.

[34] N. Panwar, S. Kaushik, and S. Kothari, "Role of renewable energy sources in environmental protection: A review," *Renewable and sustainable energy reviews*, vol. 15, no. 3, pp. 1513–1524, 2011.

[35] A. M. Bagher, "Comparison of organic solar cells and inorganic solar cells," *International Journal of Renewable and Sustainable Energy*, vol. 3, no. 3, pp. 53–58, 2014.

[36] S. Najam and B. Kumar, "Organic solar cell: Operating principle, performance parameters, structures and its advantages," in *2018 5th IEEE Uttar Pradesh Section International Conference on Electrical, Electronics and Computer Engineering (UPCON)*, pp. 1–6, IEEE, 2018.

[37] N. Marinova, S. Valero, and J. L. Delgado, "Organic and perovskite solar cells: Working principles, materials and interfaces," *Journal of colloid and interface science*, vol. 488, pp. 373–389, 2017.

[38] W. Cao and J. Xue, "Recent progress in organic photovoltaics: device architecture and optical design," *Energy & Environmental Science*, vol. 7, no. 7, pp. 2123–2144, 2014.

[39] K. Vivek and G. Agrawal, "Organic solar cells: Design, architecture and novel concepts," *Energy Technology & Ecological Concerns: A Contemporary Approach*, p. 87.

[40] D. Kekuda, J.-H. Huang, K.-C. Ho, and C.-W. Chu, "Modulation of donor- acceptor interface through thermal treatment for efficient bilayer organic solar cells," *The Journal of Physical Chemistry C*, vol. 114, no. 6, pp. 2764–2768, 2010.

[41] S. Rafique, S. M. Abdullah, K. Sulaiman, and M. Iwamoto, "Fundamentals of bulk heterojunction organic solar cells: An overview of stability/degradation issues and strategies for improvement," *Renewable and Sustainable Energy Reviews*, vol. 84, pp. 43–53, 2018.

[42] O. A. Abdulrazzaq, V. Saini, S. Bourdo, E. Dervishi, and A. S. Biris, "Organic solar cells: a review of materials, limitations, and possibilities for improvement," *Particulate science and technology*, vol. 31, no. 5, pp. 427–442, 2013.

[43] B. Qi and J. Wang, "Fill factor in organic solar cells," *Physical Chemistry Chemical Physics*, vol. 15, no. 23, pp. 8972–8982, 2013.

[44] L. Xiao, B. Liu, X. Chen, Y. Li, W. Tang, and Y. Zou, "Fluorine substituted benzothiazole-based low bandgap polymers for photovoltaic applications," *RSC advances*, vol. 3, no. 29, pp. 11869–11876, 2013.

[45] H.-J. Jhuo, P.-N. Yeh, S.-H. Liao, Y.-L. Li, Y.-S. Cheng, and S.-A. Chen, "Review on the recent progress in low band gap conjugated polymers for bulk hetero-junction polymer solar cells," *Journal of the Chinese Chemical Society*, vol. 61, no. 1, pp. 115–126, 2014.

[46] J. Mahar, G. Shabir, P. A. Channar, A. Saeed, K. D. Belfield, M. Irfan, and A. Ul-Hamid, "Donor-pi-acceptor fluorene conjugates, based on chalcone and pyrimidine derivatives: an insight into structure-property relationship, photophysical and electrochemical properties," *Journal of Fluorescence*, pp. 1–8, 2020.

[47] A. Slodek, M. Matussek, M. Filapek, G. Szafraniec-Gorol, A. Szlapa, I. Grudzka-Flak, M. Szczurek, J. G. Malecki, A. Maron, E. Schab-Balcerzak, *et al.*, "Small donor–acceptor molecules based on a quinoline–fluorene system with promising photovoltaic properties," *European Journal of Organic Chemistry*, vol. 2016, no. 14, pp. 2500–2508, 2016.

[48] R. Abbel, A. P. Schenning, and E. Meijer, "Fluorene-based materials and their supramolecular properties," *Journal of Polymer Science Part A: Polymer Chemistry*, vol. 47, no. 17, pp. 4215–4233, 2009.

[49] X. Wang, Y. Sun, S. Chen, X. Guo, M. Zhang, X. Li, Y. Li, and H. Wang, "Effects of π-conjugated bridges on photovoltaic properties of donor-π-acceptor conjugated copolymers," *Macromolecules*, vol. 45, no. 3, pp. 1208–1216, 2012.

[50] S. UrRehman, A. Alam, S. Bibi, S. Sadaf, S. R. Khan, M. Shoaib, A. Q. Khan, M. Khan, and W. UrRehman, "The effect of different aromatic conjugated bridges on optoelectronic properties of diketopyrrolopyrrole-based donor materials for organic photovoltaics.," *Journal of Molecular Modeling*, vol. 26, no. 6, pp. 154–154, 2020.

[51] P. Stephens and F. Devlin, "Chabalowski, cf; frisch," *J. Phys. Chem*, vol. 98, pp. 11623–11627, 1994.

[52] V. Barone and M. Cossi, "Quantum calculation of molecular energies and energy gradients in solution by a conductor solvent model," *The Journal of Physical Chemistry A*, vol. 102, no. 11, pp. 1995–2001, 1998.

[53] M. Frisch, G. Trucks, H. Schlegel, G. Scuseria, M. Robb, J. Cheeseman, G. Scalmani, V. Barone, G. Petersson, H. Nakatsuji, *et al.*, "Wallingford," *CT: Gaussian Inc*, 2009.

[54] H. T. Turan, O. Kucur, B. Kahraman, S. Salman, and V. Aviyente, "Design of donor–acceptor copolymers for organic photovoltaic materials: a computational study," *Physical Chemistry Chemical Physics*, vol. 20, no. 5, pp. 3581–3591, 2018.

[55] E. A. Alkan, S. Goker, H. Sarigul, E. Yıldırım, Y. A. Udum, and L. Toppare, "The impact of [1, 2, 5] chalcogenazolo [3, 4-f]-benzo [1, 2, 3] triazole structure

on the optoelectronic properties of conjugated polymers," *Journal of Polymer Science*, vol. 58, no. 7, pp. 956–968, 2020.

[56] S. C. Cevher, G. Hizalan, E. Alemdar Yilmaz, D. Cevher, Y. Udum Arslan, L. Toppare, E. Yıldırım, and A. Cirpan, "A comprehensive study: Theoretical and experimental investigation of heteroatom and substituent effects on frontier orbitals and polymer solar cell performances," *Journal of Polymer Science*, vol. 58, no. 19, pp. 2792–2806, 2020.

[57] J.-L. Brédas, D. Beljonne, V. Coropceanu, and J. Cornil, "Charge-transfer and energy-transfer processes in π-conjugated oligomers and polymers: a molecular picture," *Chemical reviews*, vol. 104, no. 11, pp. 4971–5004, 2004.

[58] B. H. Besler, K. M. Merz Jr, and P. A. Kollman, "Atomic charges derived from semiempirical methods," *Journal of computational chemistry*, vol. 11, no. 4, pp. 431–439, 1990.

[59] K. Lin, S. Ming, S. Zhen, Y. Zhao, B. Lu, and J. Xu, "Molecular design of dbt/dbf hybrid thiophenes π-conjugated systems and comparative study of their electropolymerization and optoelectronic properties: from comonomers to electrochromic polymers," *Polymer Chemistry*, vol. 6, no. 25, pp. 4575–4587, 2015.

[60] N. Akbaşoğlu, A. Balan, D. Baran, A. Cirpan, and L. Toppare, "Electrochemical and optical studies of furan and thieno [3, 2-b] thiophene end capped benzotriazole derivatives," *Journal of Polymer Science Part A: Polymer Chemistry*, vol. 48, no. 23, pp. 5603–5610, 2010.

[61] S. Goker, G. Hizalan, E. Aktas, S. Kutkan, A. Cirpan, and L. Toppare, "2, 1, 3-benzooxadiazole, thiophene and benzodithiophene based random copolymers for organic photovoltaics: thiophene versus thieno [3, 2-b] thiophene as π-conjugated linkers," *New Journal of Chemistry*, vol. 40, no. 12, pp. 10455–10464, 2016.

[62] N. A. O. LU, A. BALAN, D. BARAN, A. CIRPAN, and L. TOPPARE, "Electrochemical and optical studies of furan and thieno [3, 2-b] thiophene end capped benzotriazole derivatives,"

[63] D. Baran, A. Balan, S. Celebi, B. Meana Esteban, H. Neugebauer, N. S. Sariciftci, and L. Toppare, "Processable multipurpose conjugated polymer for electrochromic and photovoltaic applications," *Chemistry of Materials*, vol. 22, no. 9, pp. 2978–2987, 2010.

[64] Ö. Karagaçti, "New quinoxaline containing donor-acceptor type conjugated polymers for organic solar cells," Master's thesis, MIDDLE EAST TECHNICAL UNIVERSITY, 2018.

[65] T. H. Lee, S. Y. Park, B. Walker, S.-J. Ko, J. Heo, H. Y. Woo, H. Choi, and J. Y. Kim, "A universal processing additive for high-performance polymer solar cells," *RSC advances*, vol. 7, no. 13, pp. 7476–7482, 2017.

[66] R. Ginting, C. Yap, M. Yahaya, V. Fauzia, and M. Salleh, "Active layer spin coating speed dependence of inverted organic solar cell based on eosin-y-coated zno nanorod arrays," in *Journal of Physics: Conference Series*, vol. 431, p. 012016, IOP Publishing Ltd., 2013.

[67] K. Goksu, G. Hizalan, Y. A. Udum, S. O. Hacioglu, S. C. Cevher, L. Toppare, A. Cirpan, *et al.*, "Syntheses and characterization of benzotriazole, thienopyrroledione, and benzodithiophene containing conjugated random terpolymers for organic solar cells," *Journal of The Electrochemical Society*, vol. 166, no. 15, p. H849, 2019.

[68] A. Cetin, C. Istanbulluoglu, S. O. Hacioglu, S. C. Cevher, L. Toppare, and A. Cirpan, "Synthesis of bistriphenylamine-and benzodithiophene-based random conjugated polymers for organic photovoltaic applications," *Journal of Polymer Science Part A: Polymer Chemistry*, vol. 55, no. 22, pp. 3705–3715, 2017.

[69] S. M. Risser, D. N. Beratan, and S. R. Marder, "Structure-function relationships for. beta., the first molecular hyperpolarizability," *Journal of the American Chemical Society*, vol. 115, no. 17, pp. 7719–7728, 1993.

APPENDIX A

NMR SPECTRA

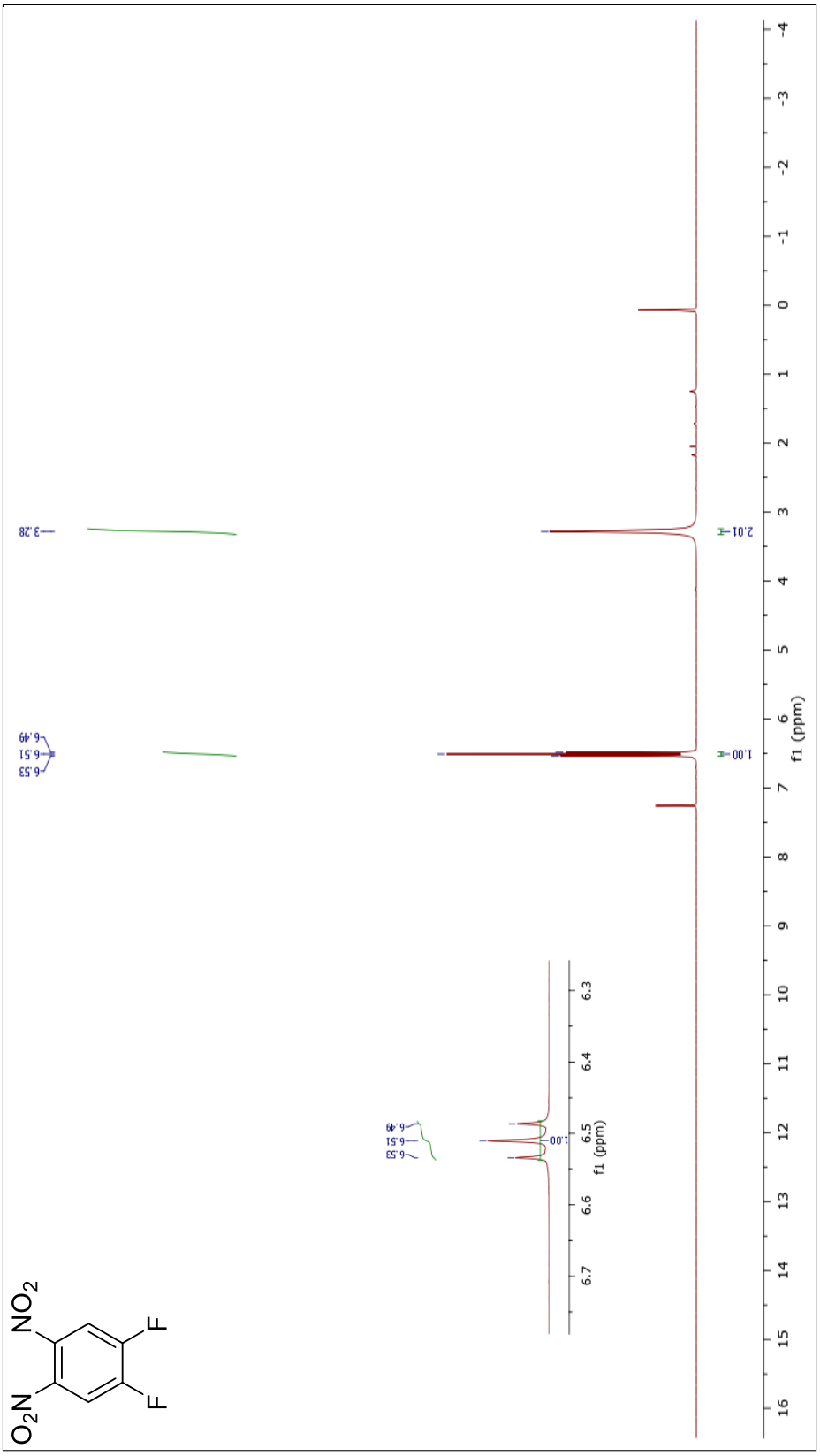

Figure A.1: ^{1}H NMR spectrum of 4,5-difluorobenzene-1,2-diamine.

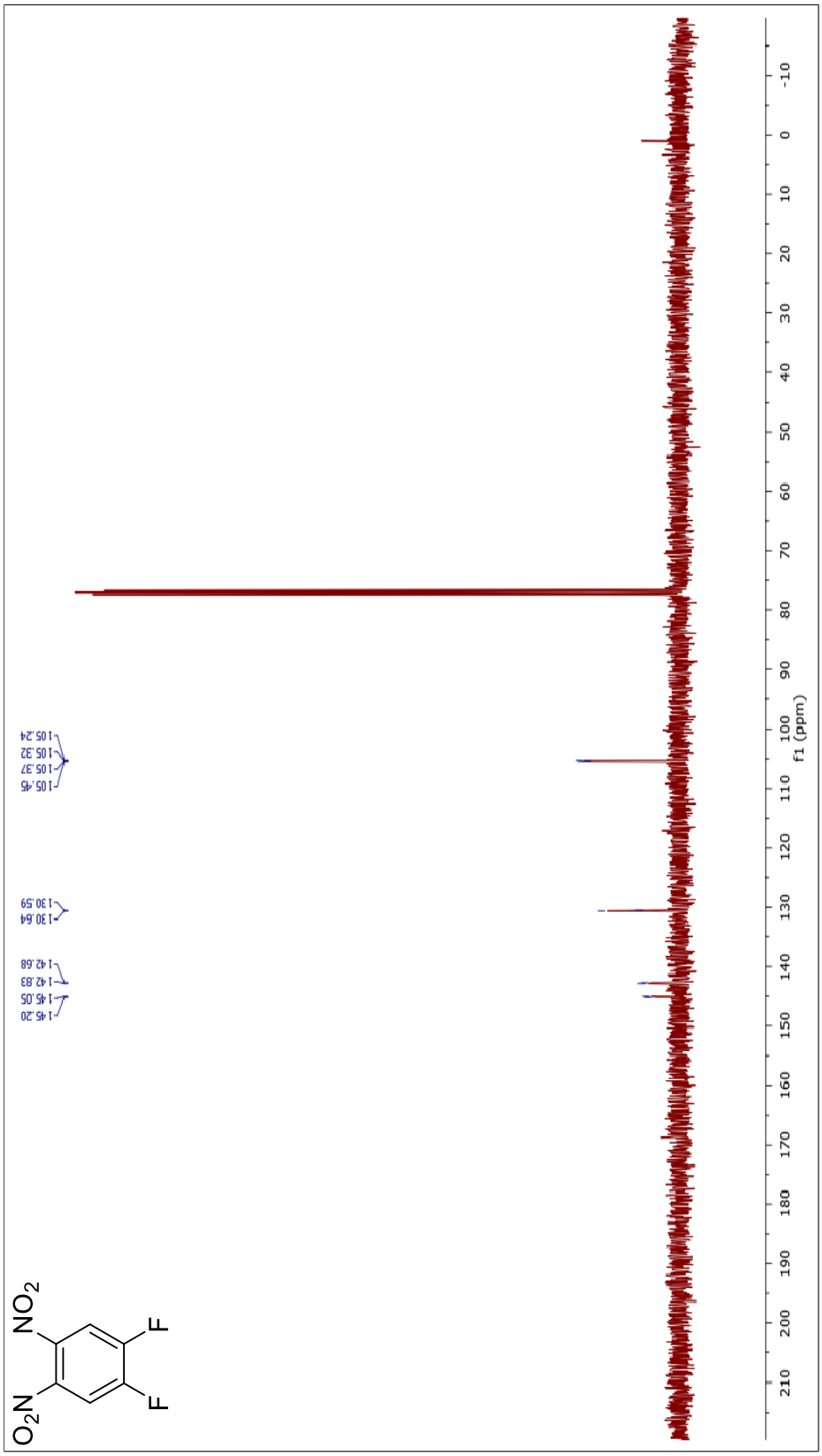

Figure A.2: ^{13}C NMR spectrum of 4,5-difluorobenzene-1,2-diamine.

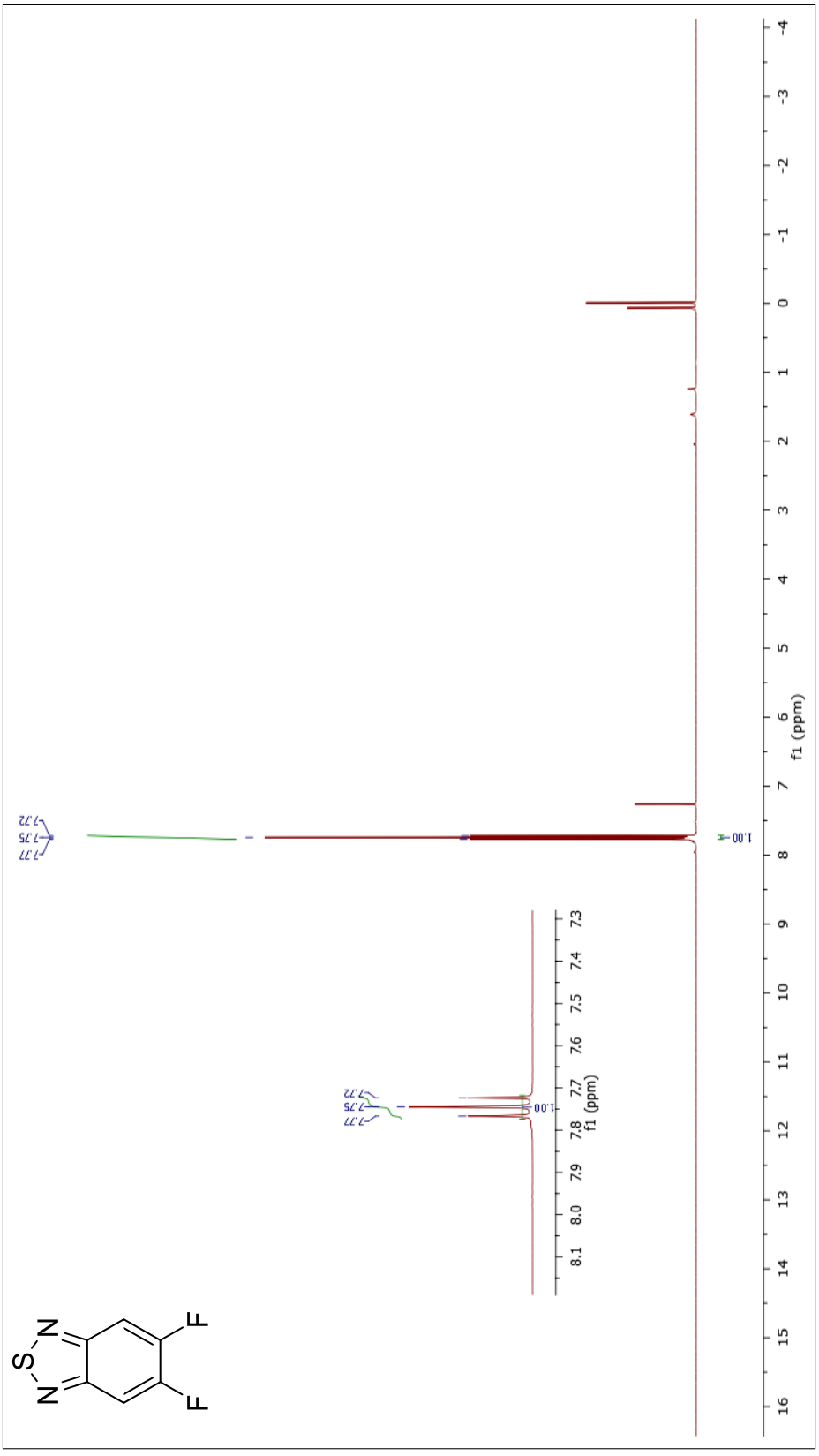

Figure A.3: ^{1}H NMR spectrum of 5,6-difluorobenzo[c][1,2,5]thiadiazole.

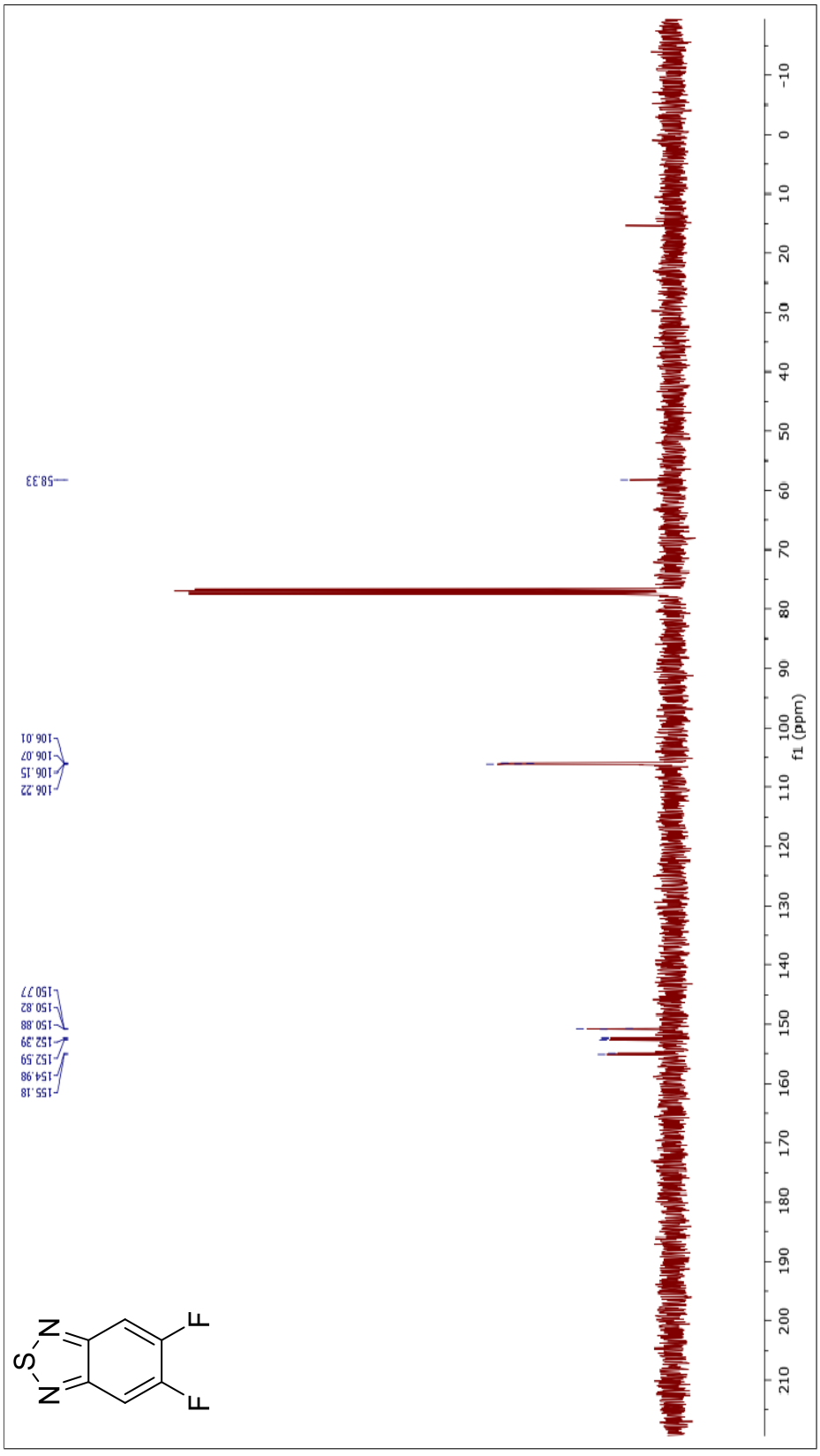

Figure A.4: ^{13}C NMR spectrum of 5,6-difluorobenzo[c][1,2,5]thiadiazole.

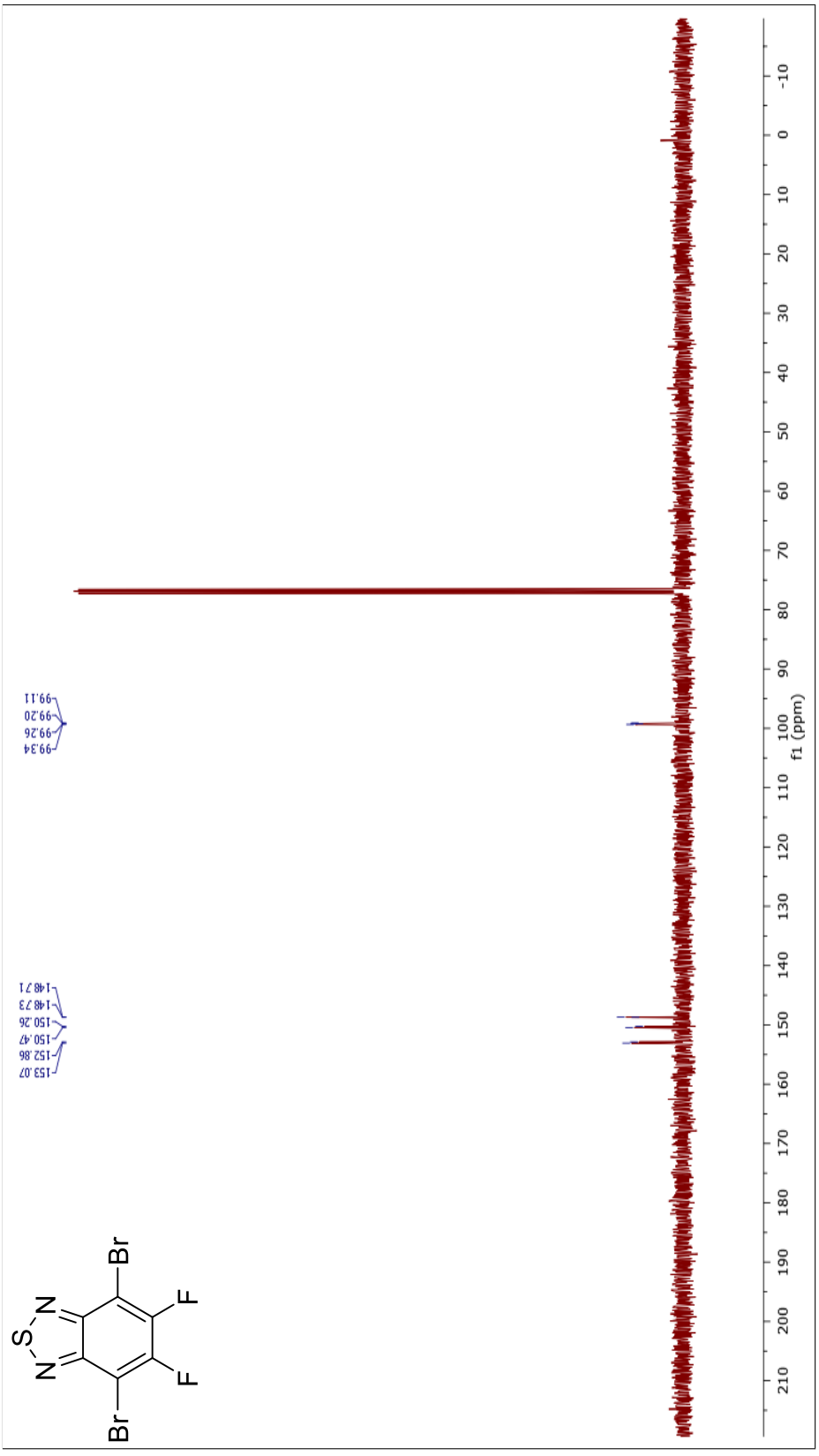

Figure A.5: ^{13}C NMR spectrum of 4,7-dibromo-5,6-difluorobenzo
c
[1,2,5]thiadiazole .

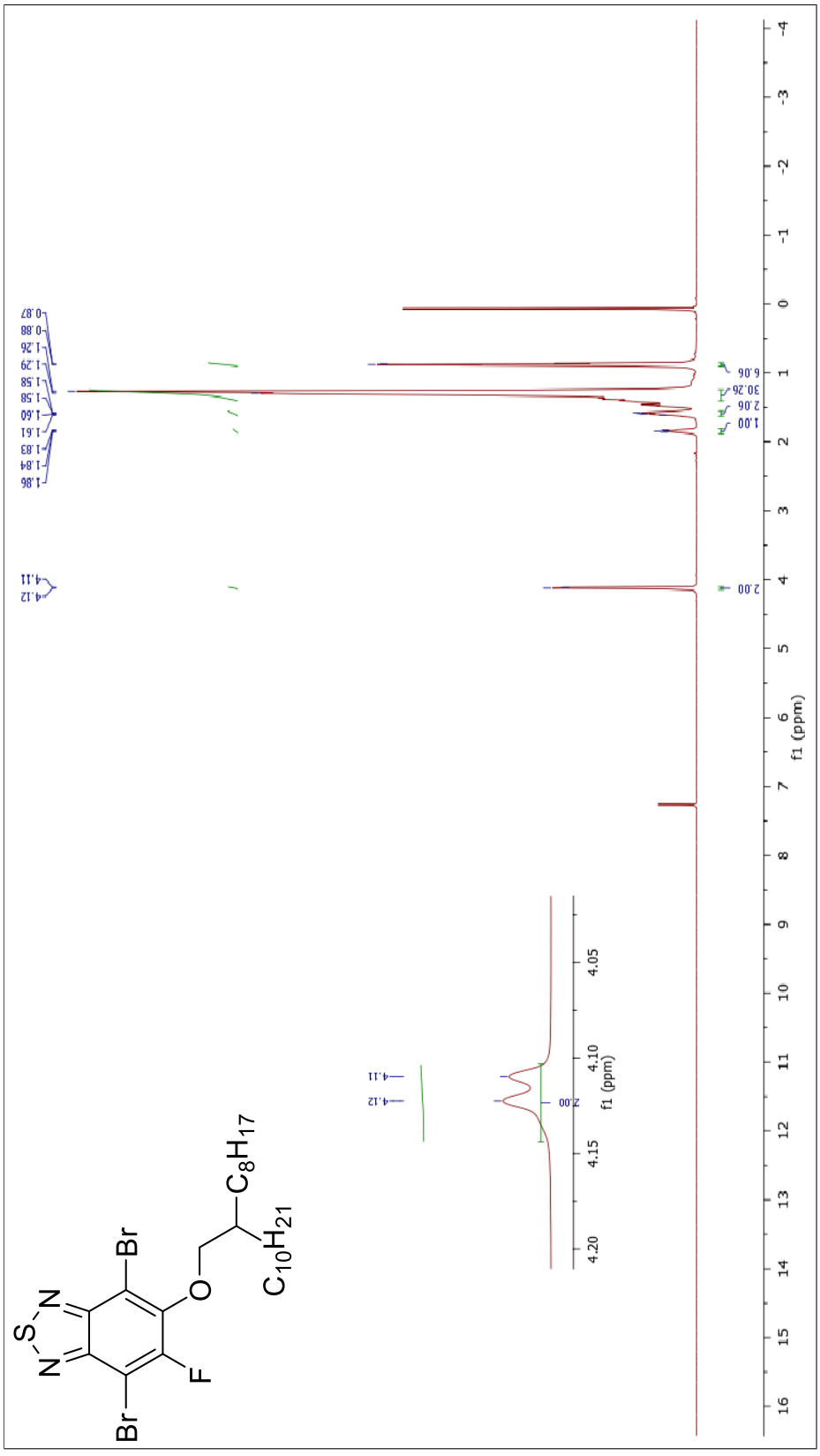

Figure A.6: ^{1}H NMR spectrum of 4,7-dibromo-5-fluoro-6-((2-octyldodecyl)oxy) benzo[c][1,2,5]thiadiazole.

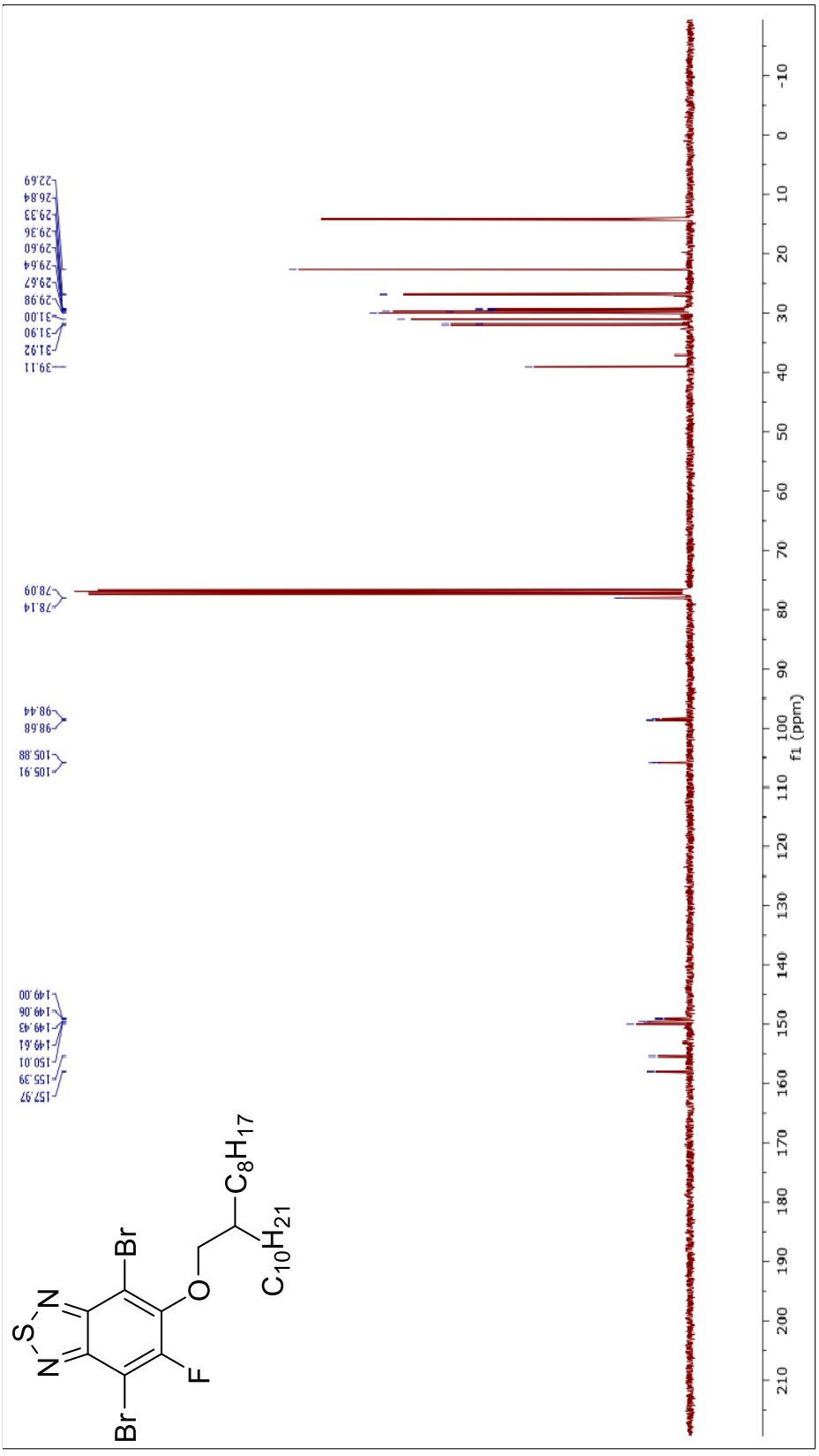

Figure A.7: ^{13}C NMR spectrum of 4,7-dibromo-5-fluoro-6-((2-octyldodecyl)oxy) benzo[c][1,2,5]thiadiazole.

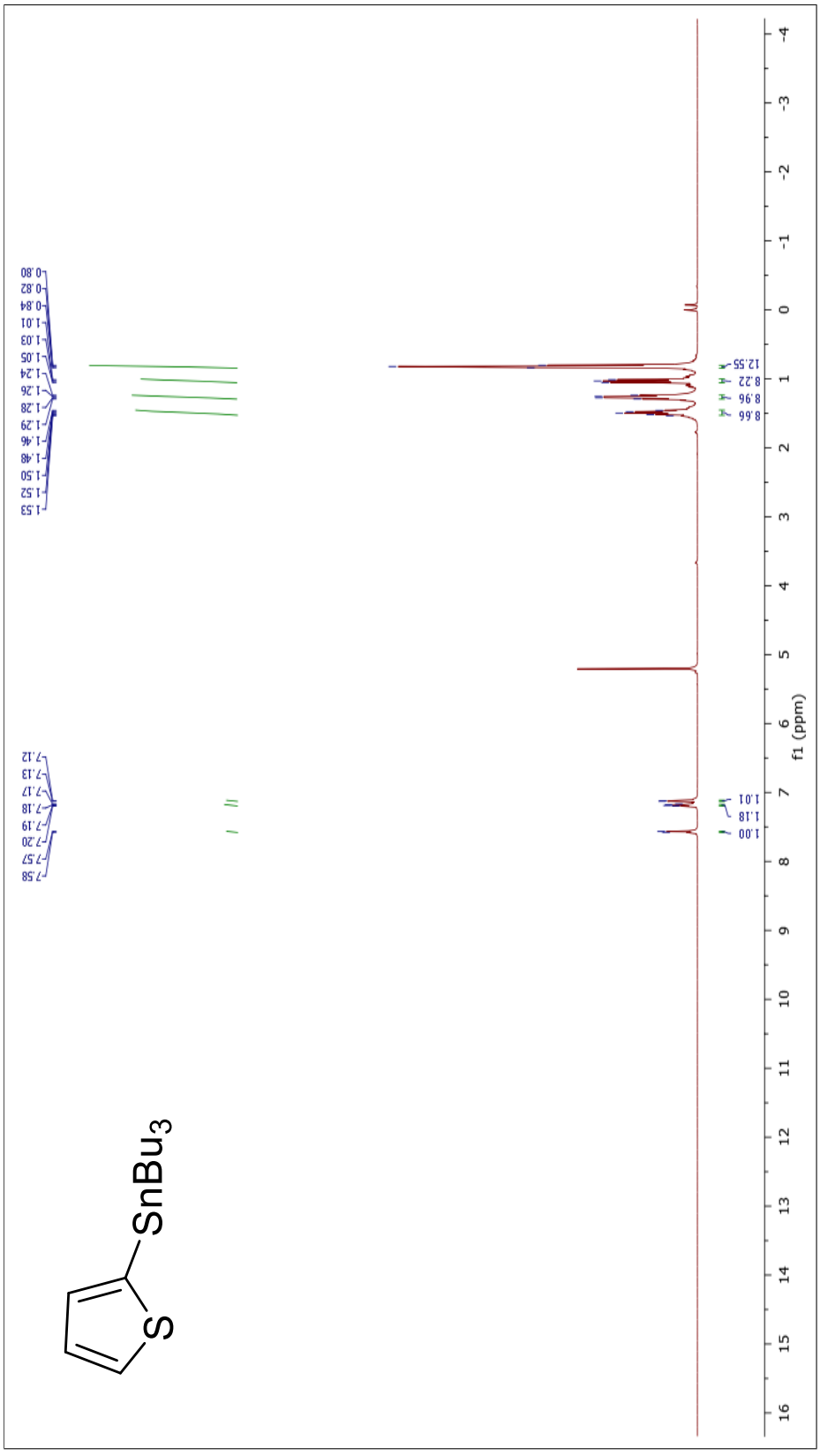

Figure A.8: ^{1}H NMR spectrum of tributyl(thiophen-2-yl)stannane.

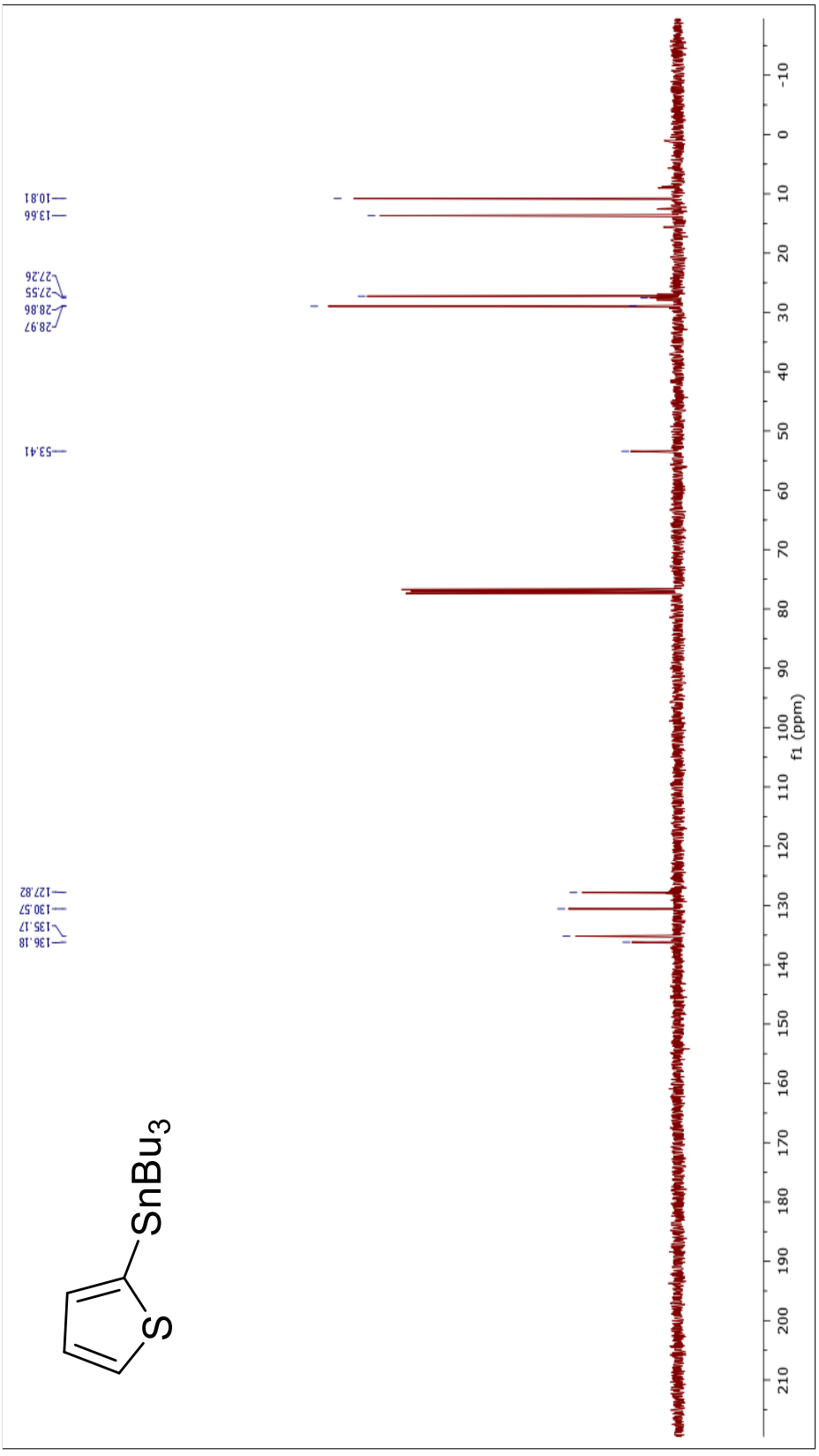

Figure A.9: ^{13}C NMR spectrum of tributyl(thiophen-2-yl)stannane.

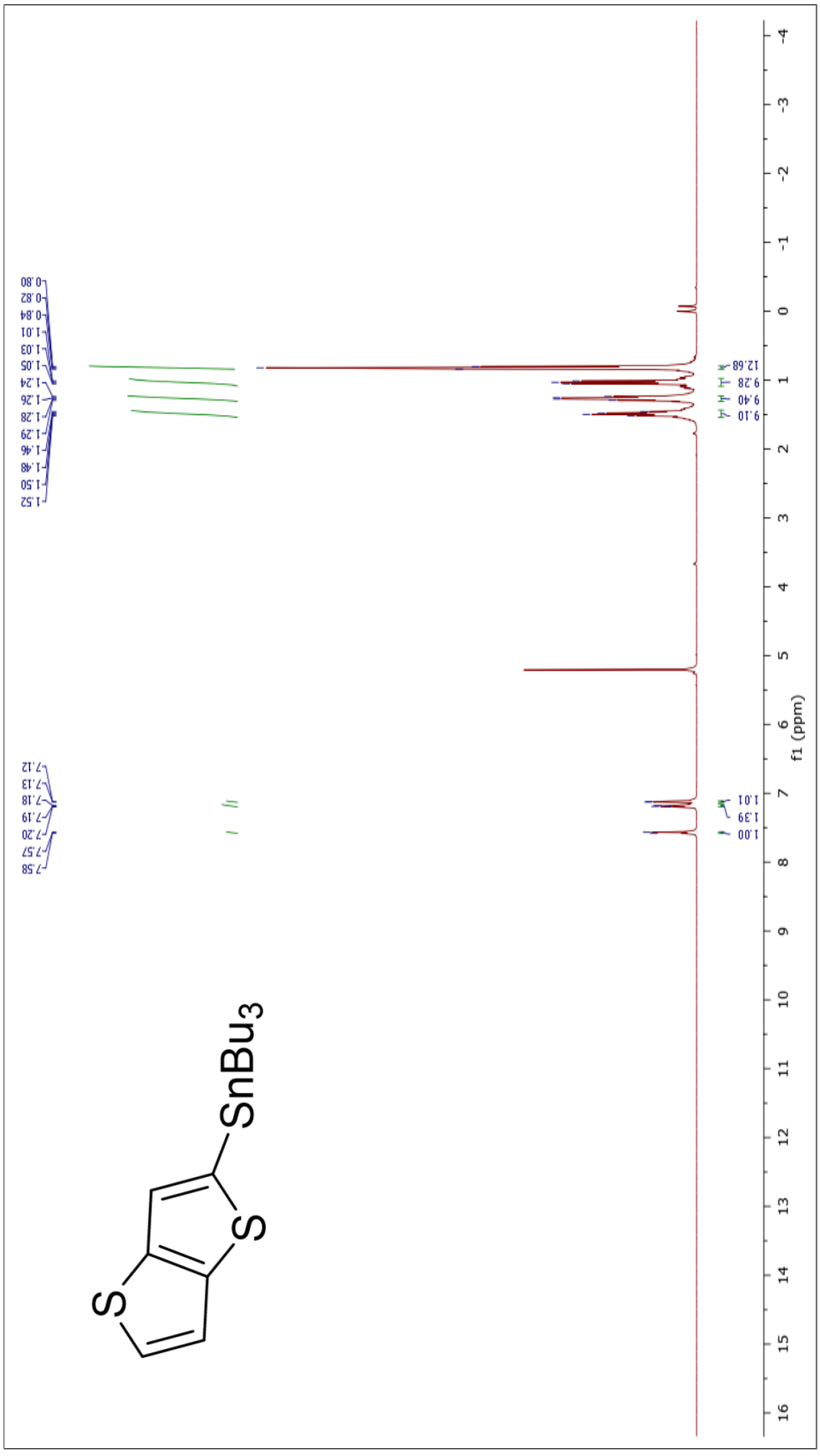

Figure A.10: ^{1}H NMR spectrum of tributyl(thieno[3,2-b]thiophen-2-yl)stannane.

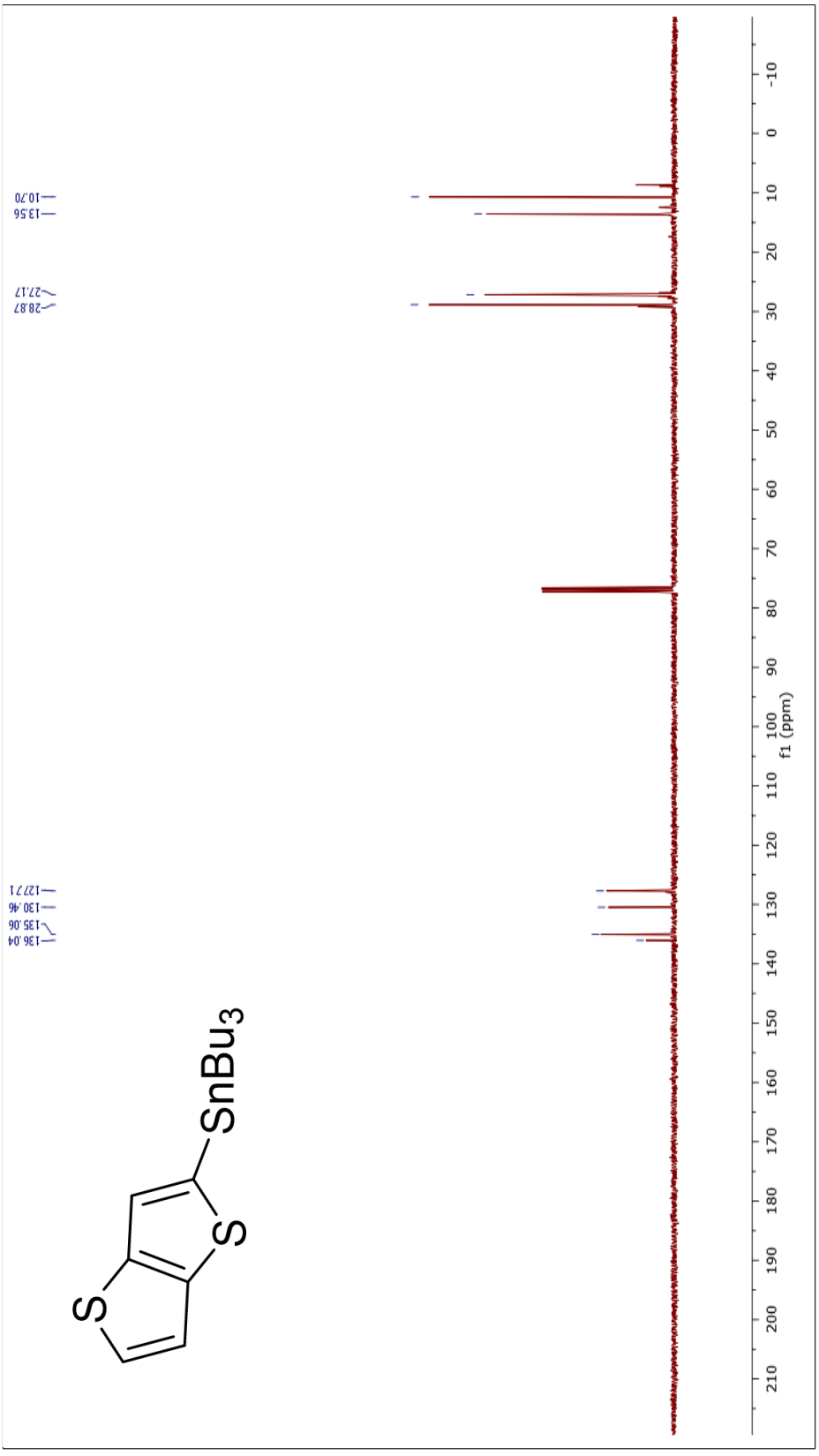

Figure A.11: ^{13}C NMR spectrum of tributyl(thieno[3,2-b]thiophen-2-yl)stannane.

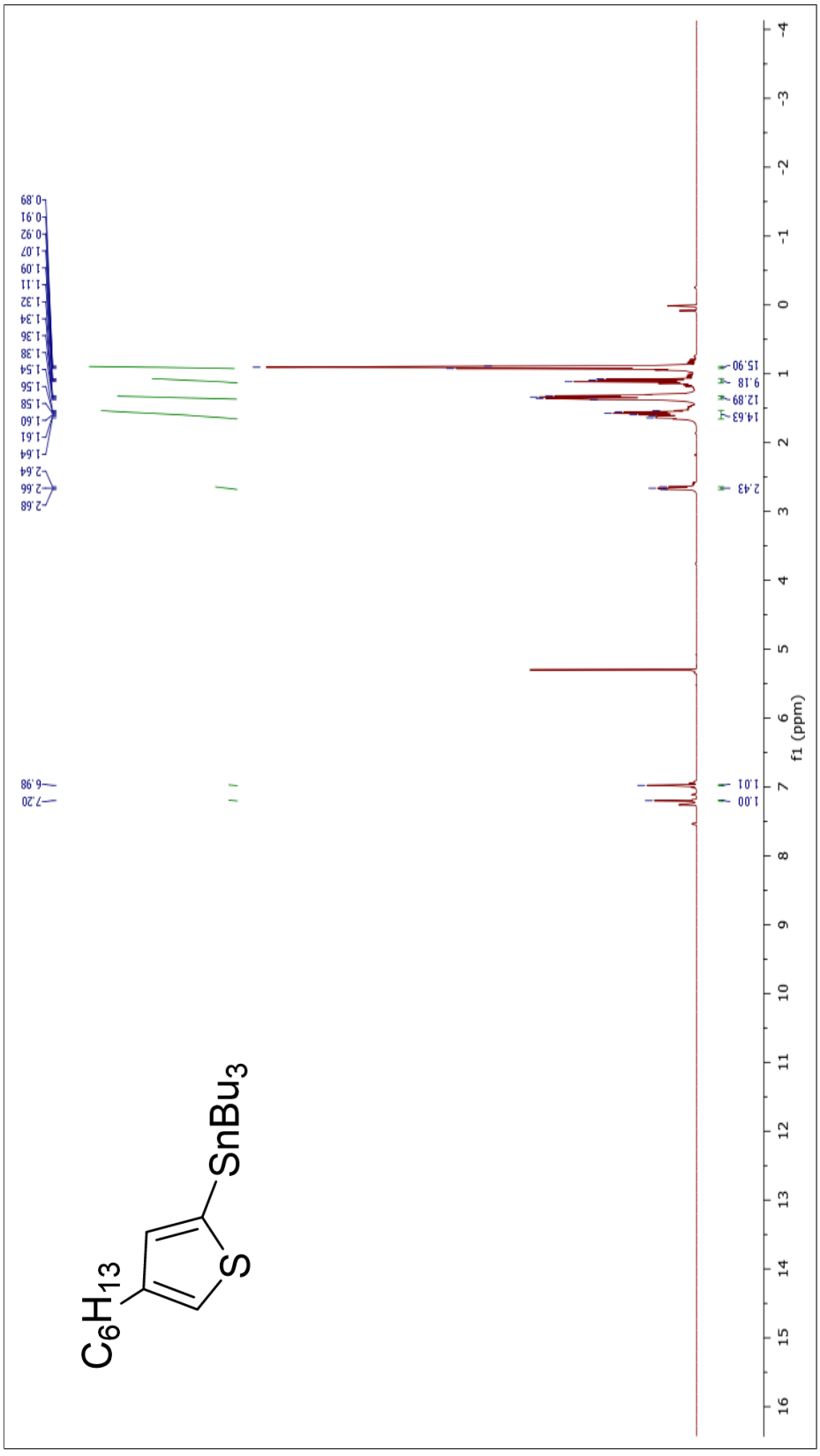

Figure A.12: ^{1}H NMR spectrum of tributyl(4-hexylthiophen-2-yl)stannane.

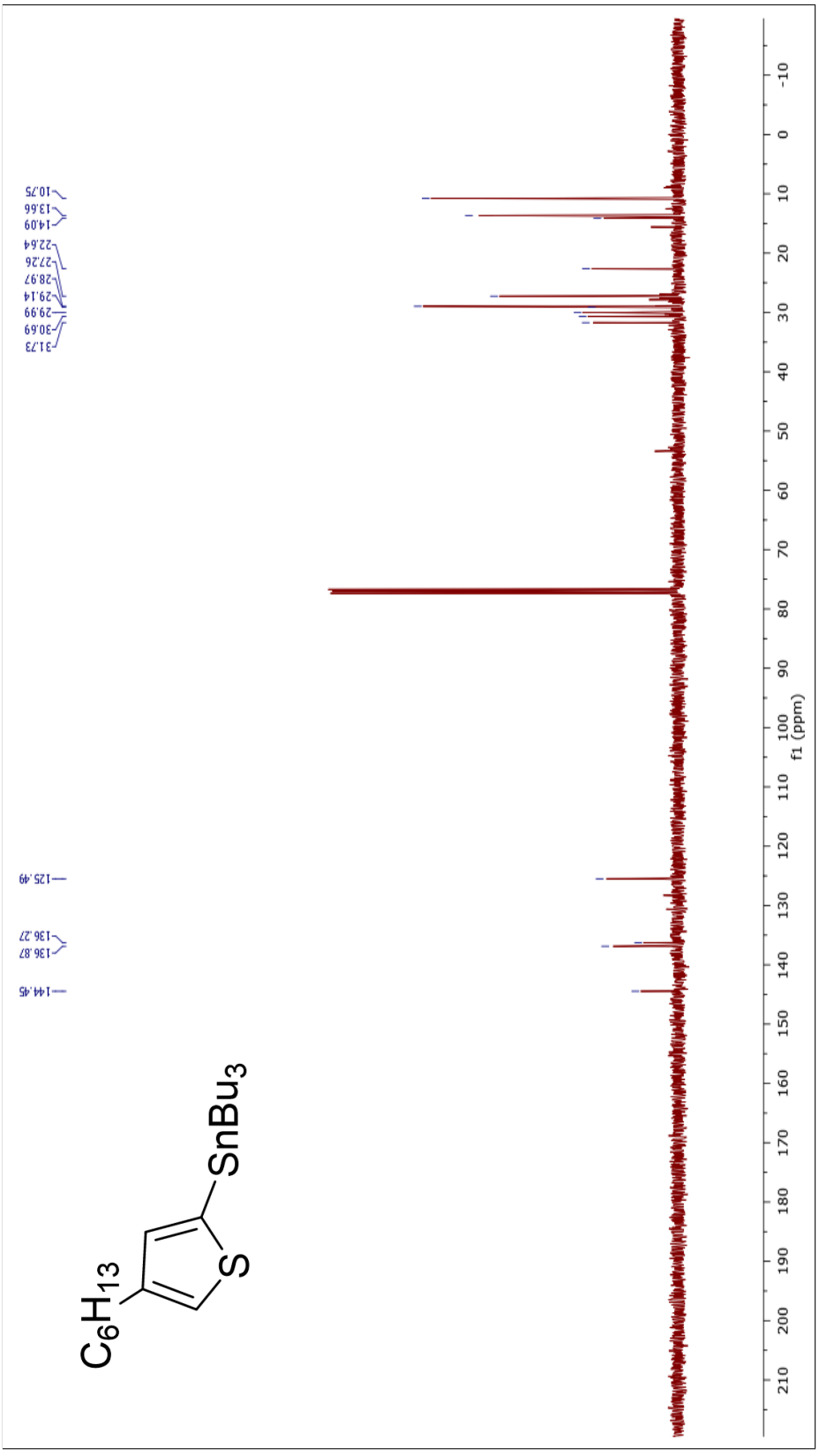

Figure A.13: ^{13}C NMR spectrum of tributyl(thiophen-2-yl)stannane.

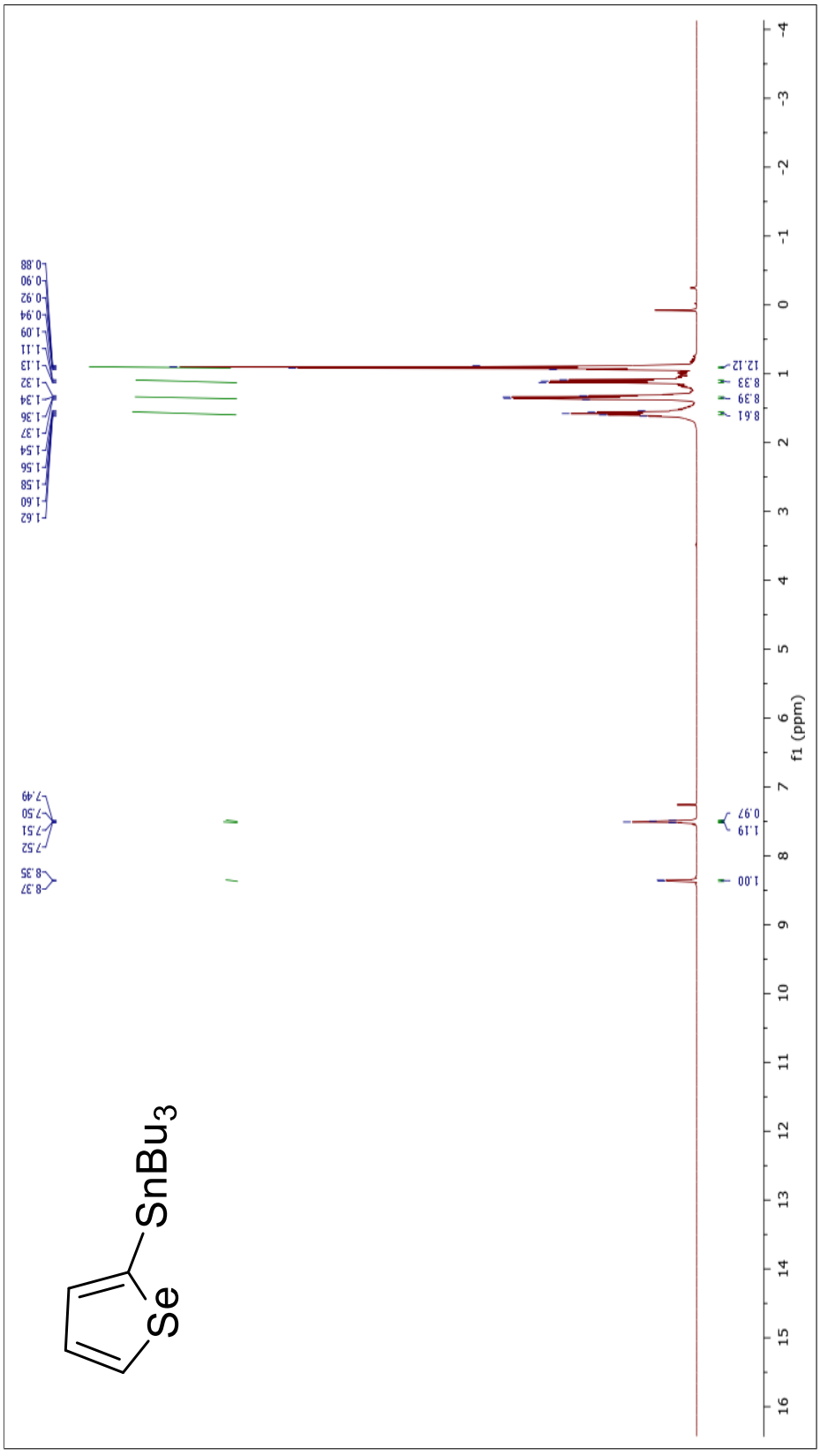

Figure A.14: ^{1}H NMR spectrum of tributyl(selenophen-2-yl)stannane.

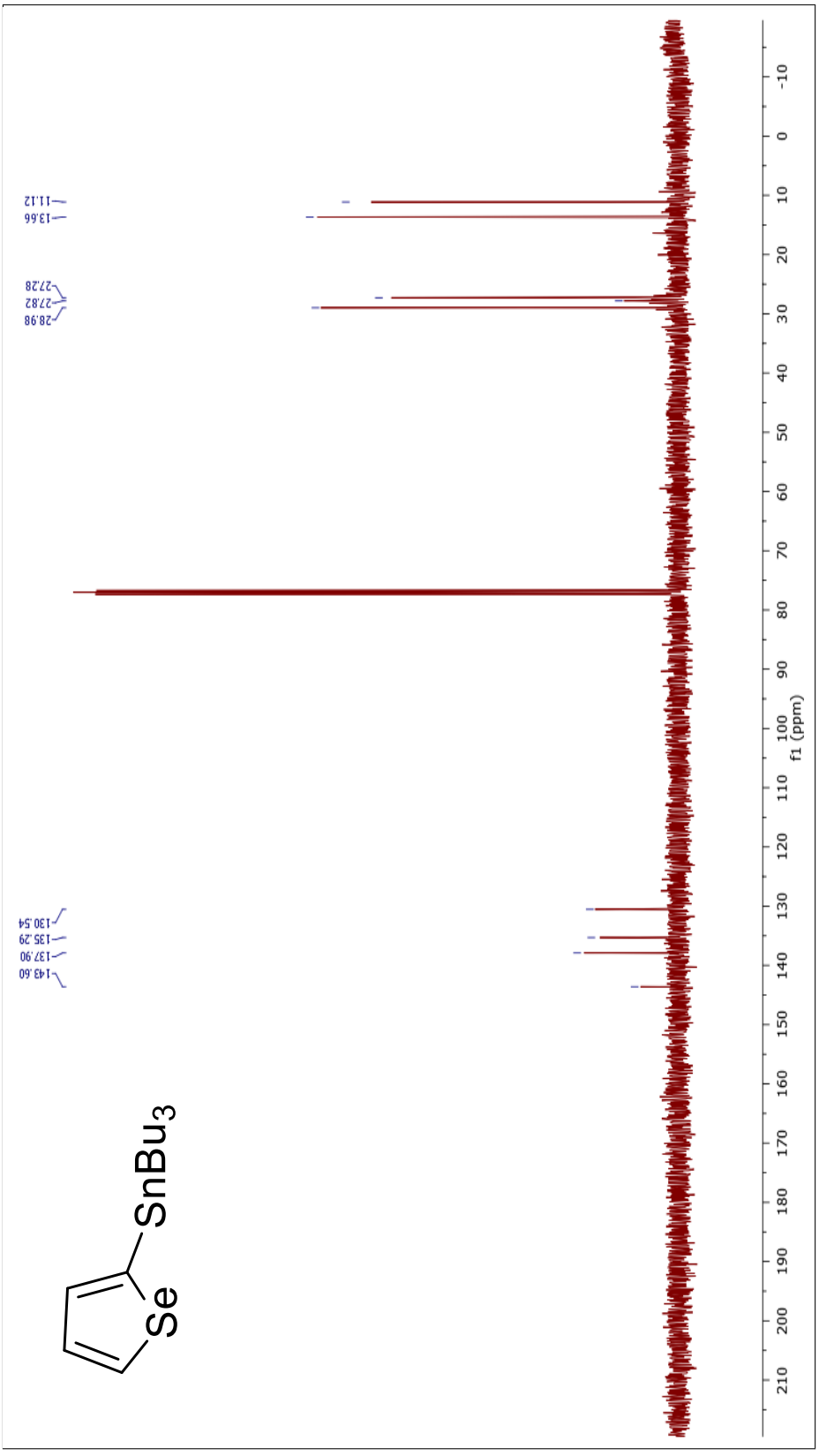

Figure A.15: ^{13}C NMR spectrum of tributyl(selenophen-2-yl)stannane.

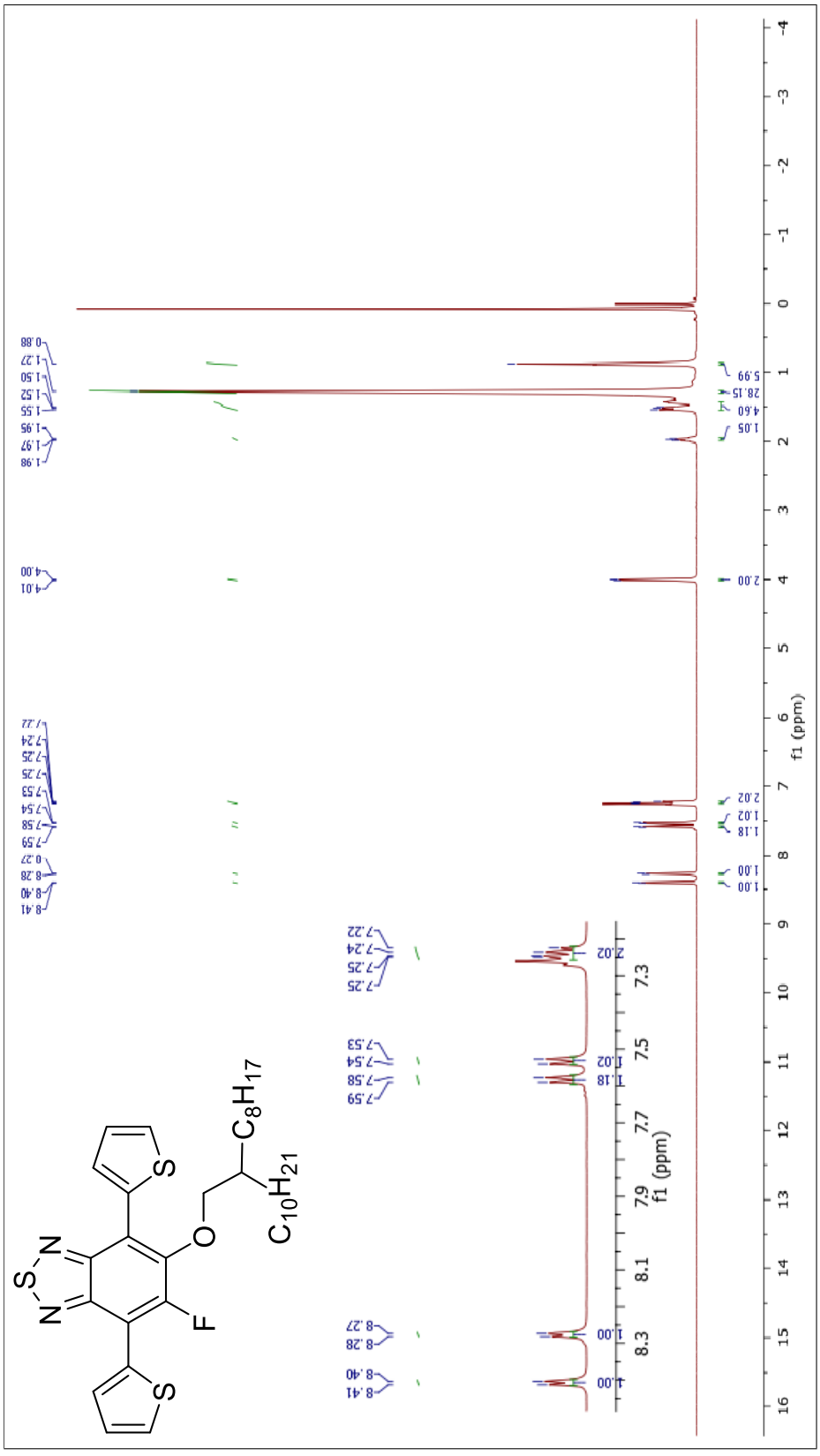

Figure A.16: ^{1}H NMR spectrum of 5-fluoro-6-((2-octyldodecyl)oxy)-4,7-di(thiophen-2-yl)benzo[c][1,2,5]thiadiazole.

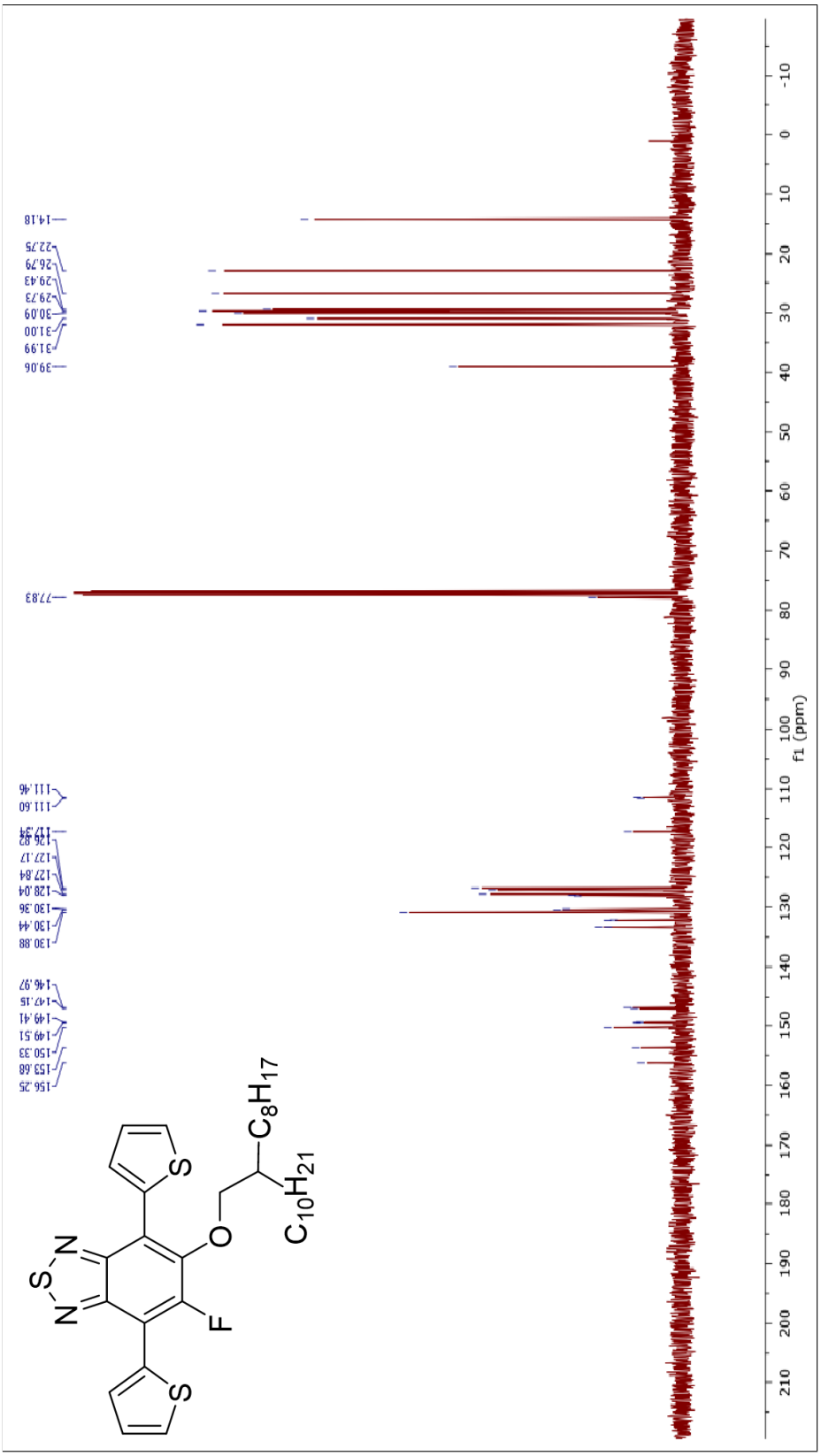

Figure A.17: ^{13}C NMR spectrum of 5-fluoro-6-((2-octyldodecyl)oxy)-4,7-di (thiophen-2-yl)benzo[c][1,2,5]thiadiazole.

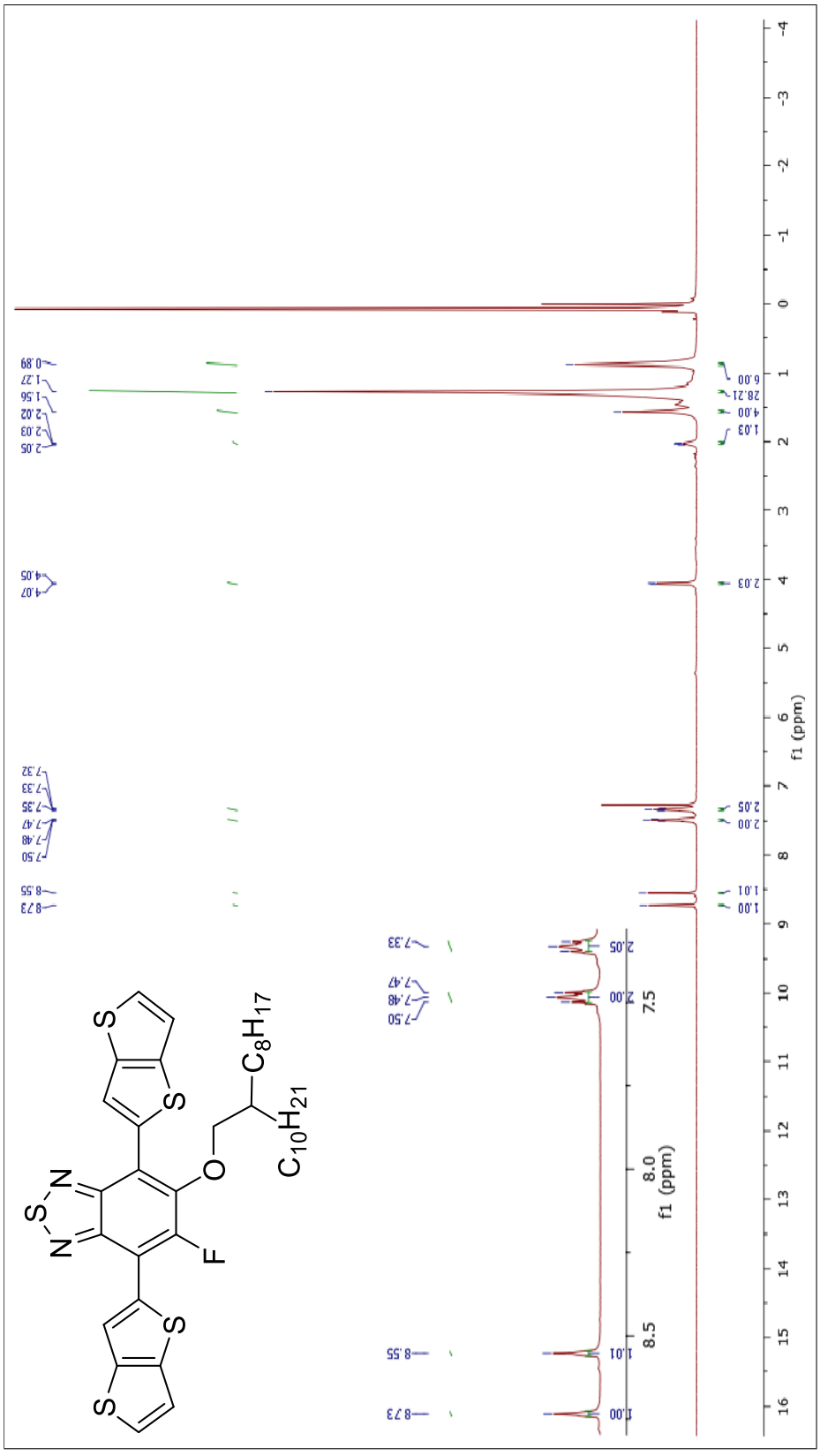

Figure A.18: ^{1}H NMR spectrum of 5-fluoro-6-((2-octyldodecyl)oxy)-4,7-bis(thieno[3,2-b]thiophen-2-yl)benzo[c][1,2,5]thiadiazole.

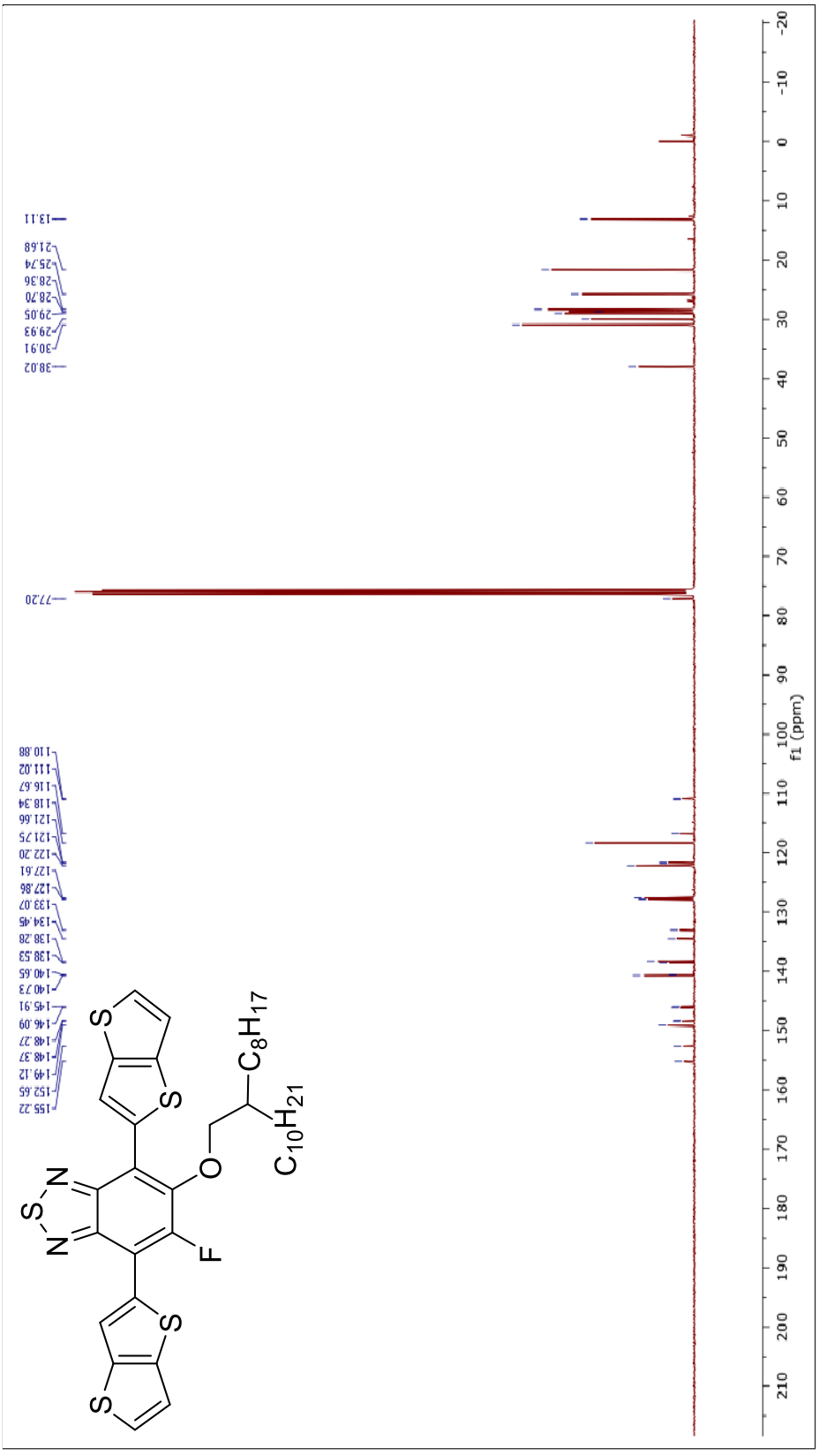

Figure A.19: ^{13}C NMR spectrum of 5-fluoro-6-((2-octyldodecyl)oxy)-4,7-bis(thieno[3,2-b]thiophen-2-yl)benzo[c][1,2,5]thiadiazole.

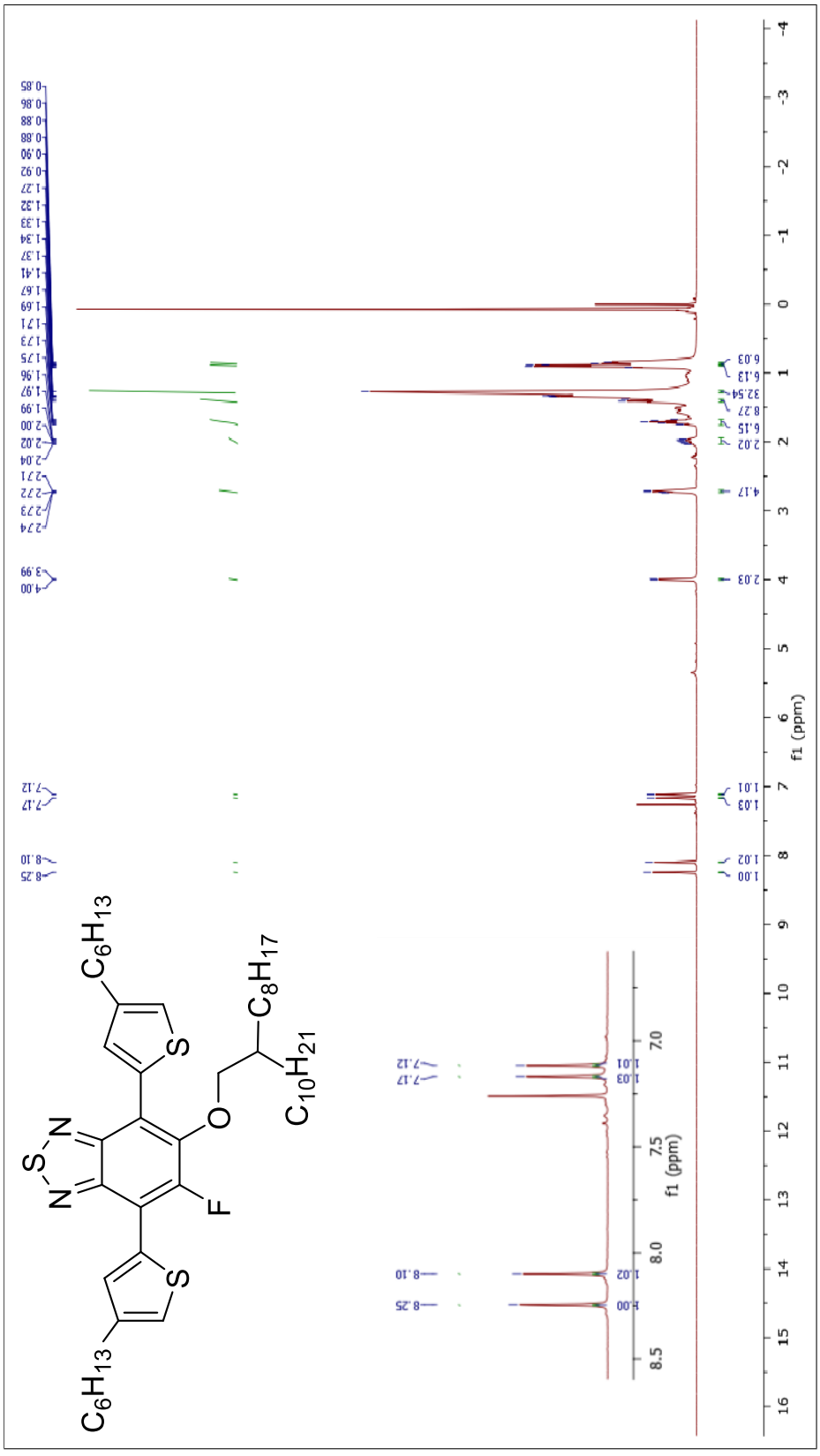

Figure A.20: ^{1}H NMR spectrum of 5-fluoro-6-((2-octyldodecyl)oxy)-4,7-bis(4-hexylthiophen-2-yl) benzo[c][1,2,5]thiadiazole.

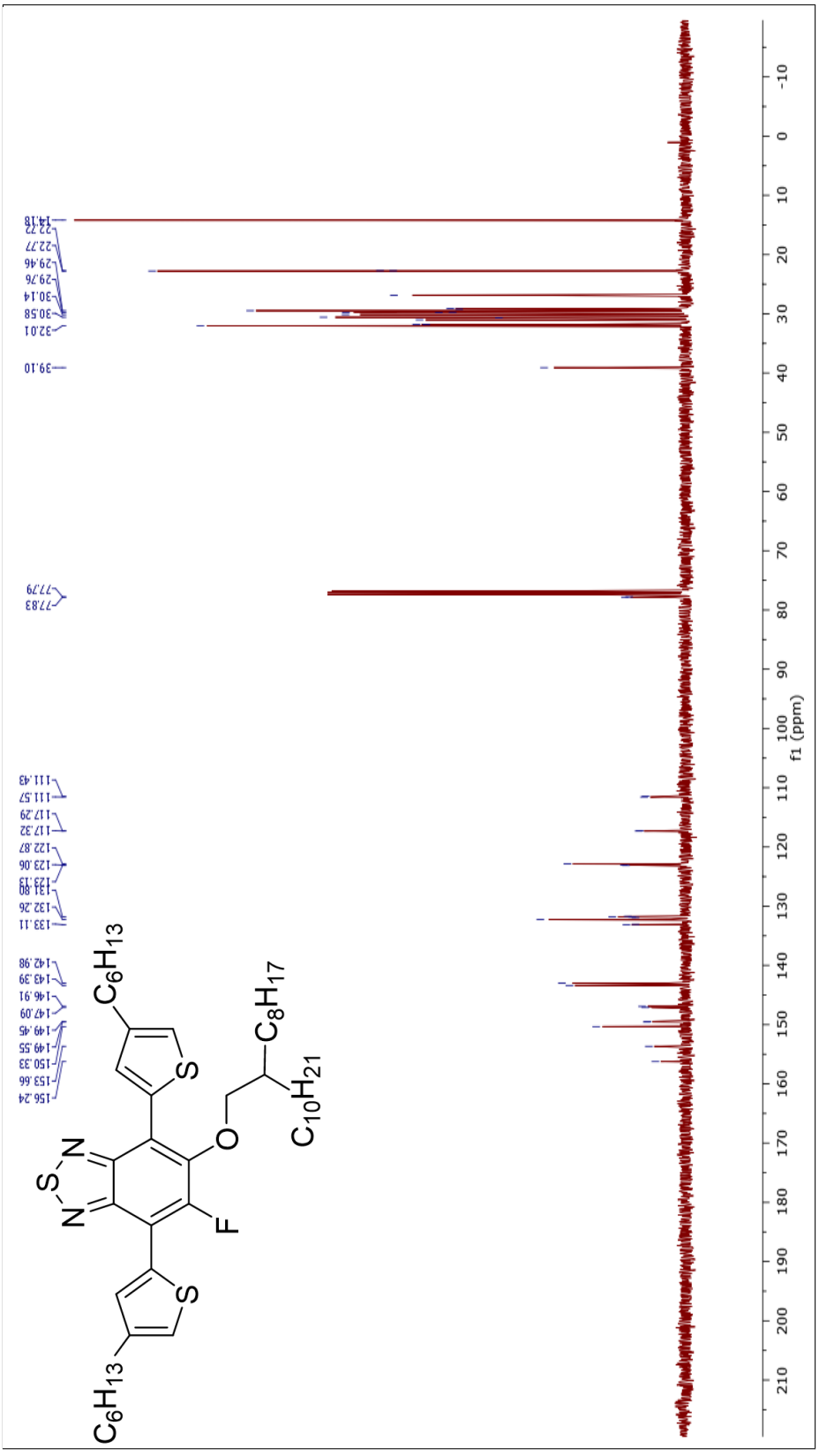

Figure A.21: ^{13}C NMR spectrum of 5-fluoro-6-((2-octyldodecyl)oxy)-4,7-bis(4-hexylthiophen-2-yl) benzo[c][1,2,5]thiadiazole.

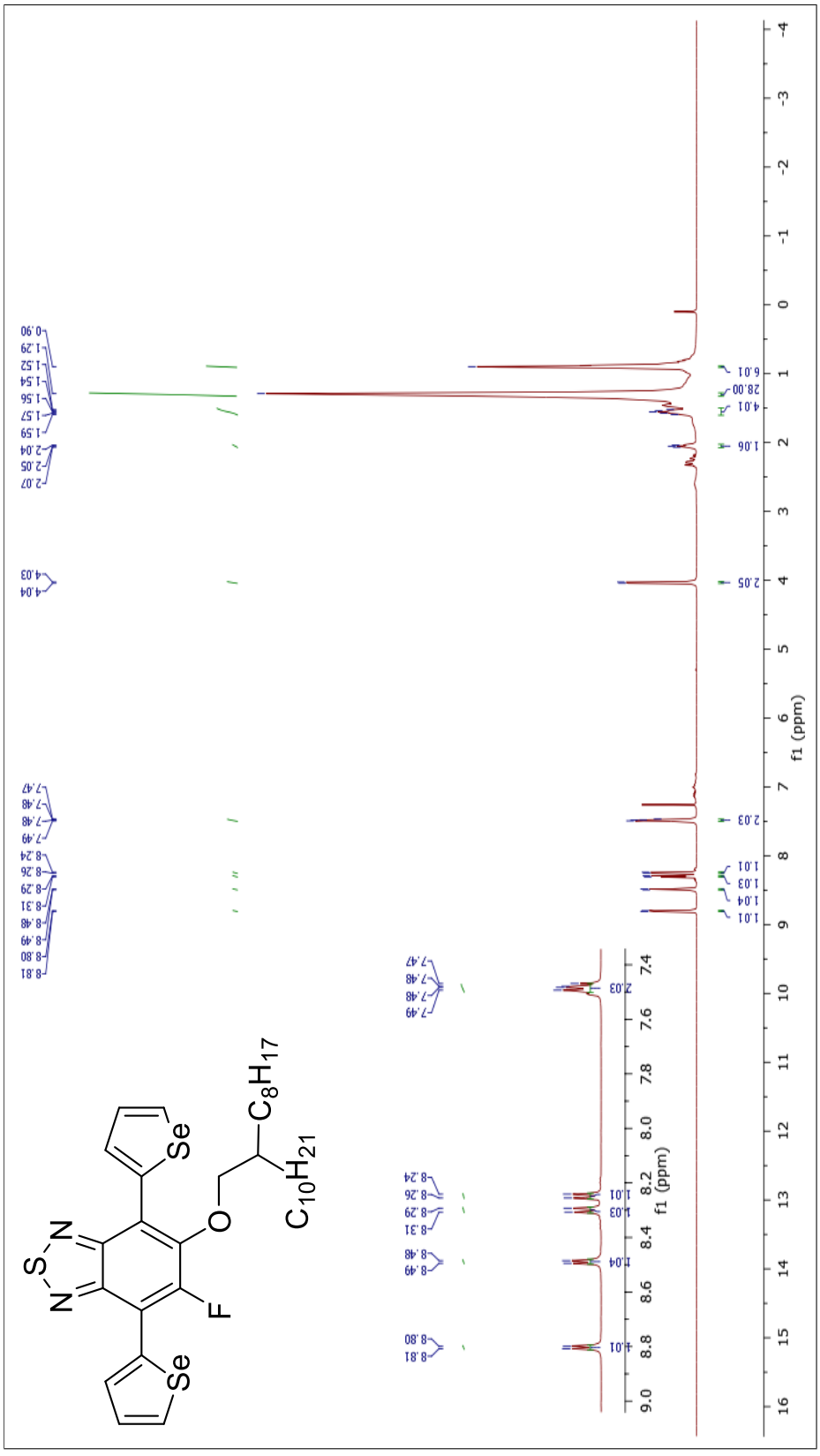

Figure A.22: ^{1}H NMR spectrum of 5-fluoro-6-((2-octyldodecyl)oxy)-4,7-di(selenophen-2-yl)benzo[c][1,2,5]thiadiazole.

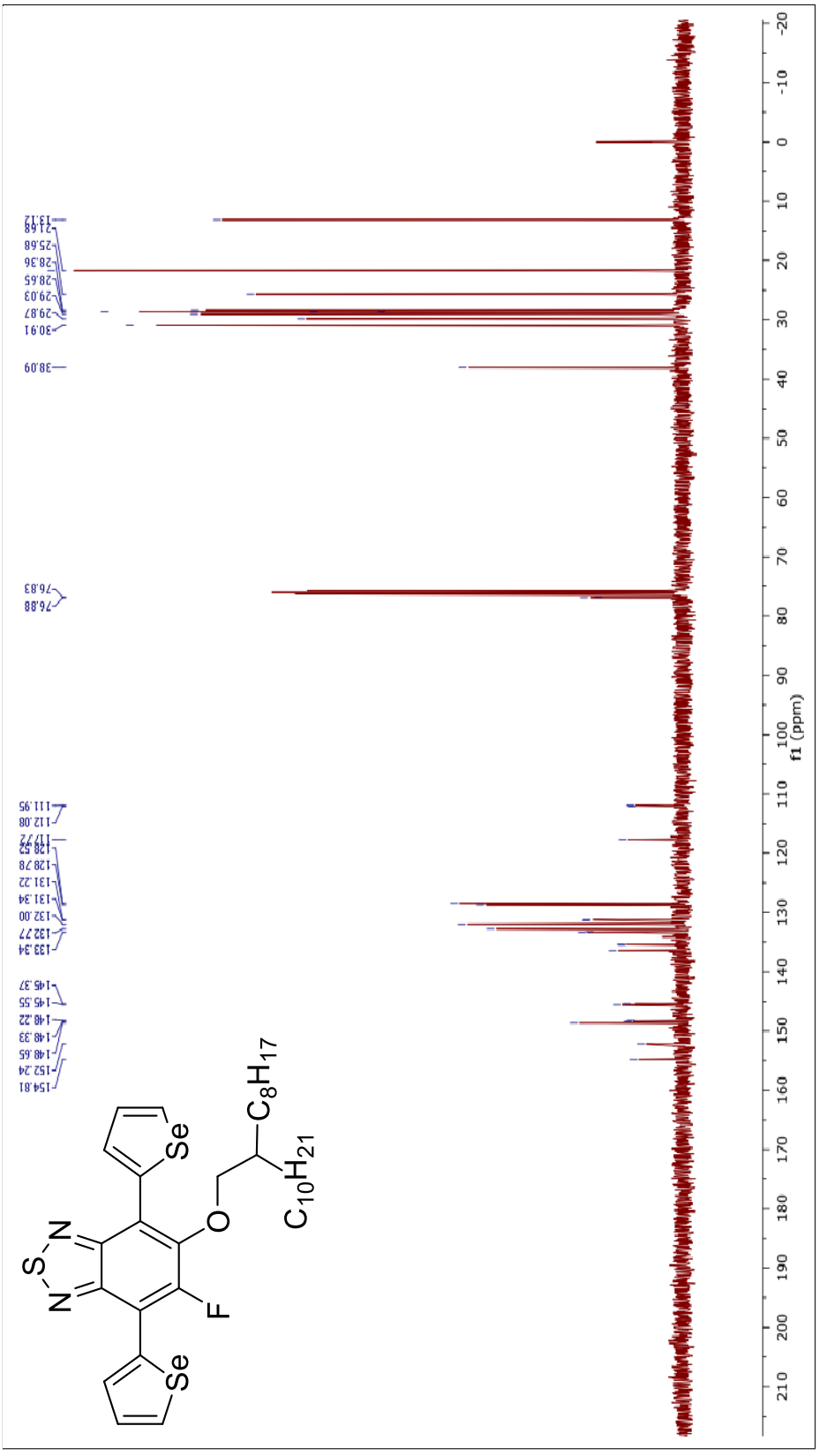

Figure A.23: ^{13}C NMR spectrum of 5-fluoro-6-((2-octyldodecyl)oxy)-4,7-di(selenophen-2-yl)benzo[c][1,2,5]thiadiazole.

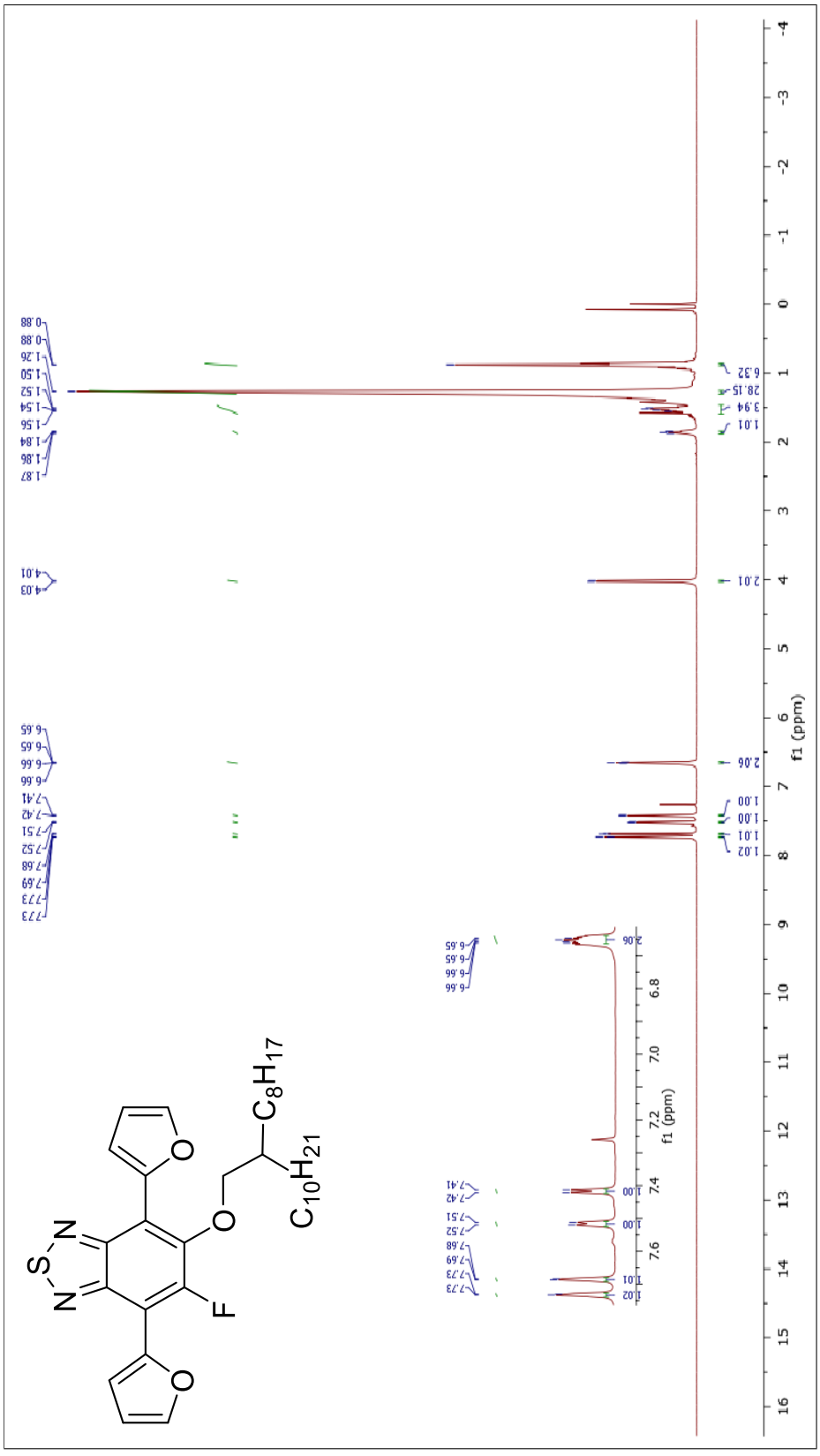

Figure A.24: ^{1}H NMR spectrum of 5-fluoro-6-((2- octyldodecyl)oxy)-4,7-di(furan-2-yl)benzo[c][1,2,5]thiadiazole.

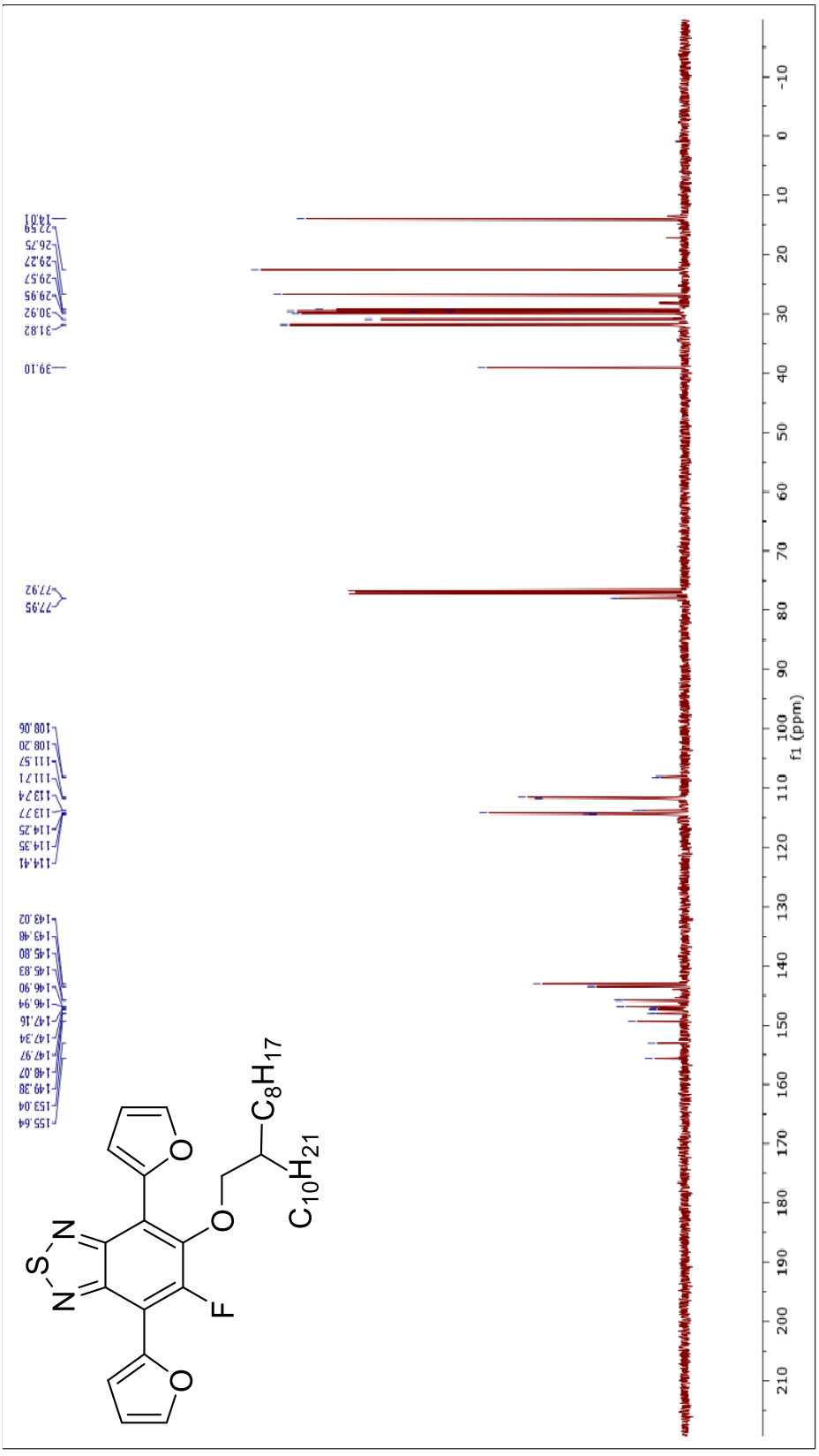

Figure A.25: ^{13}C NMR spectrum of 5-fluoro-6-((2- octyldodecyl)oxy)-4,7-di(furan-2-yl)benzo[c][1,2,5]thiadiazole.

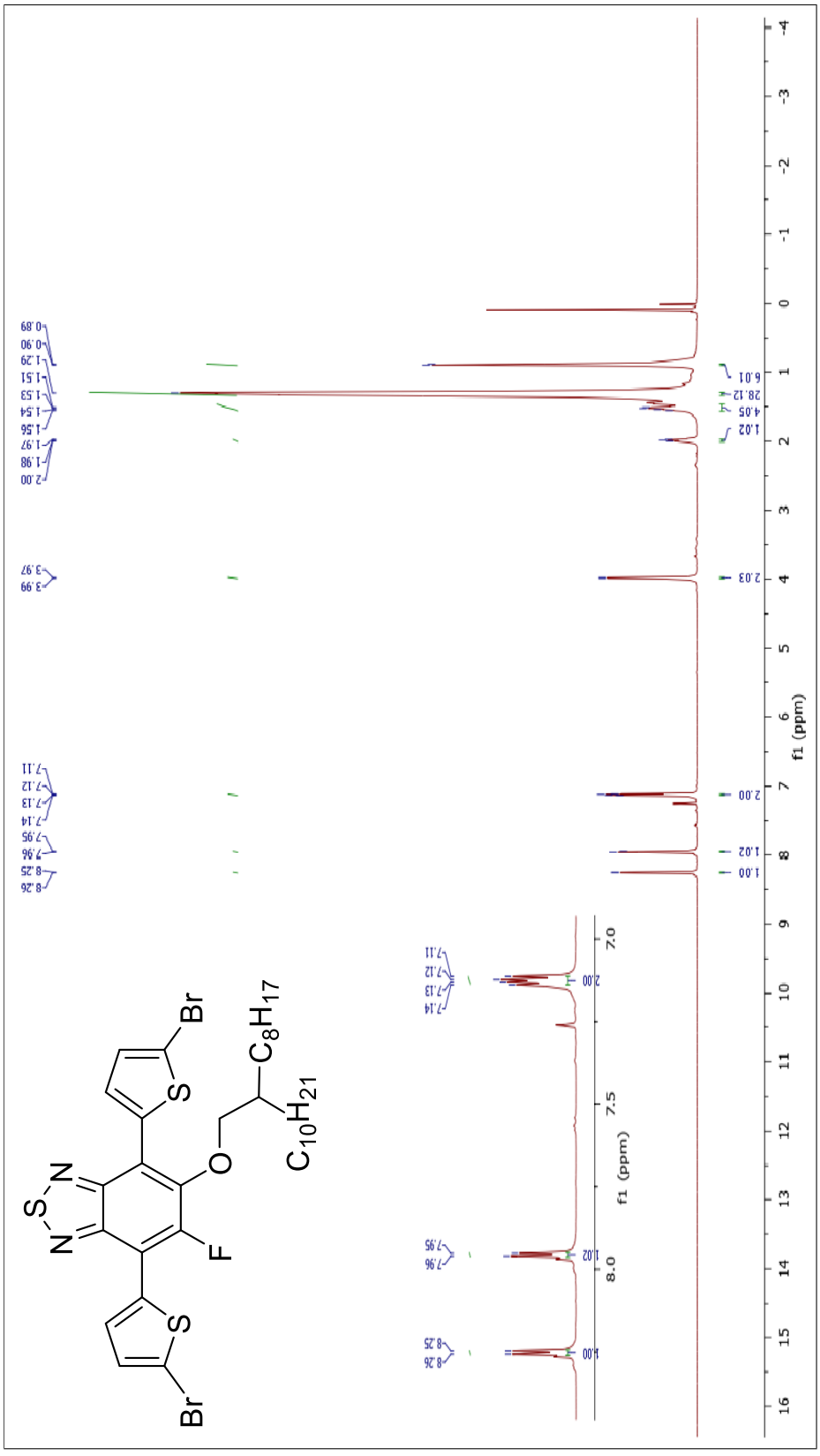

Figure A.26: ^{1}H NMR spectrum of 4,7-bis(5-bromothiophen-2-yl)-5-fluoro-6-((2-octyldodecyl)oxy)benzo[c][1,2,5]thiadiazole.

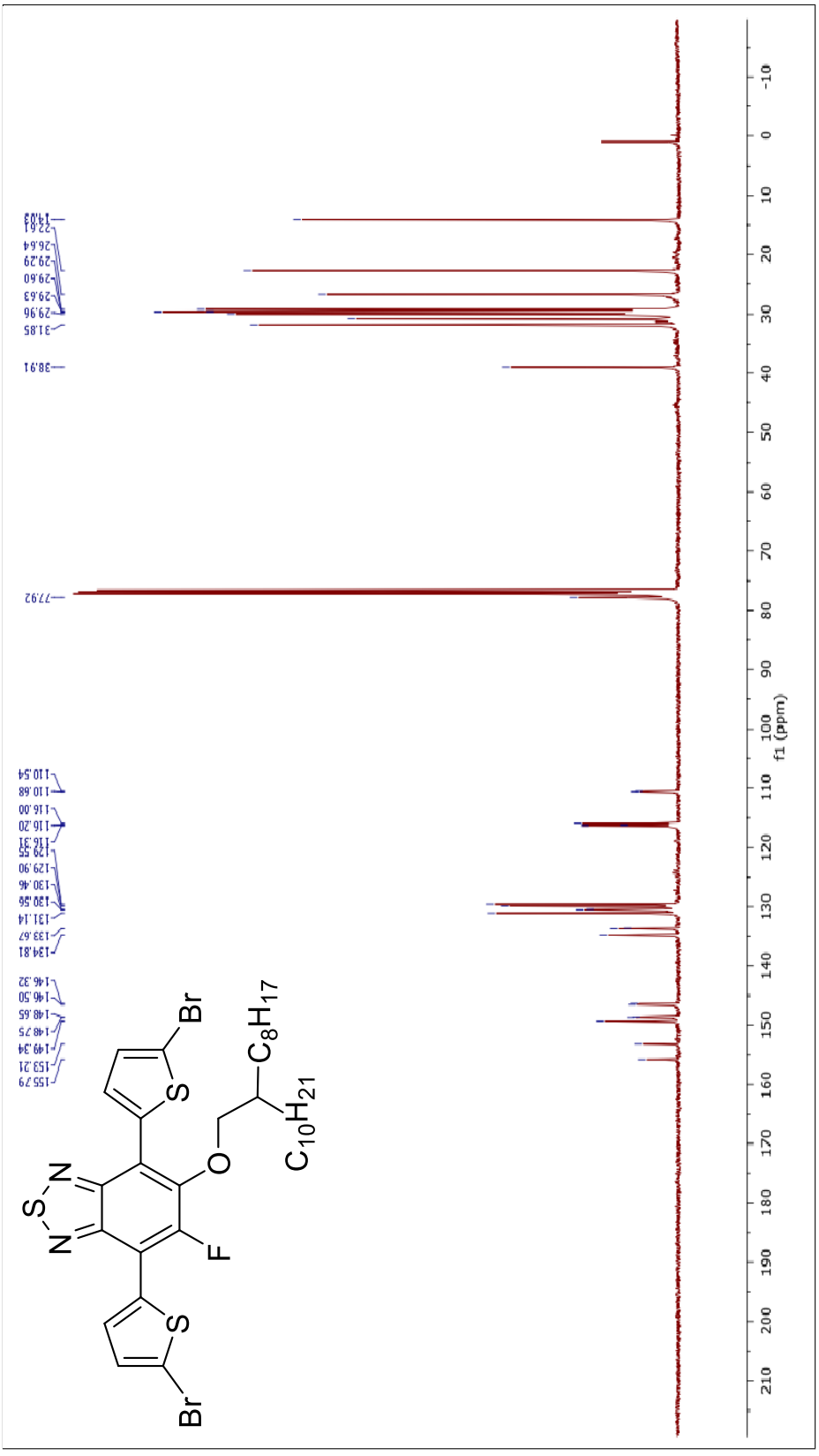

Figure A.27: ^{13}C NMR spectrum of 4,7-bis(5-bromothiophen-2-yl)-5-fluoro-6-((2-octyldodecyl)oxy)benzo[c][1,2,5]thiadiazole.

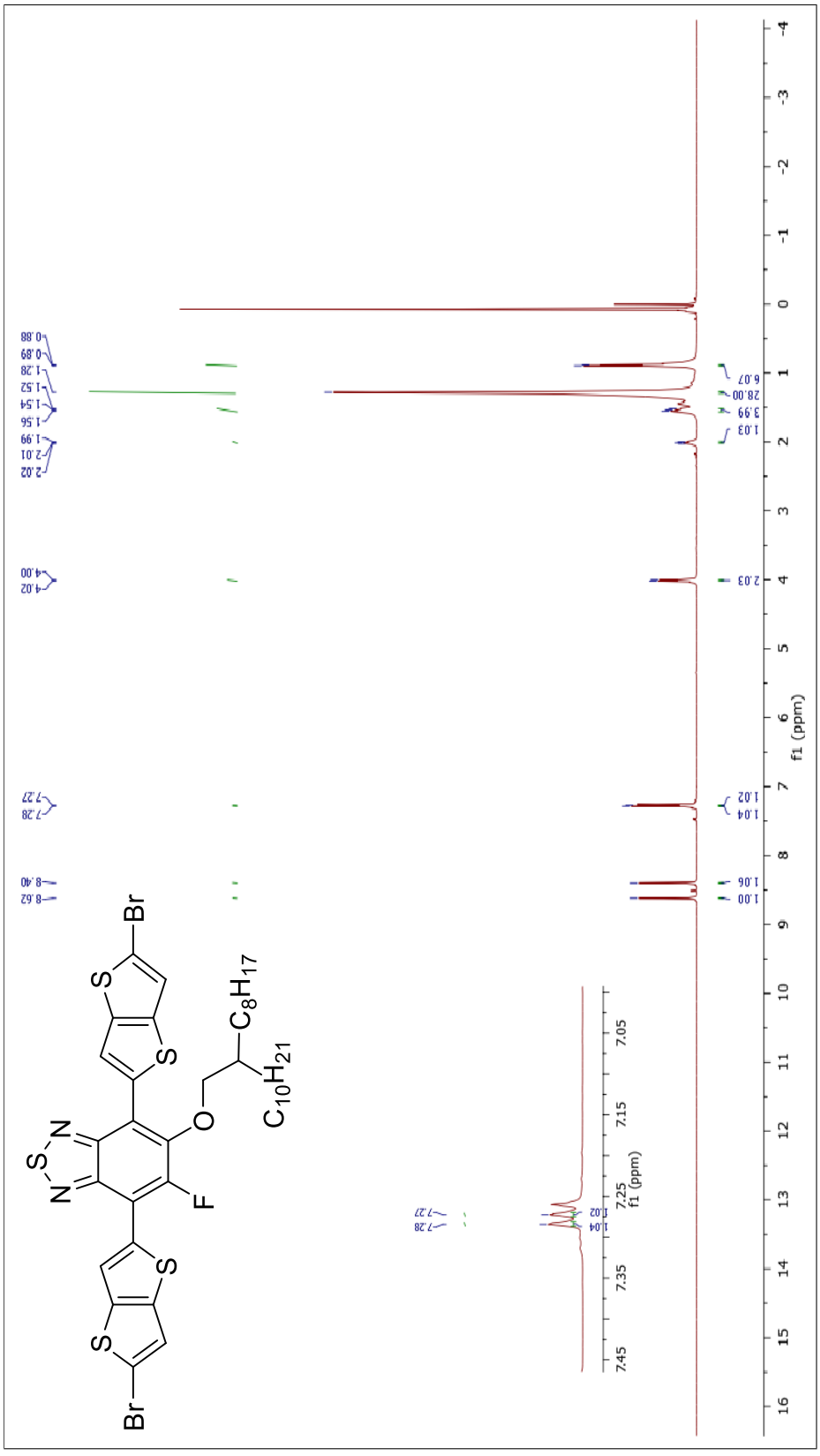

Figure A.28: ^{1}H NMR spectrum of 4,7-bis(5-bromothieno[3,2-b]thiophen-2-yl)-5-fluoro-6-((2-octyldodecyl)oxy)benzo[c][1,2,5]thiadiazole.

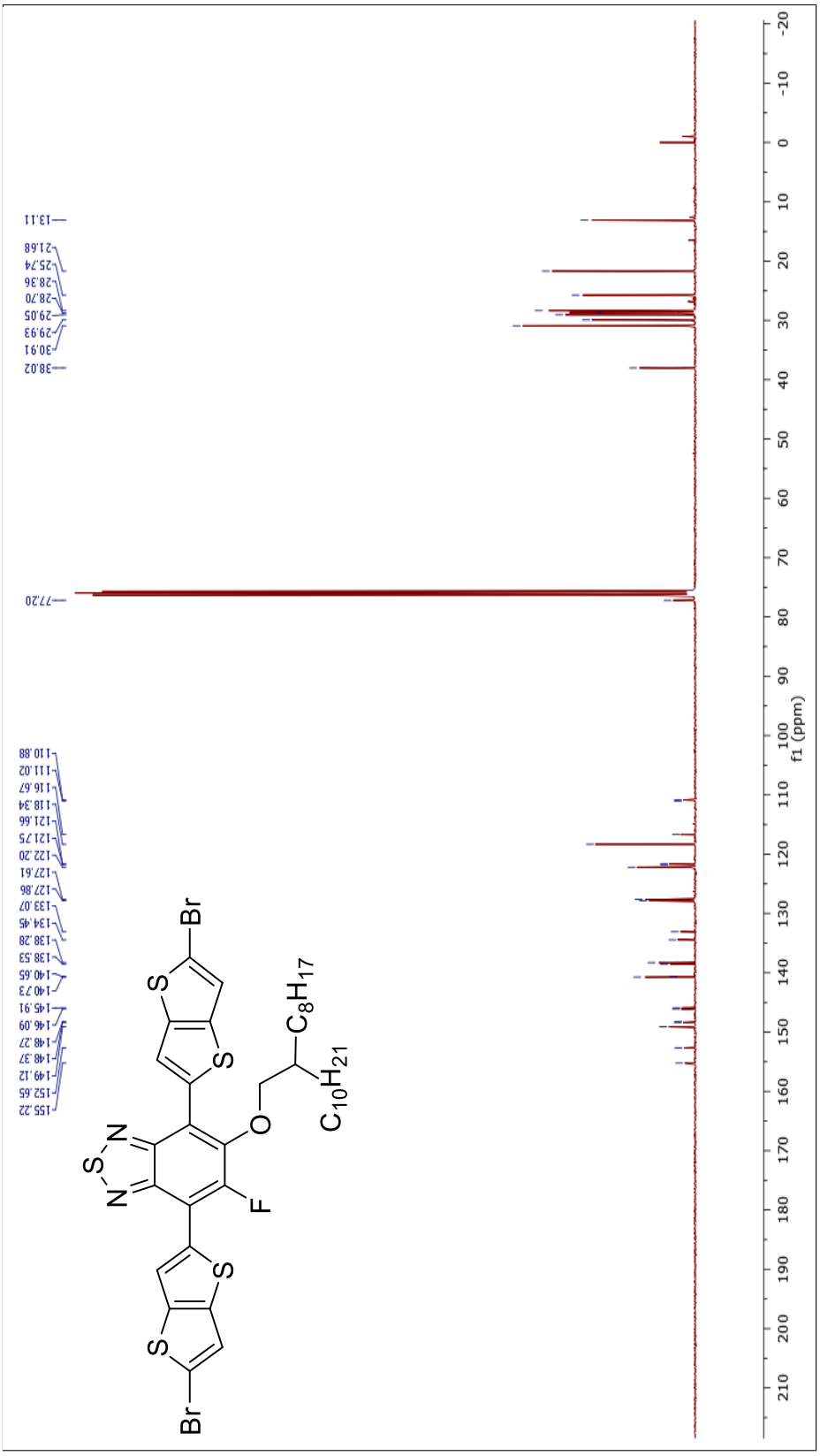

Figure A.29: ^{13}C NMR spectrum of 4,7-bis(5-bromothieno[3,2-b]thiophen-2-yl)-5-fluoro-6-((2-octyldodecyl)oxy)benzo[c][1,2,5]thiadiazole.

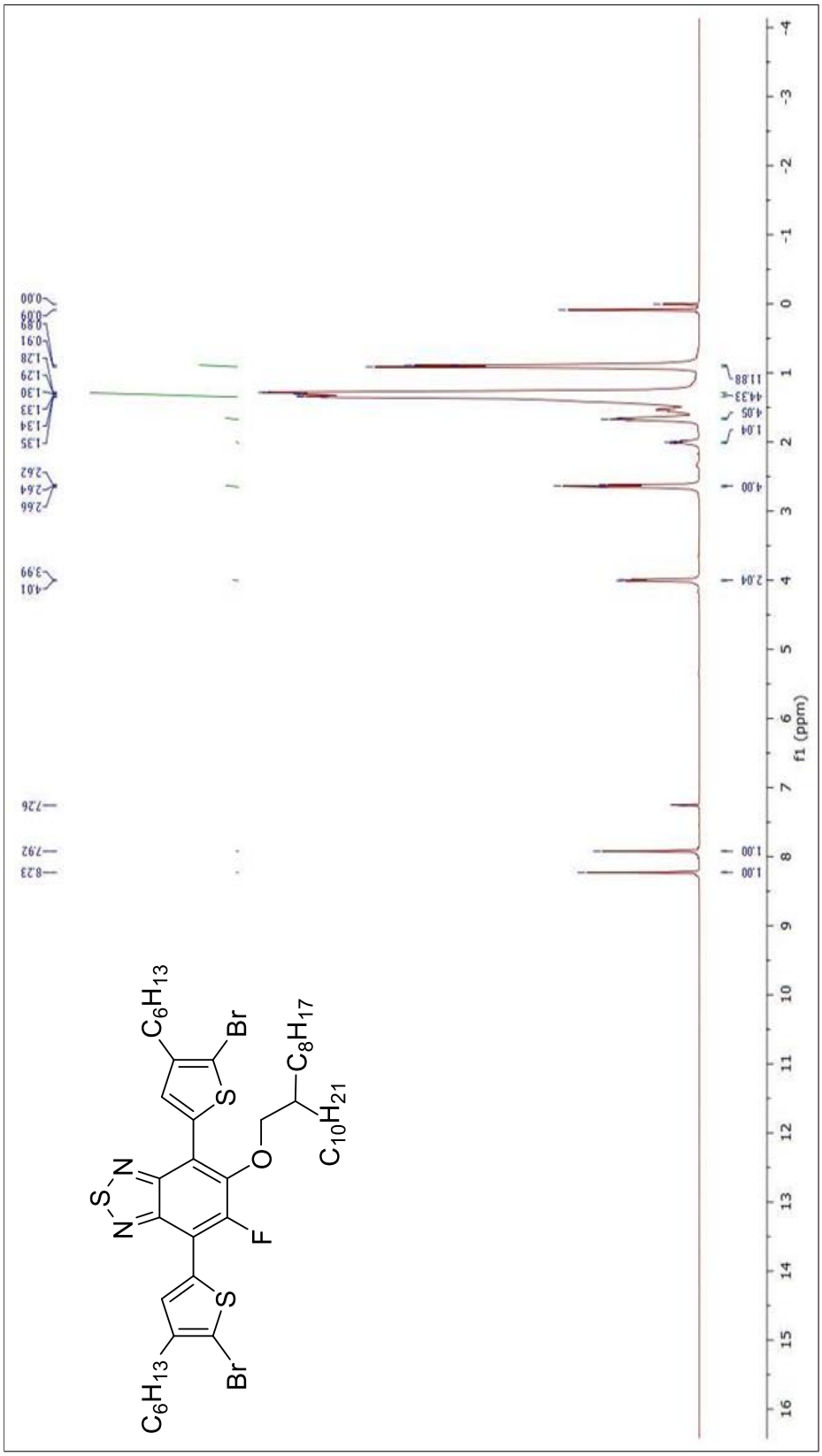

Figure A.30: ^{1}H NMR spectrum of 4,7-bis(5-bromo-4-hexylthiophen-2-yl)-5-fluoro-6-((2-octyldodecyl)oxy)benzo[c][1,2,5]thiadiazole.

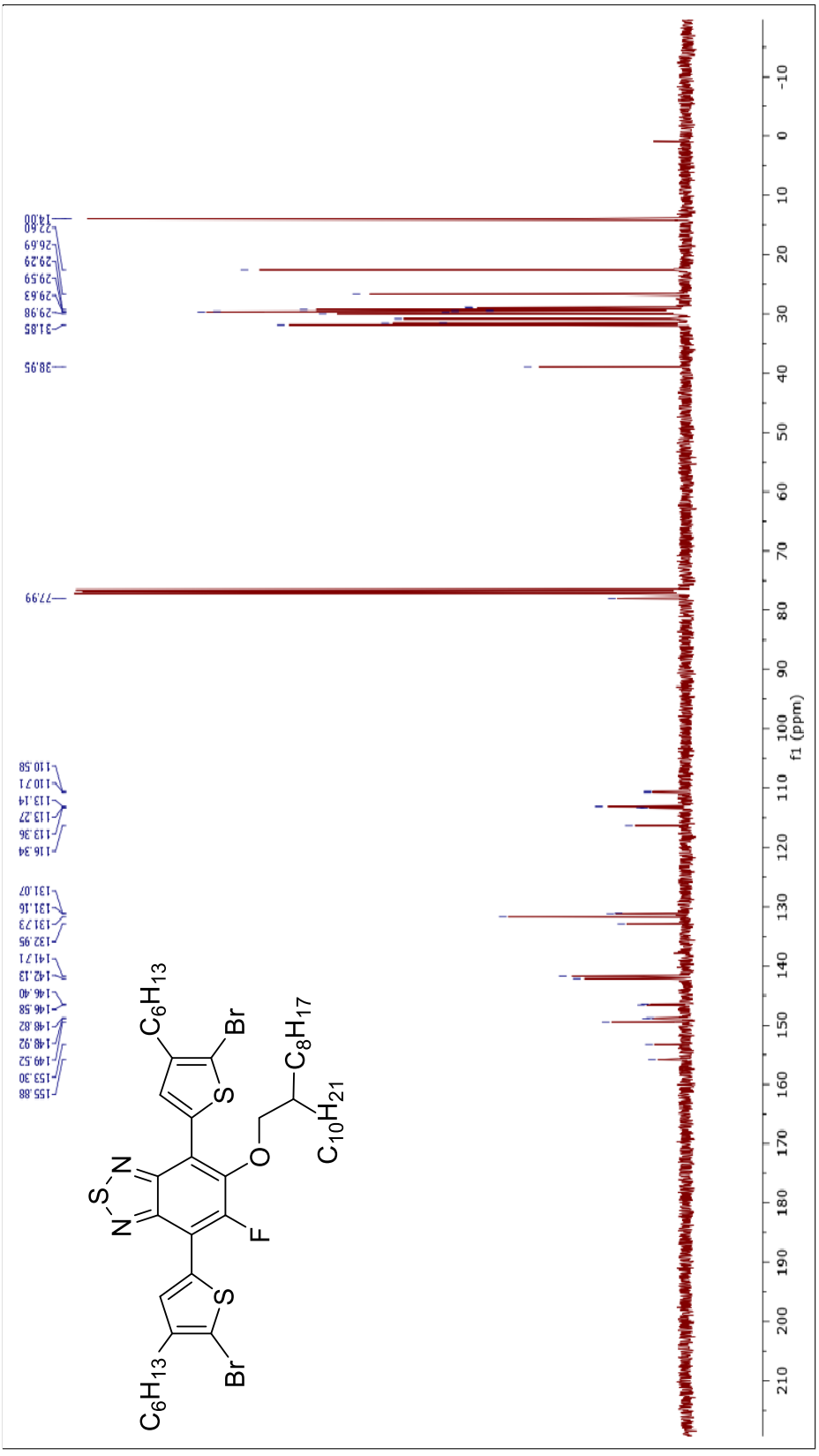

Figure A.31: ^{13}C NMR spectrum of 4,7-bis(5-bromo-4-hexylthiophen-2-yl)-5-fluoro-6-((2-octyldodecyl)oxy)benzo[c][1,2,5]thiadiazole.

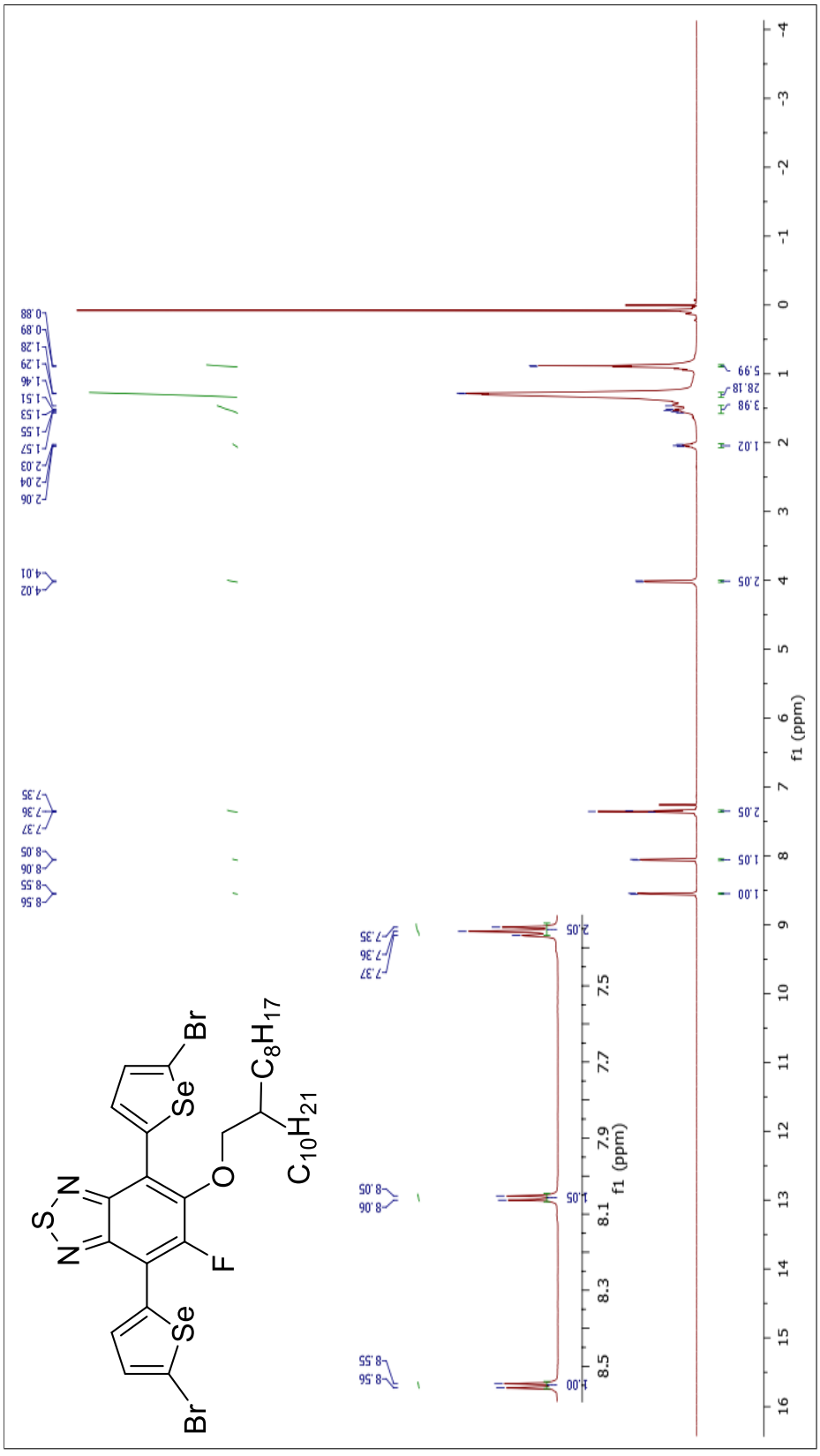

Figure A.32: ^{1}H NMR spectrum of 4,7-bis(5-bromoselenophen-2-yl)-5-fluoro-6-((2-octyldodecyl)oxy)benzo[c][1,2,5]thiadiazole.

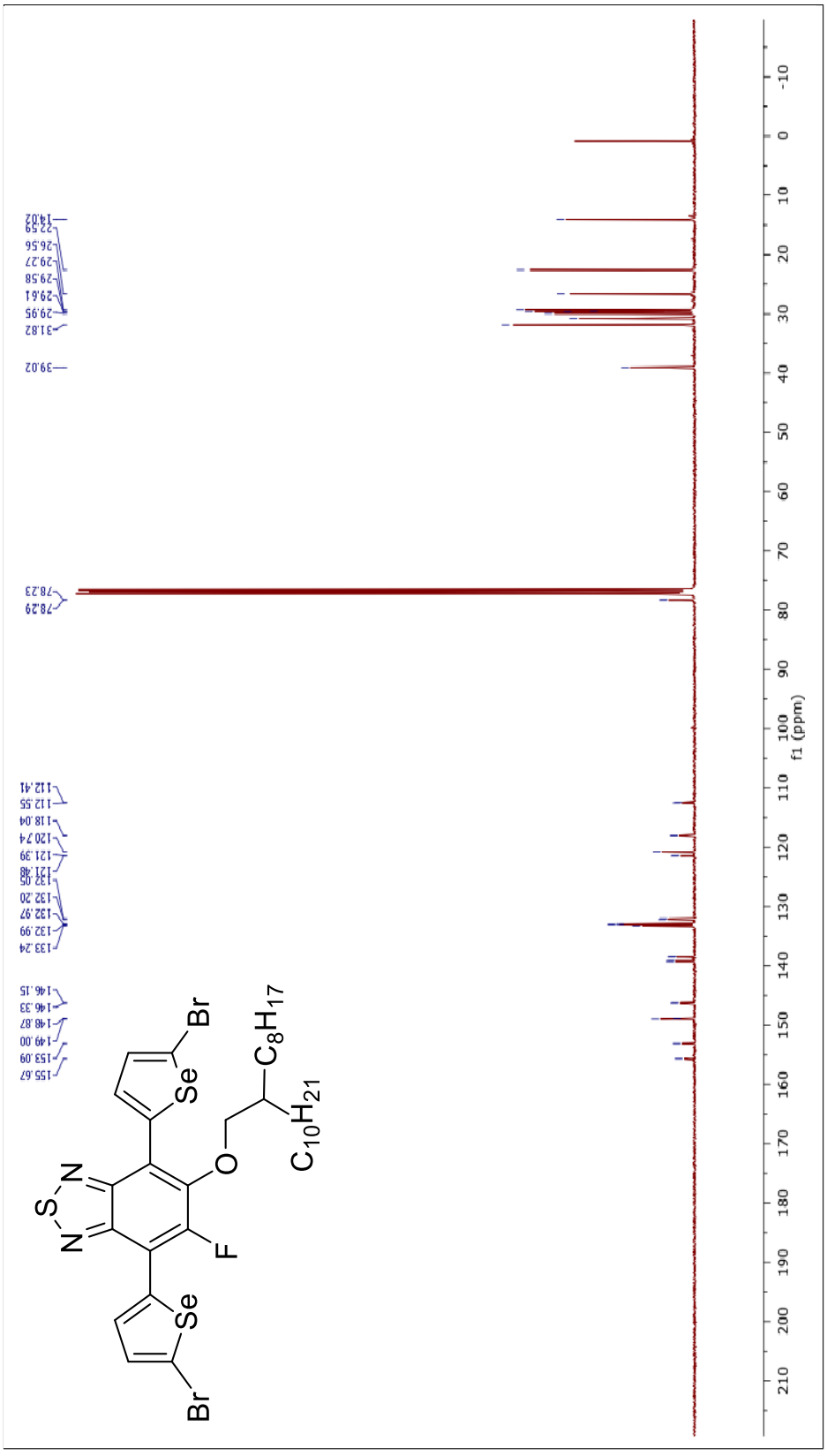

Figure A.33: ^{13}C NMR spectrum of 4,7-bis(5-bromoselenophen-2-yl)-5-fluoro-6-((2-octyldodecyl)oxy)benzo[c][1,2,5]thiadiazole.

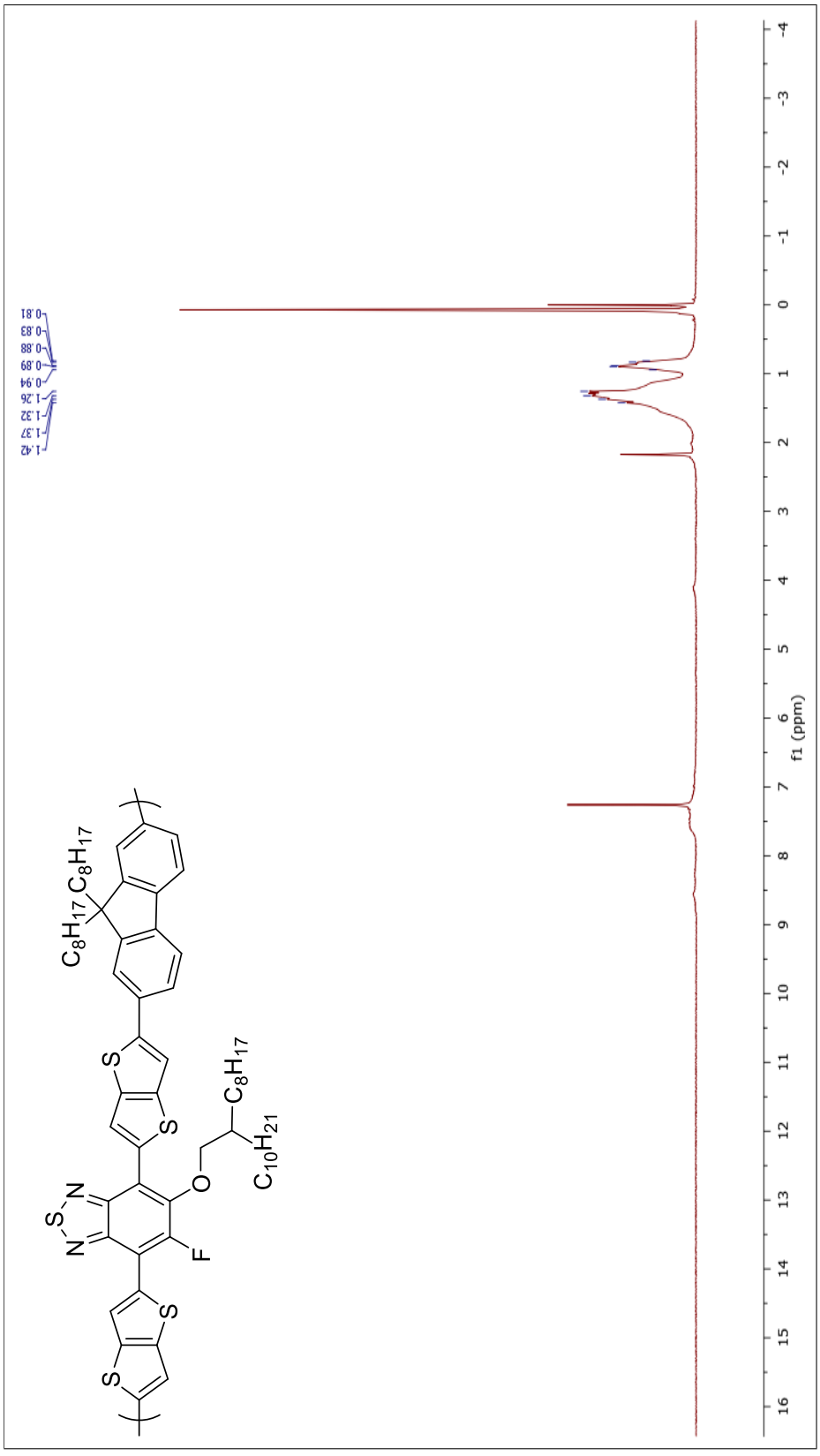

Figure A.34: ^{1}H NMR spectrum of P1.

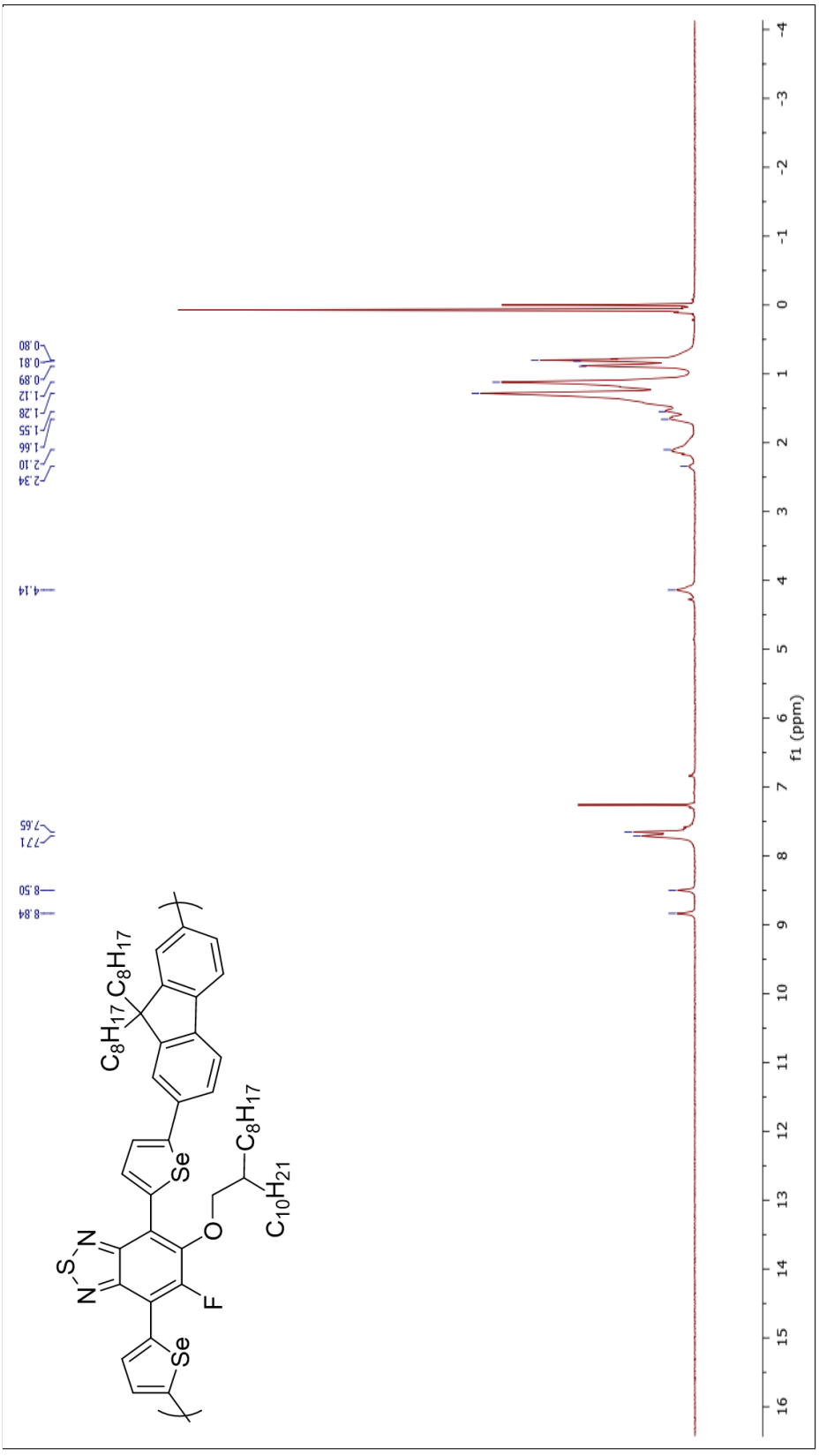

Figure A.35: ^{1}H NMR spectrum of P2.

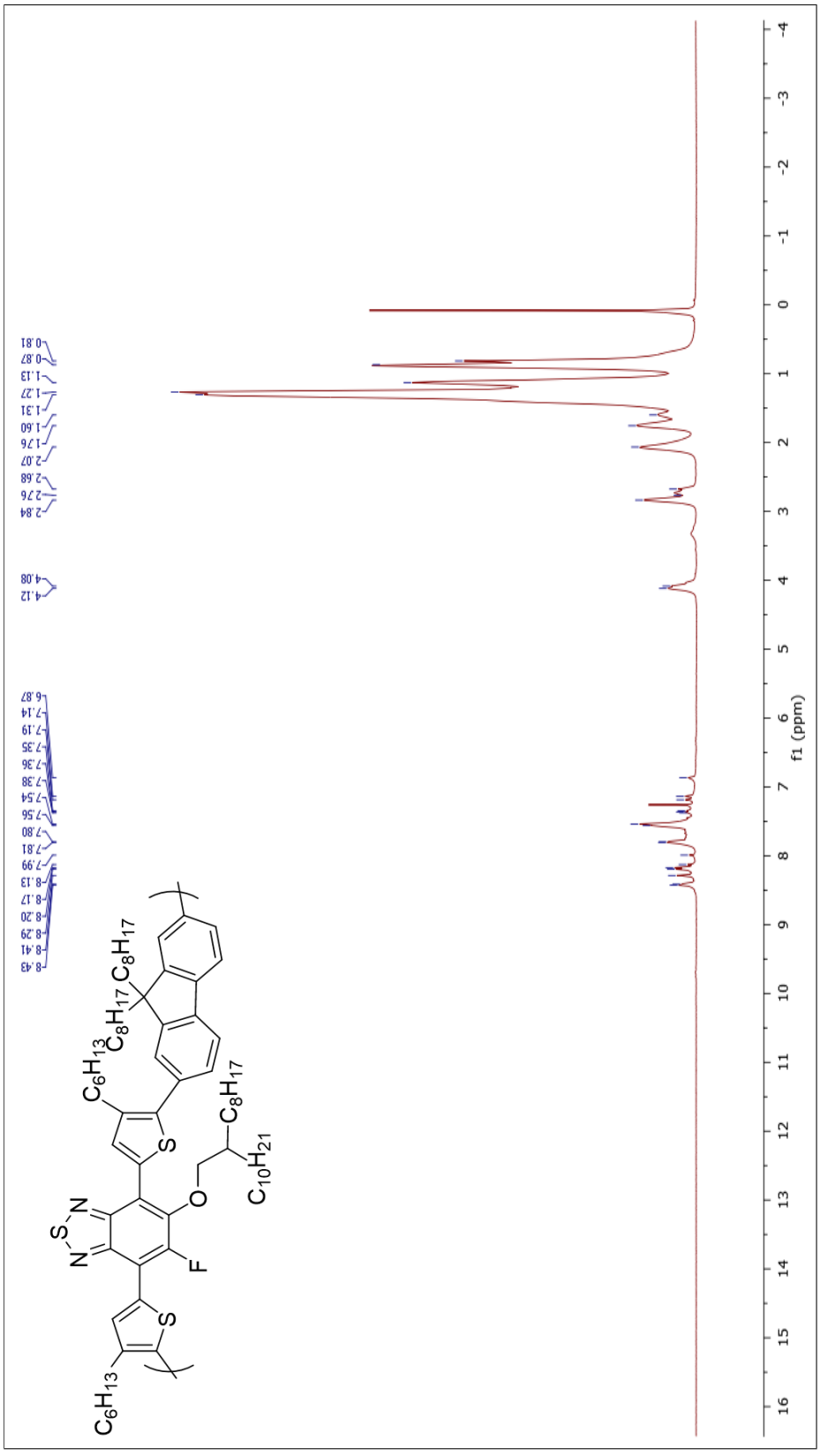

Figure A.36: ^{1}H NMR spectrum of P3.

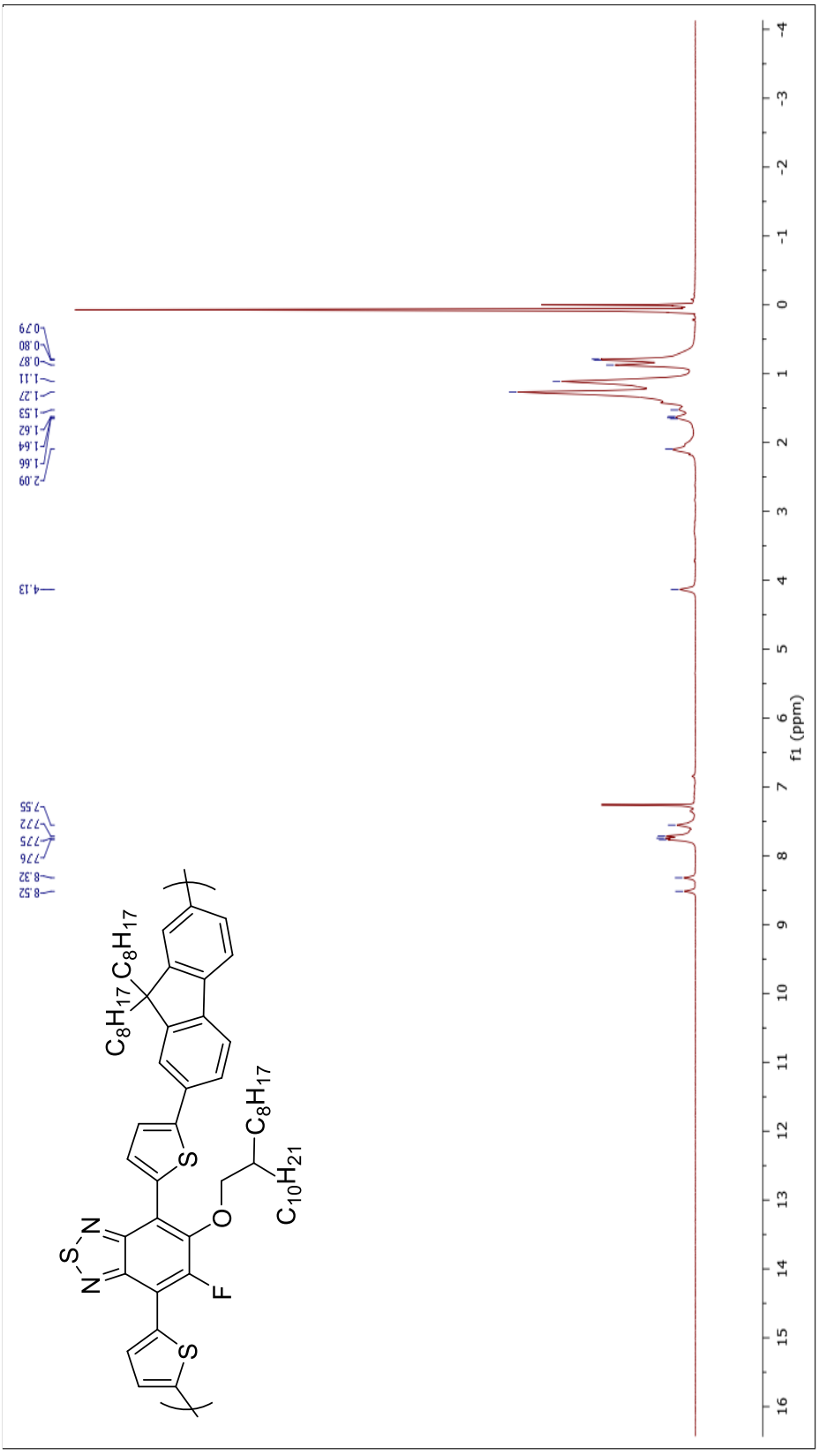

Figure A.37: ^{1}H NMR spectrum of P4.

APPENDIX B

HRMS SPECTRA

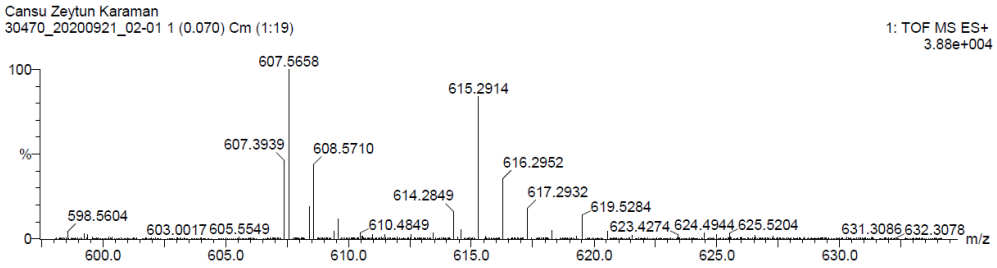

Figure B.1: HRMS spectrum of 5-fluoro-6-((2-octyldodecyl)oxy)-4,7-di(thiophen-2-yl)benzo[c][1,2,5]thiadiazole.

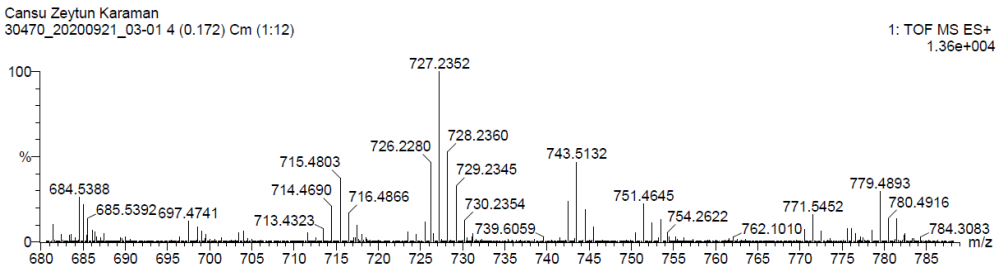

Figure B.2: HRMS spectrum of 5-fluoro-6-((2-octyldodecyl)oxy)-4,7-bis(thieno[3,2-b]thiophen-2-yl)benzo[c][1,2,5]thiadiazole.

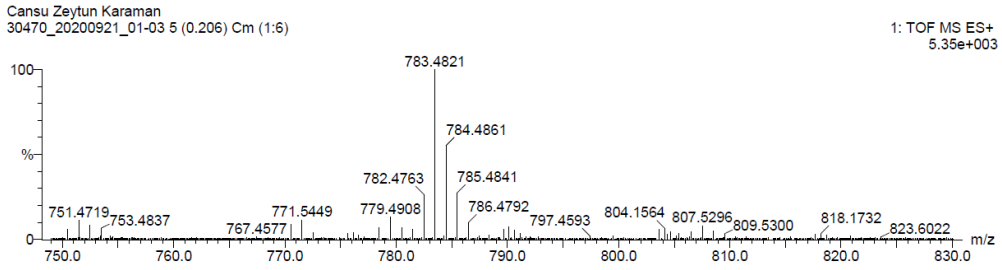

Figure B.3: HRMS spectrum of 5-fluoro-6-((2-octyldodecyl)oxy)-4,7-bis(4-hexylthiophen-2-yl) benzo[c][1,2,5]thiadiazole.

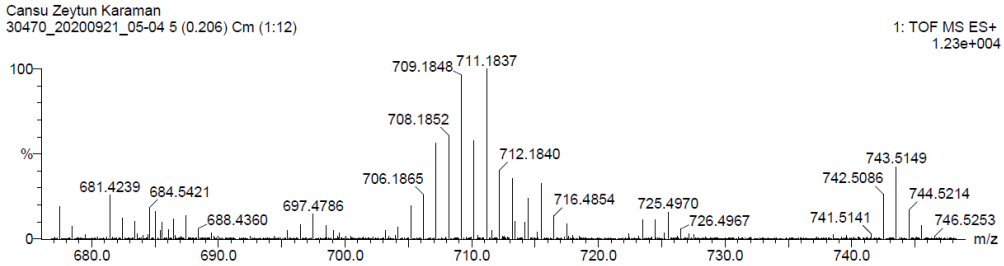

Figure B.4: HRMS spectrum of 5-fluoro-6-((2-octyldodecyl)oxy)-4,7-di(selenophen-2-yl)benzo[c][1,2,5]thiadiazole.

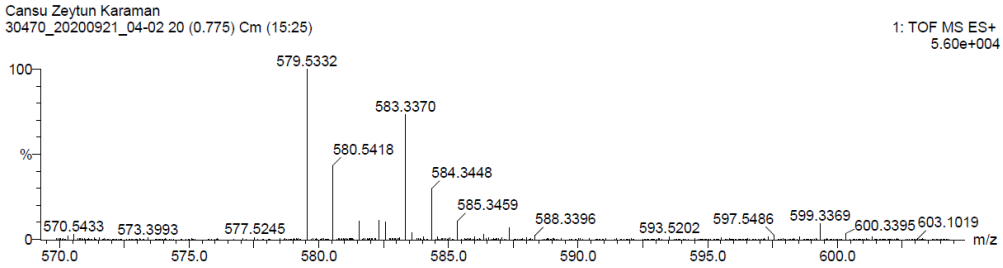

Figure B.5: HRMS spectrum of 5-fluoro-6-((2- octyldodecyl)oxy)-4,7-di(furan-2-yl)benzo[c][1,2,5]thiadiazole.

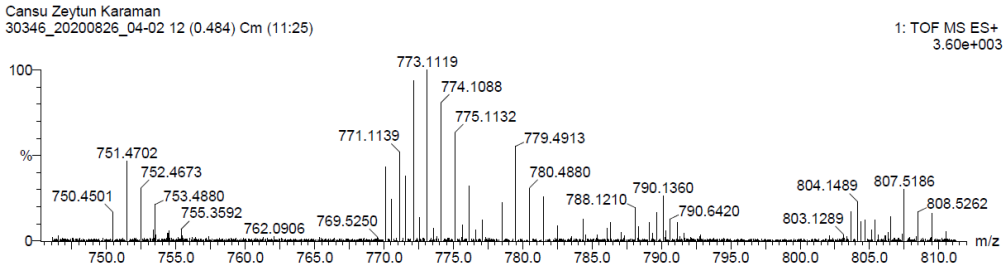

Figure B.6: HRMS spectrum of 4,7-bis(5-bromothiophen-2-yl)-5-fluoro-6-((2-octyldodecyl)oxy)benzo[c][1,2,5]thiadiazole.

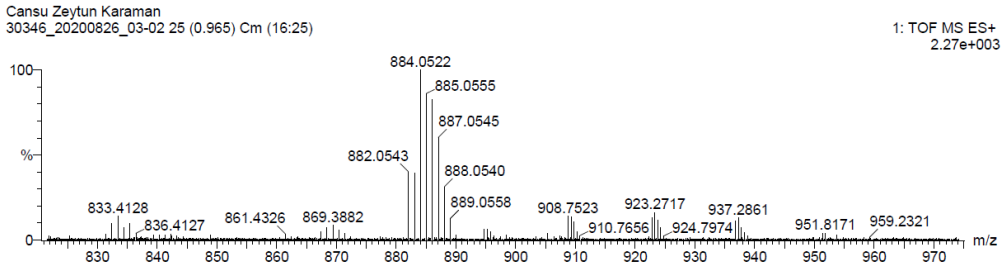

Figure B.7: HRMS spectrum of 4,7-bis(5-bromothieno[3,2-b]thiophen-2-yl)-5-fluoro-6-((2-octyldodecyl)oxy)benzo[c][1,2,5]thiadiazole.

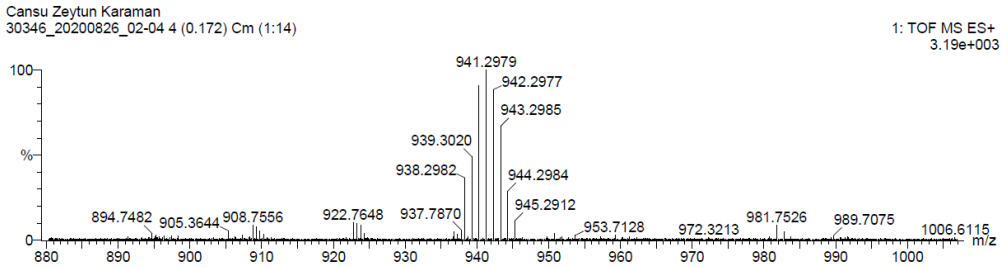

Figure B.8: HRMS spectrum of 4,7-bis(5-bromo-4-hexylthiophen-2-yl)-5-fluoro-6-((2-octyldodecyl)oxy)benzo[c][1,2,5]thiadiazole.

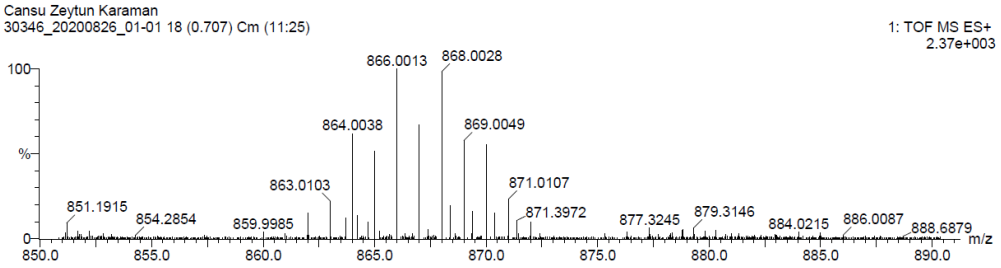

Figure B.9: HRMS spectrum of 4,7-bis(5-bromoselenophen-2-yl)-5-fluoro-6-((2-octyldodecyl)oxy)benzo[c][1,2,5]thiadiazole.

APPENDIX C

FTIR SPECTRA

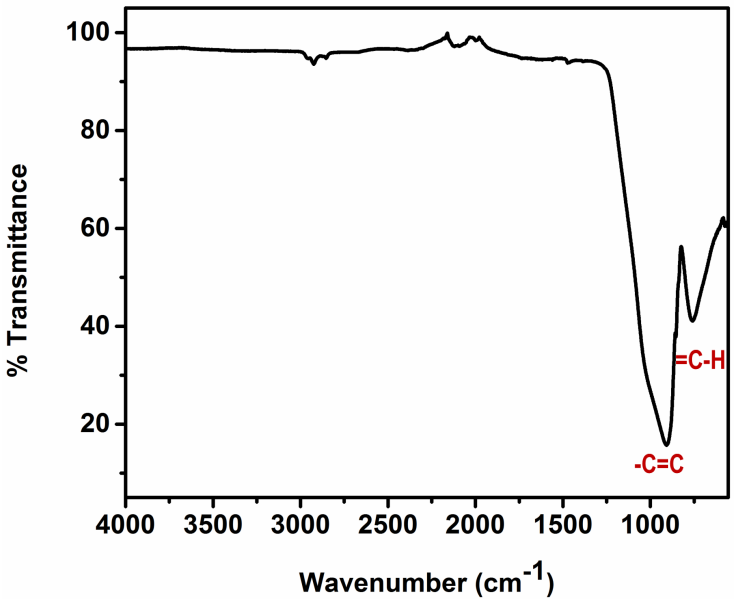

Figure C.1: FTIR spectrum of PTBTT.

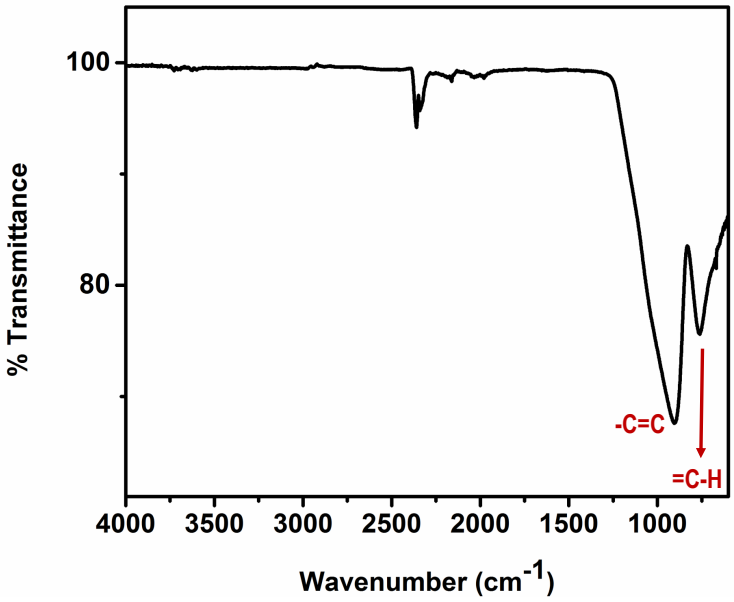

Figure C.2: FTIR spectrum of PHTBTHT.

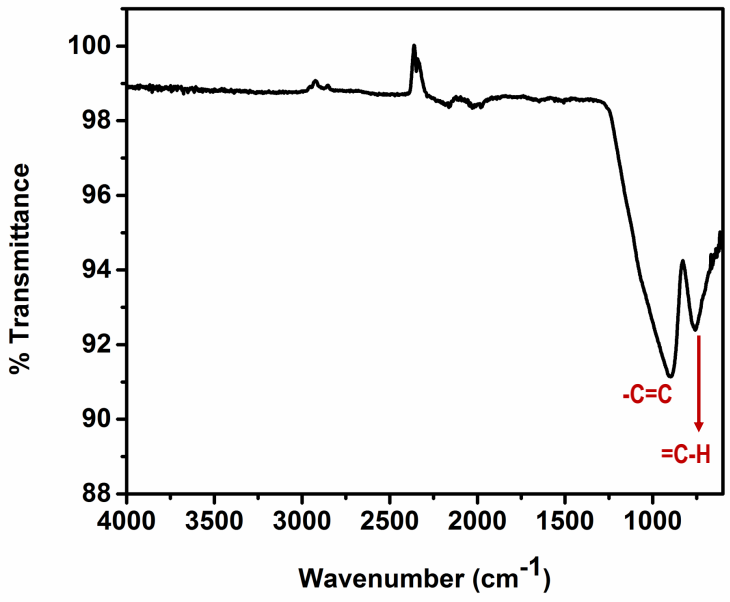

Figure C.3: FTIR spectrum of PFBTF.

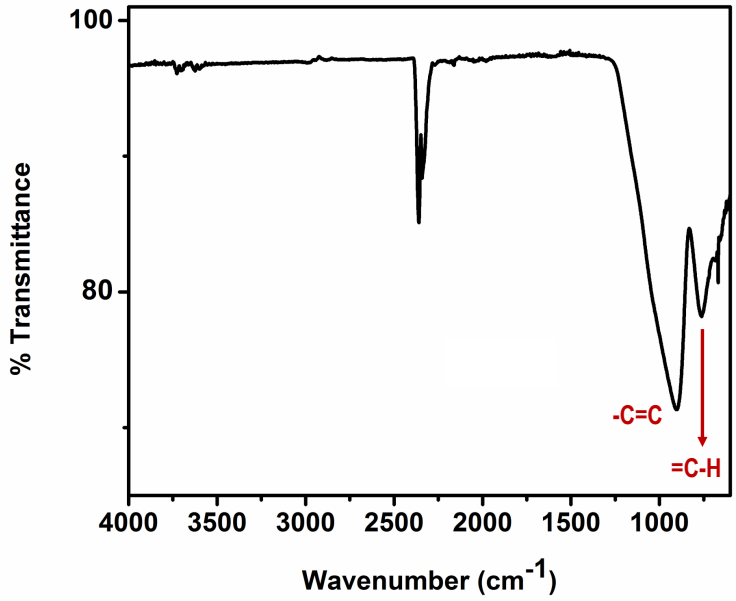

Figure C.4: FTIR spectrum of PTTBTTT.

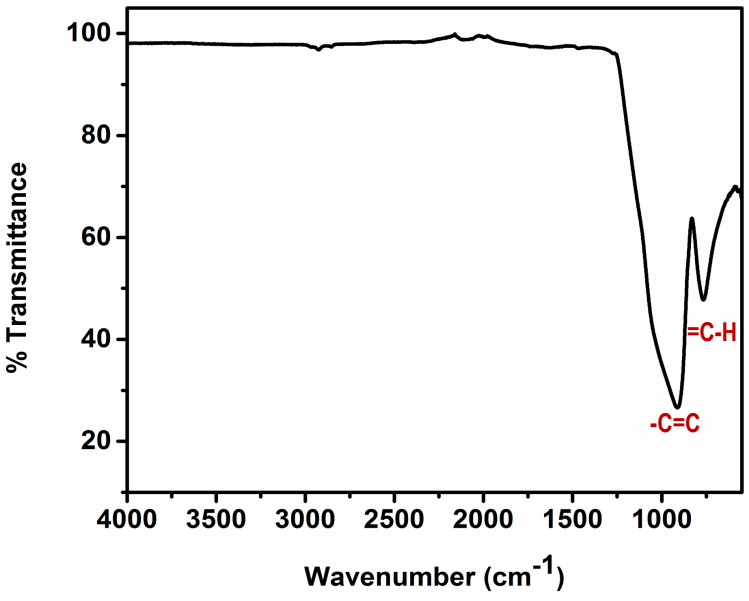

Figure C.5: FTIR spectrum of P1.

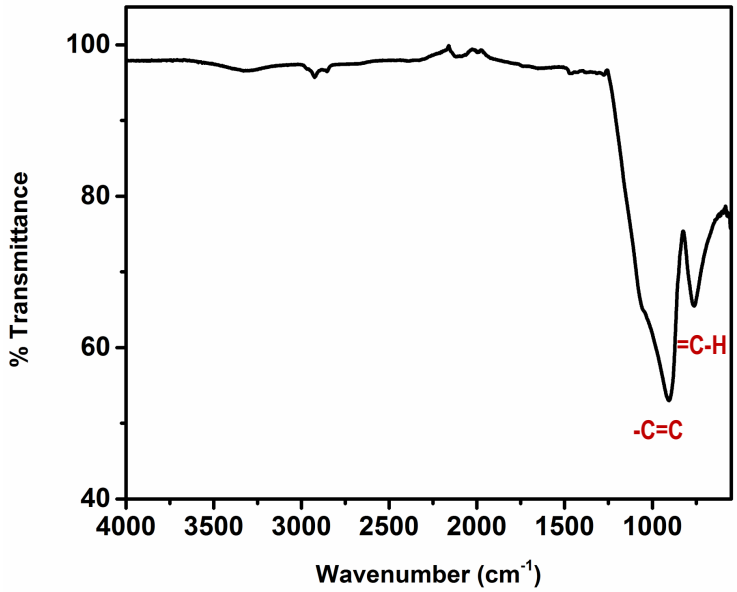

Figure C.6: FTIR spectrum of P2.

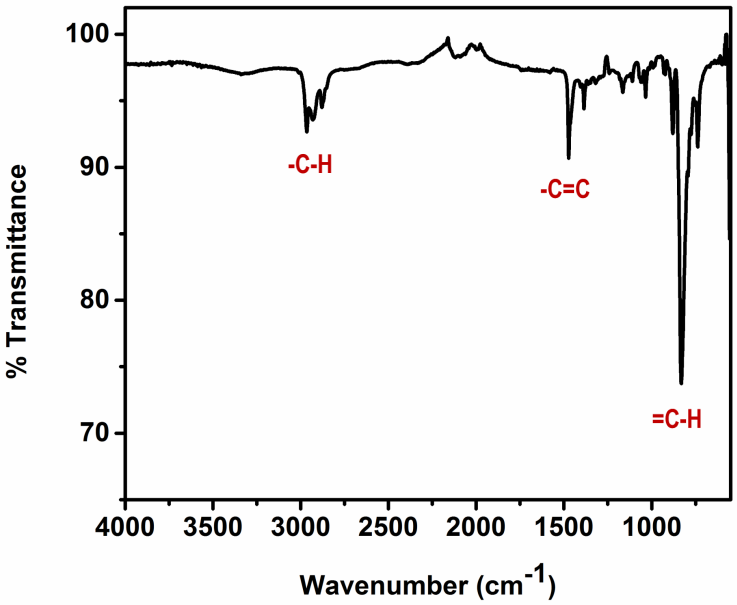

Figure C.7: FTIR spectrum of P3.

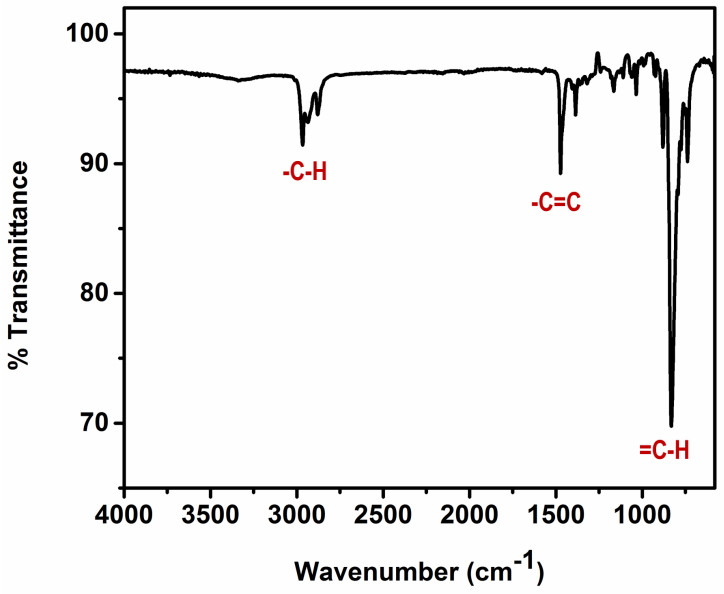

Figure C.8: FTIR spectrum of P4.